UNIVERSITÀ DEGLI STUDI DI TRIESTE

XXXVII CICLO DEL DOTTORATO DI RICERCA IN

SCIENZE DELLA RIPRODUZIONE E DELLO SVILUPPO

Development of polymeric nanoparticles for the delivery of nucleic acids in the treatment of B-cell malignancies

Targeted production of therapeutic antibodies by Burkitt lymphoma cells

Settore scientifico-disciplinare: MED/04

DOTTORANDA
MARIA CRISTINA GRIMALDI

COORDINATORE
PROF. PAOLO GASPARINI

SUPERVISORE DI TESI
PROF. PAOLO MACOR

CO-SUPERVISORE DI TESI
PROF. GABRIELE STOCCO

ANNO ACCADEMICO 2023/2024

UNIVERSITÀ DEGLI STUDI DI TRIESTE

XXXVII CICLO DEL DOTTORATO DI RICERCA IN
SCIENZE DELLA RIPRODUZIONE E DELLO SVILUPPO

Development of polymeric nanoparticles for the delivery of nucleic acids in the treatment of B-cell malignancies

Targeted production of therapeutic antibodies by Burkitt lymphoma cells

Settore scientifico-disciplinare: MED/04

DOTTORANDA
MARIA CRISTINA GRIMALDI Maria Cristina Grimaldi

COORDINATORE
PROF. PAOLO GASPARINI

SUPERVISORE DI TESI
PROF. PAOLO MACOR Paolo Macor

CO-SUPERVISORE DI TESI
PROF. GABRIELE STOCCO

ANNO ACCADEMICO 2023/2024

Table of contents

I. Riassunto

Le neoplasie delle cellule B rappresentano un gruppo eterogeneo di patologie comunemente trattate con chemioterapia e immunoterapia. Nonostante i progressi nella terapia, una percentuale significativa di pazienti sviluppa resistenza, non risponde adeguatamente o presenta effetti indesiderati. L'anticorpo antiCD20 Rituximab ha dimostrato di migliorare significativamente i tassi di sopravvivenza, ottenendo una remissione a lungo termine fino nel 95% dei pazienti. Poiché il CD20 non è espresso nelle cellule staminali, la rigenerazione delle cellule B rimane possibile dopo il trattamento. Tuttavia, l'azione del Rituximab sulle cellule B normali può portare alla loro deplezione, con conseguenti alterazioni delle loro funzioni canoniche. L'obiettivo di questo progetto di ricerca di dottorato è sviluppare un nuovo approccio terapeutico per le neoplasie pediatriche delle cellule B, in particolare il linfoma di Burkitt, attraverso la combinazione di nanovettori mirati, terapia genica e anticorpi terapeutici. Questa strategia mira a indurre la produzione di una proteina esogena, in particolare un anticorpo terapeutico antiCD20, all'interno del microambiente tumorale, minimizzando così gli effetti avversi tipicamente associati al trattamento convenzionale. Al fine di garantire un trasporto selettivo di acidi nucleici, abbiamo sviluppato nanoparticelle polimeriche biodegradabili in acido poli lattico-*co*-glicolico e alcol polivinilico, rivestite covalentemente con anticorpo ricombinante antiCD19 come meccanismo di targeting. Per valutare la funzionalità delle nanoparticelle, sono stati fatti caratterizzazione fisico-chimica, test di biocompatibilità e saggi di trasfezione per valutare il loro comportamento *in vitro* e *in vivo*. I risultati hanno dimostrato che le nanoparticelle incapsulano e rilasciano efficacemente il contenuto. Queste nanostrutture hanno mostrato un profilo di sicurezza favorevole, evidenziato dall'assenza di significativa citotossicità e attivazione della coagulazione, e solo una lieve attivazione del sistema del complemento, delle cellule endoteliali e dei leucociti. Il meccanismo di targeting antiCD19 ha migliorato la loro interazione con le cellule bersaglio, aumentando così la loro internalizzazione, la successiva espressione del DNA plasmidico esogeno e l'espressione proteica *in vitro*, e *in vivo* in un modello di linfoma umano in embrioni di zebrafish, dove non è stata osservata alcuna evidenza di tossicità. In un modello murino di linfoma di Burkitt, è stato osservato che le nanoparticelle raggiungono la massa tumorale e inducono una bassa produzione locale della proteina terapeutica antiCD20. Ciò ha comportato una modifica del microambiente tumorale, dovuta a una leggera attivazione del sistema del complemento e un lieve reclutamento di cellule del sistema immunitario, con effetti leggermente più pronunciati nei topi trattati con nanoparticelle mirate. I nostri risultati forniscono una motivazione per l'uso di nanoparticelle mirate come sistema di trasporto per il DNA esogeno per l'espressione locale di proteine terapeutiche e la modifica del microambiente tumorale, con la possibilità di immaginare queste nanostrutture come una nanopiattaforma in cui i singoli componenti (ad esempio, contenuto o meccanismo di targeting) possono essere sostituiti per raggiungere obiettivi disparati.

II. Abstract

B-cell malignancies represent a heterogeneous group of disorders commonly treated with chemotherapy and immunotherapy. Despite advancements in therapy, a significant proportion of patients either develop resistance, exhibit inadequate responses, or experience off-target effects. The antiCD20 antibody Rituximab has been shown to significantly improve survival rates, achieving long-term remission in up to 95% of patients. Since CD20 is not expressed in stem cells, B-cell regeneration remains possible following treatment. However, the action of Rituximab on normal B cells can lead to their depletion, resulting in alterations to their canonical functions.

The objective of this PhD research project is to develop a novel therapeutic approach for pediatric B-cell malignancies, particularly Burkitt lymphoma, through the combination of targeted nanocarriers, gene therapy, and therapeutic antibodies. This strategy aims to induce the production of an exogenous protein, specifically an antiCD20 therapeutic antibody, within the tumor microenvironment, thereby minimizing the adverse effects typically associated with conventional treatment. In order to ensure a selective delivery of nucleic acids, we developed biodegradable polymeric nanoparticles in poly(lactic-*co*-glycolic acid) and poly(vinyl alcohol) covalently coated with an antiCD19 recombinant antibody as a targeting mechanism. To assess the functionality of nanoparticles, physicochemical characterization, biocompatibility tests, and transfection assays were employed to assess their behavior *in vitro* and *in vivo*. The results demonstrated that nanoparticles effectively encapsulate and release the payload. These nanostructures exhibited a favorable safety profile, evidenced by the absence of significant cytotoxicity and coagulation activation and only slight activation of the complement system, endothelial cells, and leukocytes. The antiCD19 targeting mechanism enhanced their interaction with target cells, thereby improving their internalization and subsequent expression of exogenous plasmid DNA and protein expression *in vitro* and *in vivo*, in a human lymphoma model in zebrafish embryos, where no evidence of toxicity was observed. In a mouse model of Burkitt lymphoma, nanoparticles were observed to reach tumor masses and induce a low local production of the antiCD20 therapeutic protein. This resulted in a slight modification of the tumor microenvironment due to the activation of the complement system and slight recruitment of immune system cells, with barely pronounced effects observed in mice treated with targeted nanoparticles. Our findings provide a rationale for the use of targeted nanoparticles as an exogenous DNA delivery system for the local expression of therapeutic proteins and the alteration of the tumor microenvironment, with the possibility of envisioning these nanostructures as a nanoplatform in which individual components (e.g., payload or targeting mechanism) can be replaced to achieve disparate objectives.

III. List of figures

IV. List of abbreviations

AAV	Adeno-associated virus
ADC	Antibody-drug conjugates
ADCC	Antibody-dependent cellular cytotoxicity
Ag	Silver
ALL	Acute lymphoblastic leukemia
AML	Acute myeloid leukemia
Au	Gold
BCR	B-cell receptor
BL	Burkitt lymphoma
BM	Bone marrow
BSA	Bovine serum albumin
CAR	Chimeric antigen receptor
CD	Cluster of differentiation
CDC	Complement-dependent cytotoxicity
CFD	Complement Fixation Diluent
CH50	Complement hemolytic activity 50%
CH	Constant domain of heavy chain
CHO	Chinese Hamster Ovarian
CL	Constant domain of light chain
CLL	Chronic lymphocytic leukemia
CRISPR	Clustered Regularly Interspaced Shorts Palindromic Repeats
Cryo-EM	Cryogenic Electron Microscopy
CTCF	Corrected total cell fluorescence
Cu	Copper
Cy5.5	Cyanine 5.5
DLBCL	Diffuse large B-cell lymphoma
DLS	Dynamic Light Scattering
DMSO	Dimethylsulfoxide
DWNTs	Double-walled nanotubes
EA	Sensitized mutton erythrocytes
EBV	Epstein-Barr virus
EE	Encapsulation efficiency
ELISA	Enzyme-linked immunosorbent assay

EMA	European Medicines Agency
EGFP	Enhanced Green Fluorescent Protein
EPR	Enhanced permeability and retention
Fab	Antigen-binding fragments
FBS	Fetal bovine serum
Fc	Fragment crystallizable
FDA	Food and Drug Administration
GBM	Glomerular basement membrane
HIV	Human immunodeficiency virus
HL	Hodgkin lymphoma
HLMVECs	Human lung microvascular endothelial cells
hpf	Hours post-fertilization
hpi	Hours post-injection
HSCs	Hematopoietic stem cells
ICAM-1	Intracellular Adhesion Molecule 1
Ig	Immunoglobulin
iPSCs	Induced pluripotent stem cells
ITAM	Immunoreceptor tyrosine-based activation motifs
IVIS	*In Vivo* Imaging Systems
LDH	Lactate dehydrogenase
MAC	Membrane attack complex
MFI	Mean Fluorescence Intensity
MM	Multiple myeloma
MPS	Mononuclear phagocyte system
MRI	Magnetic resonance imaging
mRNA	Messenger RNA
MTT	3-(4,5-dimethylthiazol-2-yl)-2,5-diphenyltetrazolium bromide
MWNTs	Multi-walled nanotubes
NAP-2	Neutrophil-activating peptide-2
NHL	Non-Hodgkin lymphoma
NHP	Normal human-citrate anticoagulated plasma
NHS	Normal human serum
NK	Natural killer
NP	Untargeted nanoparticles

NPs	Nanoparticles
NTA	Nanoparticle Tracking Analysis
OD	Optical density
PDI	Polydispersity index
pDNA	Plasmid DNA
PEG	Polyethylene glycol
PEI	Polyethyleneimine
PF-4	Platelet factor-4
PGA	Poly(glycolic acid)
PLA	Poly(lactic acid)
PLC	Poly(ε-caprolactone)
PLGA	Poly(lactide-*co*-glycolide)
PMMA	Poly(methyl methacrylate)
PMN	Polymorphonuclear
PNPP	p-Nitrophenyl phosphate
PTU	Phenylthiourea
PVA	Poly(vinyl alcohol)
qRT-PCR	Quantitative Real Time-PCR
RISC	RNA-induced silencing complex
RNAi	RNA interference
ROI	Region Of Interest
RPMI-1640	Roswell Park Memorial Institute-1640
scFv	Single chain-Fragment variable
SD	Standard deviation
SEM	Scanning Electron Microscopy
SEM	Standard error of the mean
siRNA	Small interfering RNA
SMA	Spinal Muscular Atrophy
SWNTs	Single-walled nanotubes
TAA	Tumor-associated antigen
TB	Trypan blue
TLR	Toll-like receptor
TME	Tumor microenvironment
TNF	Tumor necrosis factor

tNP	Targeted nanoparticles
VH	Variable domain of heavy chain
VL	Variable domain of light chain
VPF	Vascular permeability factor
WHO	World Health Organization

1. Introduction

Despite the considerable advances that have been made in scientific research, cancer remains a major public health challenge with a high mortality rate observed across the globe. As reported by the World Health Organization (WHO), in 2023 there were an estimated 20 million new cases and 9.7 million deaths, with the prospect of a significant increase in the coming years [1]. Although cancer is a continent-wide issue, nearly one-quarter of all global cancer cases occur in Europe, which constitutes only one-tenth of the world's population. Breast, colorectal, prostate, and lung cancers collectively account for approximately 50% of the total cancer burden in Europe. In 2020, these cancers were also the leading causes of cancer mortality in the European continent, with pancreatic cancer additionally ranking as the fourth leading cause of cancer-related deaths [2]. In the pediatric context, cancer represents the second leading cause of death among children and adolescents aged 1 to 19 years. Leukemia is the most prevalent form, accounting for 46% of cases, followed by brain and other nervous system tumors (30%), lymphomas (28%), carcinomas (9%), bone tumors (6%), and retinoblastoma (2%) with a distribution variable based on the age [3]. Although childhood cancer is less prevalent than adult cancer, its effect on families and the healthcare system should not be underestimated. Despite extensive research, the primary causes of onset remain uncertain. The underlying causes of childhood cancer can be attributed to a combination of genetic and environmental risk factors, as well as inherent factors such as low birth weight, advanced parental age, and congenital anomalies [4]. In recent years, considerable advancement has been made in the management of childhood cancers, with overall cure rates reaching 90% in numerous high-income countries. In contrast, the range of cure rates observed in lower-middle-income countries is between 5% and 60%. These data highlight a significant disparity in the management of childhood cancers and subsequent survival rates, which is largely attributable to economic factors [5]. It is imperative to examine these trends in order to implement and develop preventive strategies [4, 6]. Nevertheless, the prevention of malignancies in children and adults is not a universally attainable goal. The most effective strategy for reducing the burden of cancer and improving outcomes is to prioritize prompt and accurate diagnosis, followed by effective, evidence-based therapy and tailored supportive care [7].

1.1. Hematological malignancies

Hematological malignancies, commonly referred to as blood cancers, are clinical conditions that originate from blood-forming and lymphoid tissues. They represent the fifth most frequently diagnosed cancer worldwide [8]. Given that they can develop from different stages of development or cell types, these malignancies constitute a heterogeneous group of pathologies. Depending on the specific point at which normal hematopoietic function is altered, they can be classified as either lymphoid or myeloid tumors. These are further classified into subtypes, which include leukemia, multiple myeloma (MM), non-Hodgkin lymphoma (NHL), and Hodgkin lymphoma (HL) [9]. Hematological malignancies are typically distinguished from other solid tumors largely by the presence of symptoms associated with bone marrow (BM) failure or suppression. The hematopoietic system is typically designed to continuously regenerate, ensuring the homeostatic replacement of blood cells and the ability to rapidly increase output to compensate for acute blood loss, particularly in cases of physical trauma, infection, and metabolic or toxic stress. In such circumstances, the hematopoietic system transitions from its typical steady state, which is characterized by slow cell proliferation, to an activated state. Normally, new lymphocytes are produced only when necessary to replace old cells that have undergone apoptosis. However, in hematological malignancies, this system malfunctions, resulting in uncontrolled growth and reproduction at an abnormal rate due to the development of cancerous cells [10, 11].

1.1.1. Development and maturation of B cells

B cells, a subtype of lymphocytes commonly known as B lymphocytes, are central elements of humoral immunity within the adaptive immune system. They play a crucial role in protecting against a vast array of pathogens and participate in allergic reactions through the production of antibodies. The primary characteristic is the clonally variable repertoire of cell surface immunoglobulin (Ig) capable of recognizing specific antigenic epitopes. In humans, as in other mammals, B lymphocyte development is a multi-step hierarchical process, that takes 2-3 days to complete. It begins in the BM from hematopoietic stem cells (HSCs). This process encompasses subsequent development, whereby HSCs give rise to common lymphoid progenitors, which subsequently develop into pro-B cells, pre-B cells, immature B cells, and finally, mature B cells (Figure 1.1) [12, 13].

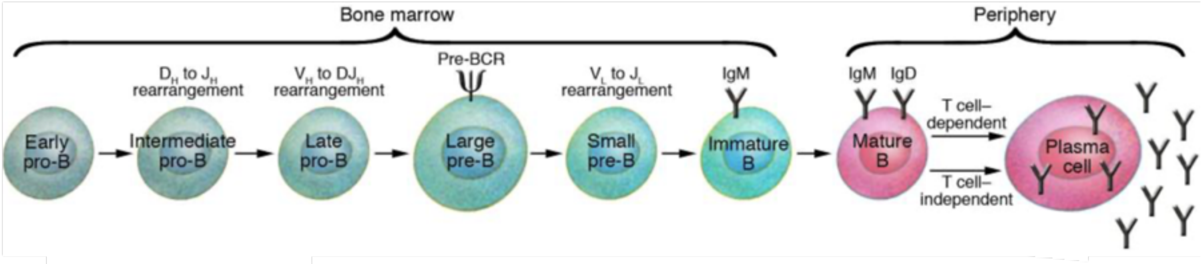

Figure 1.1. Simplified overview of B-cell development. Differentiation starts in the BM in an antigen-independent manner and is completed in the periphery in response to antigen interaction. In the BM, HSCs develop in lymphoid progenitors which give rise to pro-B cells. The rearrangement of the Ig H chain is initiated in pro-B cells and involves a series of sequential D_H to J_H and V_H to DJ_H rearrangements resulting in pre-B cells that express a pre-BCR. Upon completion of L chain rearrangement, immature B cells expressing an IgM migrate to the periphery where they can be activated by either T cell-independent or T-cell dependent antigen. This results in differentiation into plasma cells that secrete antibodies. Pillai, S., et al. 2005, modified.

Each of these stages is structured along sequential functional rearrangement processes of genes encoding variability (V), diversity (D), and joining (J) elements of the Ig heavy (H) and light (L) chain [14]. To gain a deeper comprehension of these mechanisms, it is essential to have a comprehensive understanding of the structure of Ig. In particular, each Ig molecule is composed of two H chains and two L chains which are connected by disulfide bonds. The L chain contains one variable domain (VL) and one constant domain (CL), while the H chain presents one variable domain (VH) and three or four constant domains (CH_1-CH_2-CH_3; CH_4 is exclusive to IgM and IgE). Two types of L chains, designed lambda (λ) and kappa (κ), are present in Ig. No functional differences have been identified between these two variants. In contrast, the H chain determines the class and, consequently, the effector function of an Ig. There are five main H chain classes (μ, δ, γ, α, and ε) which establish the functional activity and denote the corresponding class of Ig (IgM, IgD, IgG, IgA, and IgE respectively) [15, 16]. Consequently, throughout the entire maturation process, cells express a distinct conformation of the B-cell receptor (BCR) which is represented by either an IgM or an IgD in mature B cells. The structural organization of the BCR comprises two identical H and two identical L chains linked by a hinge, associated with an Igα/Igβ heterodimer which contains immunoreceptor tyrosine-based activation motifs (ITAM) as signaling motifs [17]. Upon recognition of an antigen by B cells, the BCR is activated, thereby initiating a signaling cascade that culminates in B-cell activation, proliferation, and further differentiation. Several distinct B-cell subsets have been defined, each of which plays a role in both adaptive and innate humoral responses [18]. It is noteworthy that this process has also been observed in jawed vertebrates, indicating that certain features have been preserved throughout evolution [19]. Analyzing the aforementioned process in detail, during the initial stage, pro-B cells undergo rearrangement of the D and J genes of the µH chain. This is followed by a second rearrangement which joins an upstream V region to the rearranged DJ segment. This marks the transition into the pre-B cell stage and the expression of the pre-BCR, constituted by µH chain assembled with surrogate L chains. Pre-B cells undergo 1 or 2 cell divisions to rearrange the gene encoding the κ and λ chains of the L chain. The combination of these latter chains with the previous µH chain generates an IgM expressed on the cell surface of immature B cells. The VDJ recombination process, which underlies these processes, is a stochastic event that occasionally fails. Consequently, immature B cells that express a BCR capable of recognizing endogenous self-antigens may be generated. Therefore, at this stage, B cells undergo screening for self-reactivity to establish B-cell tolerance and prevent autoimmunity. Immature B cells that fail to express a functional BCR or bind self-antigens typically undergo apoptosis or receptor editing to express a BCR that does not recognize self-antigens, respectively. Functional immature B cells that successfully pass this screening process then exit the BM and migrate to peripheral compartments such as the spleen and lymph nodes, where they complete their early development by differentiating into either naïve B cells, marginal zone B cells, or follicular cells. The activation of naïve B cells by either T cell-independent or T cell-dependent antigens results in their differentiation into antibody-secreting cells known as plasma cells [14, 20, 21]. Marginal zone B cells are so named due to their localization in the marginal zone of the spleen, where they serve as an interface between the immune and circulatory systems. These cells express a polyreactive BCR and produce low-affinity antibodies capable of reacting with and clearing pathogens and cellular debris. They constitute the initial line of defense, exhibiting heightened sensitivity to stimulation through Toll-like receptors (TLRs), thereby facilitating rapid antibody responses, particularly against blood-borne pathogens and T-independent antigens [22]. Upon activation, follicular B cells undergo a shift in expression, producing mono-reactive antibodies with high affinity following interaction with antigen-presenting T lymphocytes. This process encompasses both proliferation and differentiation, which are facilitated by somatic hypermutation of antibody genes that induce class switching (from IgM to IgG, IgA, or IgE) and enhance antibody affinity. These processes occur within germinal centers, which are anatomically divided into dark and light zones. The dark zone, situated in close proximity to T-cell areas, serves as a niche for proliferating B cells undergoing isotype switching and accumulating mutations in their immunoglobulin variable region genes, with the objective of enhancing BCR affinity and specificity. Subsequently, the cells undergo selective expansion, whereas those with impaired antigen-binding capacity undergo apoptosis. Cells then migrate to the light zone, where they undergo further selection by T lymphocytes [23].

Notably, all stages of development are phenotypically characterized by the expression of several B-lineage restricted surface antigens known as clusters of differentiation (CD) (such as CD10, CD19, CD20, CD21, and CD38). These antigens play a pivotal role, particularly in defining the stage of development of B-cell malignancies [12].

From a broader perspective, the maturation process is regulated by a complex network of cytokines and transcription factors that exert both positive and negative control over gene expression [24]. This makes B cells particularly susceptible to malignant transformation, notably through molecular alterations such as double-stranded DNA breaks, chromosomal translocations, inappropriate gene expression, and mutations occurring during antibody diversification processes [18, 25]. The clinical identification of distinct subtypes of B-cell malignancies, contingent on the stage of maturation and the specific cell type affected, allows for the monitoring of disease development and progression. This often involves the assessment of surface protein expression [12].

1.1.2. Classification of lymphoid malignancies

Since the 2000s, the proposed WHO classification has primarily stratified these neoplasms according to cell lineage, namely myeloid, B- and T-lymphoid, histiocytic neoplasms, and mast cell disorders. Each category is defined by a distinct set of neoplasms, characterized by a combination of morphological, immunophenotypic, genetic, and clinical features. Lymphoid blood cancers, which are summarized in Figure 1.2, are divided into leukemia and lymphoma. There are more than 80 recognized mature lymphoma subtypes, which are grouped into HLs, and NHLs based on their differing locations of appearance and advancement. The cells involved are the lymphocytes which are predominantly located in lymph nodes. This results in adverse effects on both the lymphatic and immune systems. NHLs represent a heterogeneous group of neoplasms, including B-cell, T-cell, or natural killer (NK) lymphomas. Approximately 85% of NHLs are B-cell lymphomas, which are further subdivided according to the histological features, appearance (e.g., follicular or diffuse), and growth and spread rate (e.g., indolent or aggressive) [26].

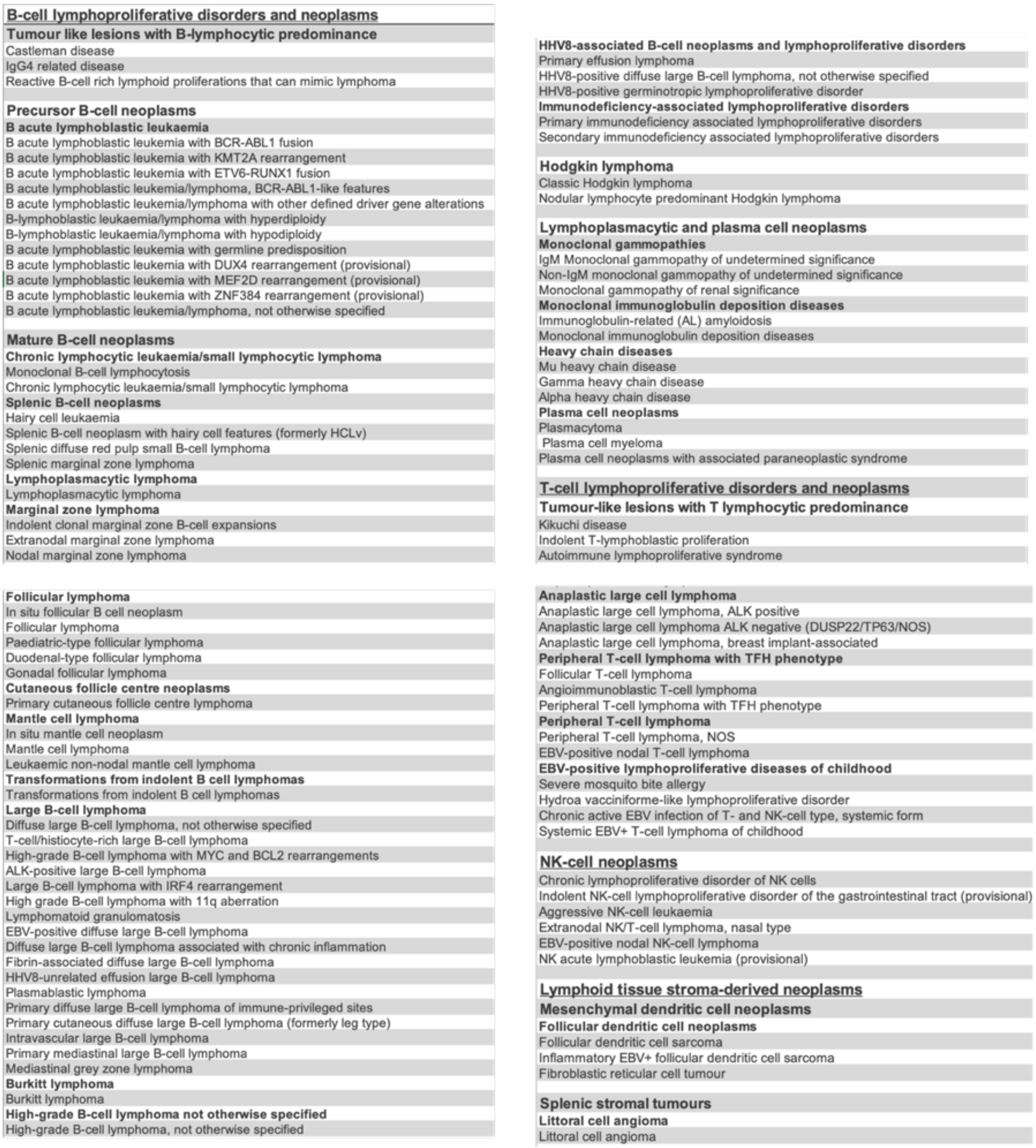

B-cell lymphoproliferative disorders and neoplasms
Tumour like lesions with B-lymphocytic predominance
Castleman disease
IgG4 related disease
Reactive B-cell rich lymphoid proliferations that can mimic lymphoma

Precursor B-cell neoplasms
B acute lymphoblastic leukaemia
B acute lymphoblastic leukemia with BCR-ABL1 fusion
B acute lymphoblastic leukemia with KMT2A rearrangement
B acute lymphoblastic leukemia with ETV6-RUNX1 fusion
B acute lymphoblastic leukemia/lymphoma, BCR-ABL1-like features
B acute lymphoblastic leukemia/lymphoma with other defined driver gene alterations
B-lymphoblastic leukaemia/lymphoma with hyperdiploidy
B-lymphoblastic leukaemia/lymphoma with hypodiploidy
B acute lymphoblastic leukemia with germline predisposition
B acute lymphoblastic leukemia with DUX4 rearrangement (provisional)
B acute lymphoblastic leukemia with MEF2D rearrangement (provisional)
B acute lymphoblastic leukemia with ZNF384 rearrangement (provisional)
B acute lymphoblastic leukemia/lymphoma, not otherwise specified

Mature B-cell neoplasms
Chronic lymphocytic leukaemia/small lymphocytic lymphoma
Monoclonal B-cell lymphocytosis
Chronic lymphocytic leukaemia/small lymphocytic lymphoma
Splenic B-cell neoplasms
Hairy cell leukaemia
Splenic B-cell neoplasm with hairy cell features (formerly HCLv)
Splenic diffuse red pulp small B-cell lymphoma
Splenic marginal zone lymphoma
Lymphoplasmacytic lymphoma
Lymphoplasmacytic lymphoma
Marginal zone lymphoma
Indolent clonal marginal zone B-cell expansions
Extranodal marginal zone lymphoma
Nodal marginal zone lymphoma

Follicular lymphoma
In situ follicular B cell neoplasm
Follicular lymphoma
Paediatric-type follicular lymphoma
Duodenal-type follicular lymphoma
Gonadal follicular lymphoma
Cutaneous follicle centre neoplasms
Primary cutaneous follicle centre lymphoma
Mantle cell lymphoma
In situ mantle cell neoplasm
Mantle cell lymphoma
Leukaemic non-nodal mantle cell lymphoma
Transformations from indolent B cell lymphomas
Transformations from indolent B cell lymphomas
Large B-cell lymphoma
Diffuse large B-cell lymphoma, not otherwise specified
T-cell/histiocyte-rich large B-cell lymphoma
High-grade B-cell lymphoma with MYC and BCL2 rearrangements
ALK-positive large B-cell lymphoma
Large B-cell lymphoma with IRF4 rearrangement
High grade B-cell lymphoma with 11q aberration
Lymphomatoid granulomatosis
EBV-positive diffuse large B-cell lymphoma
Diffuse large B-cell lymphoma associated with chronic inflammation
Fibrin-associated diffuse large B-cell lymphoma
HHV8-unrelated effusion large B-cell lymphoma
Plasmablastic lymphoma
Primary diffuse large B-cell lymphoma of immune-privileged sites
Primary cutaneous diffuse large B-cell lymphoma (formerly leg type)
Intravascular large B-cell lymphoma
Primary mediastinal large B-cell lymphoma
Mediastinal grey zone lymphoma
Burkitt lymphoma
Burkitt lymphoma
High-grade B-cell lymphoma not otherwise specified
High-grade B-cell lymphoma, not otherwise specified

HHV8-associated B-cell neoplasms and lymphoproliferative disorders
Primary effusion lymphoma
HHV8-positive diffuse large B-cell lymphoma, not otherwise specified
HHV8-positive germinotropic lymphoproliferative disorder
Immunodeficiency-associated lymphoproliferative disorders
Primary immunodeficiency associated lymphoproliferative disorders
Secondary immunodeficiency associated lymphoproliferative disorders

Hodgkin lymphoma
Classic Hodgkin lymphoma
Nodular lymphocyte predominant Hodgkin lymphoma

Lymphoplasmacytic and plasma cell neoplasms
Monoclonal gammopathies
IgM Monoclonal gammopathy of undetermined significance
Non-IgM monoclonal gammopathy of undetermined significance
Monoclonal gammopathy of renal significance
Monoclonal immunoglobulin deposition diseases
Immunoglobulin-related (AL) amyloidosis
Monoclonal immunoglobulin deposition diseases
Heavy chain diseases
Mu heavy chain disease
Gamma heavy chain disease
Alpha heavy chain disease
Plasma cell neoplasms
Plasmacytoma
Plasma cell myeloma
Plasma cell neoplasms with associated paraneoplastic syndrome

T-cell lymphoproliferative disorders and neoplasms
Tumour-like lesions with T lymphocytic predominance
Kikuchi disease
Indolent T-lymphoblastic proliferation
Autoimmune lymphoproliferative syndrome

Anaplastic large cell lymphoma
Anaplastic large cell lymphoma, ALK positive
Anaplastic large cell lymphoma ALK negative (DUSP22/TP63/NOS)
Anaplastic large cell lymphoma, breast implant-associated
Peripheral T-cell lymphoma with TFH phenotype
Follicular T-cell lymphoma
Angioimmunoblastic T-cell lymphoma
Peripheral T-cell lymphoma with TFH phenotype
Peripheral T-cell lymphoma
Peripheral T-cell lymphoma, NOS
EBV-positive nodal T-cell lymphoma
EBV-positive lymphoproliferative diseases of childhood
Severe mosquito bite allergy
Hydroa vacciniforme-like lymphoproliferative disorder
Chronic active EBV infection of T- and NK-cell type, systemic form
Systemic EBV+ T-cell lymphoma of childhood

NK-cell neoplasms
Chronic lymphoproliferative disorder of NK cells
Indolent NK-cell lymphoproliferative disorder of the gastrointestinal tract (provisional)
Aggressive NK-cell leukaemia
Extranodal NK/T-cell lymphoma, nasal type
EBV-positive nodal NK-cell lymphoma
NK acute lymphoblastic leukemia (provisional)

Lymphoid tissue stroma-derived neoplasms
Mesenchymal dendritic cell neoplasms
Follicular dendritic cell neoplasms
Follicular dendritic cell sarcoma
Inflammatory EBV+ follicular dendritic cell sarcoma
Fibroblastic reticular cell tumour

Splenic stromal tumours
Littoral cell angioma
Littoral cell angioma

Figure 1.2. Proposed WHO classification of lymphoid neoplasms. In accordance with the WHO classification system, neoplasms are classified as originating from cells of the lymphoid lineage at varying stages of maturation, including precursor and mature stages. Each subtype gives rise to a distinct disease entity, characterized by differences in morphology and clinical features. Adapted from https://whobluebooks.iarc.fr/structures/haematolymphoid/.

An example of indolent NHL, presenting a slow rate of growth, is follicular lymphoma which manifests at a slower rate of growth and is more prevalent in adults than in younger age groups, with a prevalence of 1-2%. In contrast, aggressive NHLs, including

Burkitt lymphoma and diffuse large B-cell lymphoma (DLBCL), exhibit rapid growth and account for approximately one-third of all NHLs globally [27-29]. As previously described, hematological malignancies represent the predominant form of cancer in the pediatric population. In high-income countries, there has been a notable increase in overall survival rates from 80% to 90% over recent decades. This improvement can be attributed to the use of intensive chemotherapy, steroid therapy, and radiotherapy, as well as the advent of novel treatment modalities, such as immunotherapy, which employs, for example, chimeric antigen receptor (CAR)-T cells, among other techniques. Notwithstanding these advances, challenges persist, including treatment-related mortality and relapse. The administration of elevated doses of conventional chemotherapy frequently proves ineffective in improving outcomes and may precipitate an increase in complications. Furthermore, long-term pediatric survivors often report a significantly higher prevalence of severe chronic disorders, with incidences up to three times higher than in the general population [30, 31].

1.1.2.1. Burkitt lymphoma

Burkitt lymphoma (BL) is a highly aggressive B-cell NHL and the most rapidly proliferating human cancer that accounts for 1-2% of all NHL cases in the general population. It is more prevalent in children and adolescents but accounts for a relatively low incidence rate in adults. BL was first reported by the Irish surgeon Denis P. Burkitt in 1958 when he described 38 Ugandan children with rapidly enlarging facial tumors that were uniformly fatal. He postulated that these tumors were round-cell sarcomas and observed a distinctive combination of jaw and orbital involvement, as well as a proclivity for extranodal dissemination to the adrenal glands, kidneys, liver, thyroid, pancreas, stomach, and ovaries. The histologic appearance was subsequently observed to be identical to that of lymphomas characterized by abdominal masses, and a lymphoid origin was confirmed [32]. BL is derived from germinal center B cells and is classified into three main clinical types: endemic, sporadic, and immunodeficiency-associated. A defining feature of BL is the inappropriately high level of c-myc transcription factor which normally regulates cell proliferation, differentiation, and apoptosis. This alteration derives from several different mechanisms, most commonly by translocation of the long arm of chromosome 8 (containing the *MYC* gene) and the Ig H chain gene on chromosome 14, resulting in a perpetuated proliferation state of B cells. This accounts for the rapid doubling time of

BL tumors [25, 33]. However, *MYC* translocation is also common in DLBCL and other high B-cell lymphomas, which presents a challenge for accurate diagnosis. Consequently, biopsy specimens may display monomorphic, medium-sized B cells with round nuclei and a cytoplasm that is deeply basophilic and often contains lipid vacuoles. Additionally, specimens may exhibit a "starry sky" pattern resulting from the presence of benign macrophages that have ingested apoptotic debris (Figure 1.3) [32].

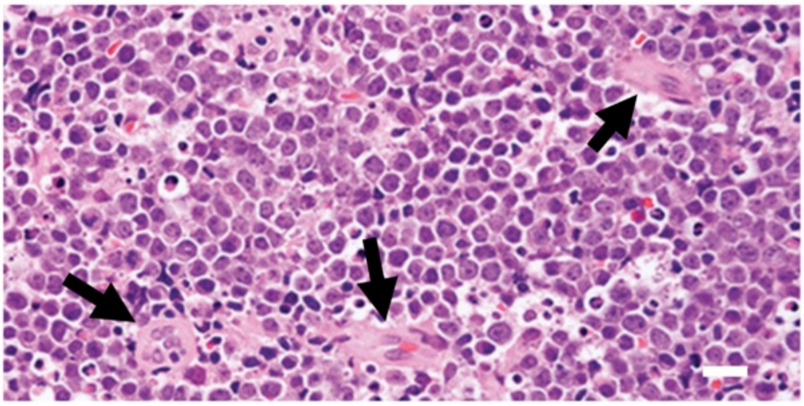

Figure 1.3. Morphologic features of Burkitt lymphoma. Hematoxylin and eosin staining method reveals the typical morphologic features of an involved lymph node from a patient with BL. These features include uniform sheets of medium-size cells with numerous mitotic figures and macrophages containing nuclear debris (black arrows) giving the classic “starry sky” appearance. Scale bar 20 µm. Roschewski, M., et al. 2022, modified.

In particular, sporadic BL is more prevalent in the pediatric population, accounting for approximately 30% of pediatric lymphomas. It typically manifests at around 10 years of age and is often associated with Epstein-Barr virus (EBV). It has a global distribution and encompasses forms that are not geographically restricted. The endemic form is primarily observed in children between the ages of four and seven in equatorial Africa and New Guinea, accounting for up to 50% of childhood cancers in these regions. It is also associated with EBV. Finally, immunodeficiency-associated BL is most frequently observed in patients infected with the human immunodeficiency virus (HIV) and in individuals with congenital immunodeficiency [34, 35]. In BL, malignant B cells express B-cell markers such as CD19, CD20, CD79a, and the germinal center marker CD10. Consequently, immunohistochemistry and cytogenetics play a pivotal role in the diagnosis of the disease. Some of the clinical manifestations include a rapidly growing mass, elevated lactate dehydrogenase (LDH), and increased uric acid. Additionally, there are instances where jaw lesions or BM involvement occur, though these occurrences are rare [36]. The standard first-line therapeutic approach is a high-dose chemotherapy regimen that includes cyclophosphamide, doxorubicin, vincristine, and prednisone. This approach often yields unsatisfactory results in patients who have become refractory to treatment and is associated with a range of adverse effects. Moreover, many clinical trials have demonstrated the efficacy of CAR-T cells in the treatment of B-cell lymphoma [37, 38].

The exploitation of the phenotypic features of B cells and their surface antigens, such as CD, represents an interesting therapeutic approach that sets the basis for most target therapy.

1.1.3. Tumoral B-cell markers and immunotherapy

As described in paragraph 1.1.1., each B-cell malignancy is associated with a distinct developmental stage and surface antigen expression profile. These latter, have a significant role in the identification of the degree of maturation, which is of particular importance for diagnosis, prognosis, and therapeutic approaches, especially those that are targeted and personalized [39, 40]. For clinical application, an ideal surface antigen should be abundant, accessible, and expressed homogeneously, consistently, and exclusively on the surface of target cells. These are fundamental features in the context of therapy, particularly in the field of immunotherapy [41]. It is well established that the immune system is capable of identifying and eliminating tumor cells through the exploitation of surveillance mechanisms, whereby tumor-associated antigens (TAAs) are recognized. Nevertheless, tumor cells can circumvent immune detection through a variety of mechanisms, including reduced surface expression, enhanced T-cell suppression, recruitment of immunosuppressive or regulatory immune cells, and the inhibition of immune cell activity due to the release of acidic and toxic metabolites within the tumor microenvironment. Consequently, the objective of cancer immunotherapy is to reactivate normal immune functions by employing immunomodulators, monoclonal antibodies, or the patient's immune cells [42]. Since the 1890s, immunotherapy has transformed cancer treatment. This is evidenced by the work of Dr. William Coley, a surgeon who injected live bacteria into patients with inoperable malignant tumors, observing a complete regression in most patients. This event led to his being dubbed the "Father of cancer immunotherapy" and established the foundation for the development of alternative treatments [43].

In the context of B cells, there are examples of specific markers (e.g., CD19, CD20, CD22, CD30, or CD52) that are overexpressed in cancerous conditions. As a result, these markers can be subjects in targeted immunotherapy. For example, strategies targeting CD22, a surface antigen predominantly expressed on B lymphoid cells, involve monoclonal antibodies such as Epratuzumab, which, despite efficacy, is associated with notable toxicity [44]. In contrast, CD52 serves as the target for Alemtuzumab, a depleting antibody approved in 2014 for multiple sclerosis, with broad expression on cells of the hematopoietic lineage. Due to its depletion effects on T and B cells, Alemtuzumab carries safety risks, including heightened susceptibility to infections and adverse autoimmune events [45]. Despite their use across different diseases, recent focus has centered on the historically promising antigens CD19 and CD20.

1.1.3.1. CD19

The human CD19 antigen is a transmembrane glycoprotein with a molecular weight of 95 kDa belonging to the Ig superfamily. It is constituted by a single transmembrane domain, a cytoplasmic C-terminus, and an extracellular N-terminus. CD19 is expressed in a specific and overexpressed manner in normal and neoplastic B cells, respectively. Its surface density is highly regulated throughout B-cell development, beginning with the pro-B cell stage and continuing until the loss of expression during terminal plasma cell differentiation. In addition to its expression in nearly all stages of B-cell development (except for the stem cells stage), it functions as a co-receptor in B-cell signaling. In particular, it exists in a complex with CD21 (also known as Complement Receptor 2) and CD81 (Figure 1.4). The first is involved in the binding of complement C3-derived fragments [46], while the second enables the assembly of the complex into membrane domains [47]. Subsequently, the complex facilitates the binding of the complement C3 cleavage product C3d, thereby enabling the interaction between CD19 and BCR. This provides a link between innate and adaptive immunity. This interaction results in a reduction in the number of antigen receptors required for cell activation, thereby lowering the threshold necessary for B-cell proliferation in response to a specific antigen [48, 49].

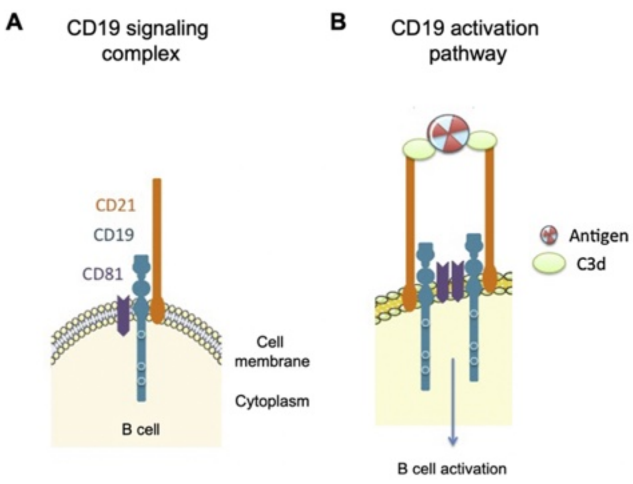

Figure 1.4. CD19 signaling complex and activation pathway. (A) Schematic representation of the CD19 signaling complex. The CD19 complex is constituted by CD21, CD81, and CD19 transmembrane proteins. CD19 contains an intracellular tail that is involved in signal transduction. (B) Pathway of CD19 activation: the CD19 complex is able to bind activated complement fragment C3d, thereby modulating BCR signaling. Jakobczyk, H., et al. 2017, modified.

In the context of therapeutic intervention, CD19 represents a more exploitable target in comparison to other commonly utilized targets (Figure 1.5). This is because it enables the targeting of early B-cell differentiation stages (e.g., acute lymphoblastic leukemia, ALL) which are not typically addressed by therapies that target the CD20 antigen, which is expressed at later stages. This approach has the potential to expand the number of patients who may derive benefit from treatment [50].

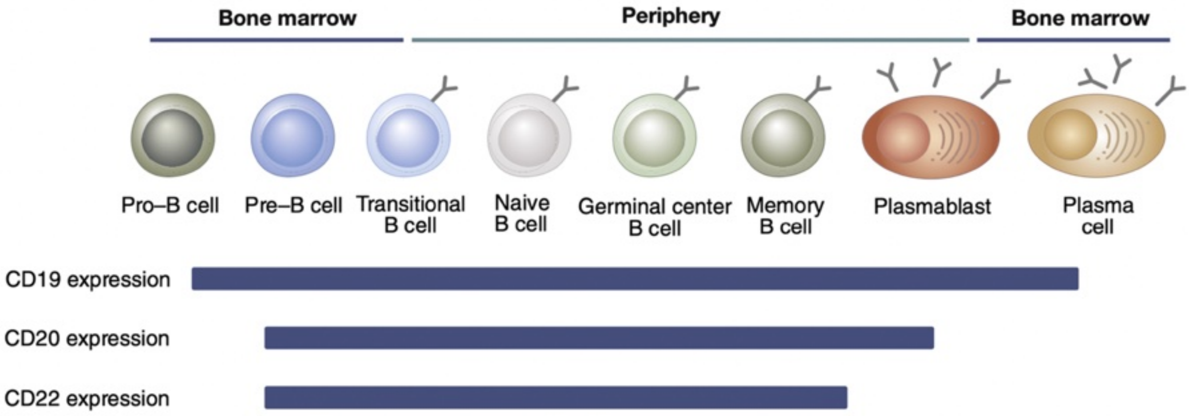

Figure 1.5. CD19 expression compared to other B-cell therapeutical targets. Illustrative representation of the expression of some B-cell antigens, used in therapy, throughout their developmental stages. Crickx, E., et al. 2020, modified.

For the past two decades, CD19 has been identified as a promising target for immunotherapy, particularly in those diseases that respond poorly to conventional chemotherapy. A variety of strategies, including antibody-drug conjugates (ADCs), fragment crystallizable (Fc)-engineered human CD19, bispecific antibodies, or CAR-T cells have been developed for the treatment of B-cell malignancies, with numerous approaches already approved by the Food and Drug Administration (FDA) or undergoing clinical trials. For example, Blinatumomab (BLINCYTO®, Amgen), a bispecific antibody construct approved for the treatment of Philadelphia chromosome-negative B-ALL both in adults and children, binds specifically to CD19 expressed on the surface of cells of B-lineage origin, and to CD3 expressed on the surface of T cells. This facilitates contact between these cells and enables activated T cells to eliminate B cells [49]. Moreover, Loncastuximab tesirine (ZYNLONTA™), an example of antiCD19 ADC, received its initial approval in 2021 for the treatment of adult patients with relapsed or refractory large B-cell lymphoma [51].

The key factor contributing to the efficacy of antiCD19 mediated approaches is the internalization of the CD19 antigen upon binding of antibodies or immunoconjugates, which is followed by uptake into lysosomes [49]. Time-lapse and co-localization studies have demonstrated that CD19 antigen internalization occurs within approximately 90 minutes after binding to a ligand. This is followed by the subsequent degradation of its components within the lysosomal compartment and the release of therapeutic metabolites [52-54].

1.1.3.2. CD20

Another crucial B-cell-associated antigen is CD20, which was the first target of monoclonal antibodies designed for therapeutic applications. CD20 is a tetraspanning membrane protein with a molecular weight of between 33 to 37 kDa. It is postulated to function as a subunit of a B-cell calcium ion channel. Furthermore, CD20 has been observed to localize in lipid rafts, which are involved in receptor-mediated signal transduction, and to directly interact with the BCR. As illustrated in Figure 1.5, CD20 is expressed on the surface of the majority of B cells, from late pre-B lymphocytes to differentiated plasmablasts. Thus, its absence on early stem cells or plasma cells allows for B-cell ablative therapy [55, 56]. CD20 has been an attractive target for several reasons, including its presence in over 95% of mature B-cell neoplasms and the fact that it is not actively internalized or shed from the cell surface under normal conditions, but is mostly shed upon antibody binding, making this an important consideration in the development of therapeutic strategies [57-59]. An increase in CD20 expression has been observed in patients with specific types of B-cell lymphoma and leukemia. The high levels of CD20 molecules present on the surface of B cells render it an attractive target for antibody-based therapy. Furthermore, these characteristics render it an effective effector agent in complement-dependent cytotoxicity (CDC) and antibody-dependent cellular cytotoxicity (ADCC) processes. Furthermore, the binding of antibodies to CD20 can result in the generation of signals that regulate cell growth and apoptosis in a range of cells, including tumor cells [60]. Over the years, several antiCD20 monoclonal antibodies have been approved for use, each of which binds to a different epitope of the CD20 protein and triggers a distinct effector function, including apoptosis, ADCC, and CDC. AntiCD20 antibodies are classified as Type I or Type II based on their mode of CD20 binding and the primary mechanism by which they kill cells. Specifically, B cells can be bound by twice as many Type I antibodies compared with Type II ones (in which only one antibody per CD20 is bound) most likely due to differences in binding geometries. As a result, Type I antibodies are capable of inducing the translocation of CD20 into lipid rafts upon binding. This clustering process enhances the recruitment and activation of the complement system, thereby enabling Type I antibodies to exert potent CDC. In contrast, Type II antibodies exhibit relatively lower activity in this regard because binding does not always promote the same degree of lipid raft redistribution [61, 62].

The first monoclonal antibody approved for the treatment of lymphoma, and that changed the management of NHL and chronic lymphocytic leukemia (CLL) was the widely recognized Rituximab (MabThera®; Rituxan). The mechanisms of action of this antibody will be described in detail in paragraph 1.1.3.2.1.

1.1.3.2.1. The advent of Rituximab

Rituximab is a chimeric IgG1 antiCD20 developed by Ronald Levy with the objective of targeting malignant B cells. In 1993, Rituximab was first employed in the treatment of lymphoma, resulting in a favorable response that led to its approval by the FDA in 1997. The binding of Rituximab to CD20 is responsible for the elimination of $CD20^+$ B cells primarily through CDC, and ADCC although antibody-dependent cellular phagocytosis or direct apoptosis play a role (Figure 1.6).

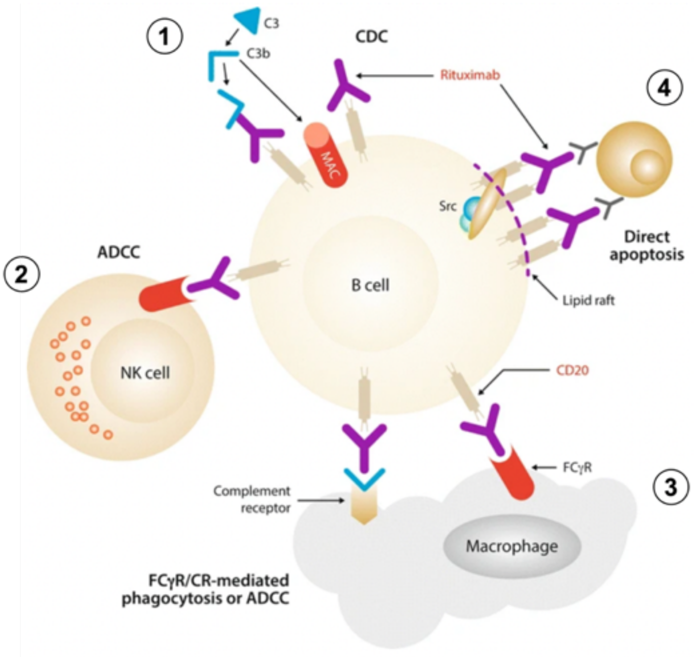

Figure 1.6. Mechanisms of Rituximab-mediated cell death. Rituximab-bound B cells are killed by at least four different mechanisms: (1) Binding of Rituximab to CD20 on the B-cell surface causes activation of the complement cascade, which generates the MAC, which can directly induce B-cell lysis by CDC. (2) Binding of Rituximab allows interaction with NK cells via Fcγ receptors, which leads to ADCC. (3) The Fc portion of Rituximab and the deposited complement fragments allow recognition by both Fc receptors and complement receptors on macrophages, which leads to phagocytosis and ADCC. (4) The crosslinking of several molecules of Rituximab and CD20 in the lipid raft determines the interaction of these complexes with elements of a signaling pathway (e.g., Src) that mediate direct apoptosis. Salles, G., et al. 2017, modified.

Specifically, the binding of Rituximab to tumor cells results in the reorganization of CD20 molecules into lipid rafts and subsequent activation of the classical pathway of the complement cascade which ultimately leads to cell lysis. In summary, upon binding to target cells, the Fc domain of the antibody recruits the complement component C1. The C1 complex, comprising of the antibody recognition protein C1q and the serine proteases C1r and C1s (C1r2s2), initiates a proteolytic cascade that culminates in the formation of the membrane attack complex (MAC) within the target cell membrane. This results in the creation of lytic pores and ultimately leads to cell death. In particular, surface-bound IgG molecules that organize into hexamers serve as a robust platform for C1q docking, effectively inducing complement activation. This highlights the significance of antibody clustering on the target surface, which enables efficient complement activation by facilitating avid C1q binding [63].

ADCC is a consequence of the interaction between the Fc region of Rituximab and antibody-coated tumor cells with membrane-bound Fcγ receptors on the surface of effector cells, including NK cells, granulocytes, and macrophages. This interaction leads to the activation of cellular immune responses, including the release of cytokines and mediators that target and destroy tumor cells. Furthermore, it is postulated that Rituximab binding to CD20 on B lymphocytes may induce cell death through a nonclassical apoptosis mechanism, involving the crosslinking of multiple CD20 molecules [64, 65].

Despite the incomplete understanding of the biological role of CD20, the introduction of Rituximab marked a transformative era of treatment for nearly B-cell NHL and for nearly 20 years Rituximab-based therapies have been the standard of care. Typically administered in conjunction with traditional chemotherapy or as monotherapy, Rituximab is also utilized as maintenance therapy. Particularly in pediatric BL, regimen-based therapy has significantly improved survival outcomes, achieving long-term complete remission in 95% of patients. However, despite the substantial contributions of Rituximab in extending life expectancy in the treated population, its high treatment costs remain a significant economic consideration [64, 66-68]. As previously stated, CD20 is not expressed on stem cells, which enables the regeneration of B cells following treatment with Rituximab. However, it is crucial to emphasize that Rituximab can also act on normal B cells, potentially leading to normal B-cell depletion [69] and subsequent effects on antibody production, cytokine networks, B-cell-mediated antigen presentation, and activation of T cells and macrophages [70].

For these reasons, research efforts over the years have focused on the identification of "next-generation" approaches, such as nanocarriers equipped with targeting mechanisms. The objective of these approaches is to guarantee therapeutic efficacy through the utilization of diverse types of therapeutic payloads, while simultaneously minimizing the incidence of adverse effects by selectively targeting neoplastic cells and preserving the viability of healthy cells.

1.2. Nanomedicine as an emerging approach for cancer treatment

The objective of targeted therapy to neoplastic areas without damaging normal tissues remains a challenging clinical goal in cancer treatment. Accordingly, the optimal pharmaceutical agent should be straightforward to administer, exhibit a high degree of specificity and affinity for its intended target, evade off-target effects, and remain in the body for a duration commensurate with the desired therapeutic outcome. This should result in a reduction of the adverse effects observed in healthy tissues. In light of these principles, nanomedicine has become an integral component of contemporary medical practice, addressing numerous limitations inherent to traditional approaches [71, 72]. This revolutionary field of research was first introduced by Richard Feynman in 1959. The term "nanosystems" is used to describe structures and materials with dimensions ranging from 1 nm to 1000 nm. The field has subsequently evolved into the contemporary concept of nanomedicine, which is employed for biomedical purposes such as diagnostics, prevention, and the treatment of diseases [73].

Nanoparticle design requires information on both materials and biological processes of interest, in addition to the structural and chemical properties, size, shape, and surface charge. This information renders them suitable for the treatment of several diseases [74]. Furthermore, in contrast to atoms and macroscopic materials, nanomaterials exhibit a high surface area-to-volume ratio and demonstrate tunable optical, electronic, magnetic, and biological properties. These features facilitate the development of personalized and safe pharmaceuticals. A significant challenge in cancer therapy is the poor water solubility and chemical stability of anticancer agents, which can severely affect drug uptake and bioavailability. The encapsulation of these compounds in hydrophilic carriers represents a technique that can be employed to overcome these issues. As nano-devices continue to evolve, the objective is to integrate the most efficacious dose of a pharmaceutical agent into a nano-system that can actively target specific sites and release its contents there, thereby enhancing overall efficacy. Concurrently, the selectivity for tumor cells minimizes interactions of nanoparticles with healthy tissues, thus reducing adverse effects. Moreover, these systems can safeguard against degradation *in vivo*, thereby prolonging their circulation time. It is therefore of paramount importance to select an appropriate nano-carrier [75].

The employment of diverse nanoparticle types to administer precise drug dosages to affected cells, such as tumor cells, without compromising the physiology of normal cells represents a pivotal area of research and development for decades to come. This is particularly true given the potential of nanomedicine and nano-drug delivery systems to revolutionize the way drugs are administered. Based on data from 2021, approximately 100 nanomedicines have been approved by the FDA for the treatment of various diseases (e.g., cancer, respiratory or ocular diseases, and prevention of SARS-CoV-2 infection) and recently, there has been a significant surge in the number of nanomedicine clinical trials [76].

1.2.1. Nanocarriers as a delivery platform: an overview in the hematological field

Several types of nanostructures are available and currently being explored for their potential use in clinical cancer therapy. These structures exhibit a range of characteristics, including shape, size, payload composition, and interactions with the surrounding biological environment. These characteristics collectively determine the attributes, benefits, and drawbacks of each nanocarrier, with applications in diverse clinical contexts. A comprehensive classification of the most commonly utilized nanostructures is presented in several reviews in the literature [77-79] with a particular focus on those employed in the treatment of hematological malignancies. In fact, a multitude of nanoparticle types, exhibiting diverse forms, dimensions, compositions, and functionalities, have been employed for the delivery of anticancer agents in the context of blood cancer therapy [80].

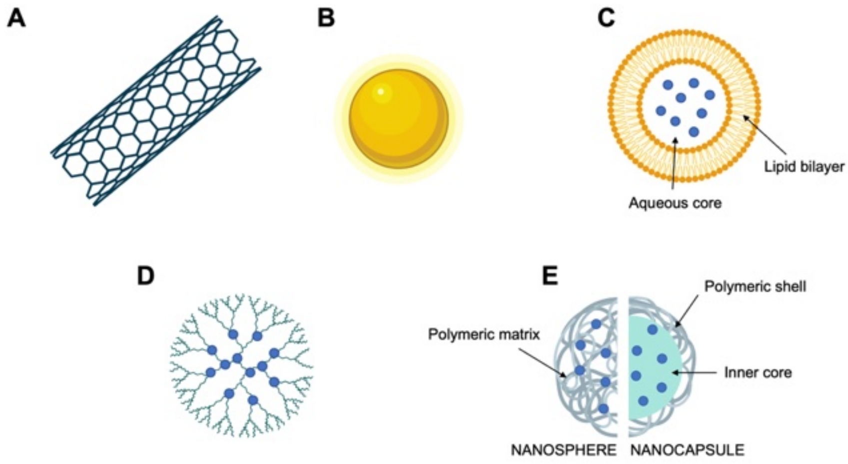

Figure 1.7. Schematic representation of some nanocarriers. (A) Carbon nanotube; (B) Gold nanoparticle; (C) Liposome; (D) Dendrimer; (E) Polymeric nanoparticle. Partially created with Biorender.com.

Nanoparticles are typically defined by the presence of one or more materials, which are organized in various ways to define multiple layers. The inner part is defined core and is often loaded with a therapeutic or imaging agent. The external layer, or shell, is formed by polymers, lipids, small molecules, or metal ions. Additionally, the surface of nanoparticles may be functionalized through the conjugation of targeting molecules, including peptides [81], antibody fragments [82], or full antibodies [83], to the external coat. These surface components exert significant influence on cellular uptake by modifying the surface chemistry, thereby promoting specific interactions and limiting non-specific ones [84]. Based on their composition, nanoparticles can be classified into several categories, with representative examples illustrated in Figure 1.7.

1.2.2. Carbon-based nanoparticles

This class of nanoparticles is composed exclusively of carbon atoms, arranged in either pentagonal or hexagonal units. Examples of such structures include carbon nanotubes (Figure 1.7A), which are elongated structures approximately 1-2 nm in diameter and are classified as single-walled (SWNTs), double-walled (DWNTs), or multi-walled (MWNTs). These nanotubes are distinguished by their adaptability, rendering them well-suited for drug delivery applications. In this regard, Mia et al. have demonstrated the potential of functionalized SWNTs for the eradication of leukemic B cells, offering a promising avenue for future leukemia therapy [85]. Furthermore, their electrical conductivity, high strength, and electron affinity render them an optimal vehicle for bioimaging (e.g., magnetic resonance imaging, MRI), energy storage, and environmental sensing to monitor or detect microbial pathogens [77, 78, 86].

1.2.3. Metal nanoparticles

Metal nanoparticles are composed exclusively of metal precursors, exhibiting monometallic, bimetallic, or polymetallic characteristics. They can be structured in diverse layers, including a core-shell configuration. The primary metals employed in their fabrication are copper (Cu), silver (Ag), and gold (Au) (Figure 1.7B), which exhibit a broad absorption band in the visible region. Due to their localized surface plasmon resonance characteristics and thermal properties, these nanoparticles possess unique optical and electrical properties, rendering them valuable in a multitude of scientific fields, including physical, chemical, biological, and pharmaceutical disciplines. Additionally, their synthesis can be controlled for specific facets, sizes, and shapes [77, 78]. Several studies investigating the potential of metal nanoparticles in the treatment of hematological malignancies, including MM and ALL, are currently underway. These studies have yielded promising results, demonstrating the ability of metal nanoparticles to inhibit the growth of tumor cells *in vitro*. However, the majority of these studies have focused on the theragnostic applications of metal nanoparticles, with further research needed to fully elucidate their therapeutic potential [80].

1.2.4. Liposome

The first class of nanocarriers approved by the FDA is represented by liposomes (Figure 1.7C). These synthetic spherical vesicles are structured with an aqueous core and unilamellar or multilamellar phospholipid layers. Due to their physicochemical properties, liposomes are employed in the fields of cosmetics and pharmaceuticals for the transport of small molecules and macromolecules. A noteworthy contemporary application of liposomes is in the field of vaccine design, where they serve as protective carriers for the delivery of genomic material or protein antigens. A notable example of this application is the use of liposomal technology by BioNTech/Pfizer and Moderna to develop nucleic acid-based vaccines for SARS-CoV-2. Specifically, a synthetic messenger RNA (mRNA) is encapsulated within a lipid formulation to protect it from nuclease degradation and to ensure adequate cellular internalization and protein expression. However, liposomes present certain challenges, including rapid clearance and relatively short circulating life. The lipid bilayer can be recognized by macrophages, which are phagocytic cells responsible for incorporating and eliminating microorganisms and foreign particles. These limitations can be surmounted through the functionalization and modification of the surface with natural or biocompatible polymers. Consequently, in 1995, the FDA approved Doxil®, the first PEGylated liposomal carrier loaded with doxorubicin for the treatment of several cancers, including MM. Doxil® is characterized by a polyethylene glycol (PEG) coating that protects the liposome from detection by phagocytic cells, allowing for prolonged circulation time. This formulation enhances the therapeutic profile of doxorubicin, which is typically associated with cardiotoxicity. In comparison to the free drug, the liposomal formulation has been demonstrated to reduce the likelihood of potential adverse effects [76, 87]. Over the years, different formulations have been approved for use in the treatment of ALL and acute myeloid leukemia (AML) respectively, including Marqibo® (vincristine-loaded liposomes) and Vyxeos® (cytarabine/daunorubicin-loaded liposomes) [80].

1.2.5. Dendrimers

Dendrimers (Figure 1.7D) are small synthetic macromolecules with a size range of 2 to 10 nm and a specific hyperbranched structure. These three-dimensional, globular structures are distinguished by their tree-like configuration and high branching points. The structure consists of a core, which can be a single atom or molecule, from which one or more branches emanate. The branches are formed from repeated units connected by branch junctions. The final structure is characterized by radial concentric layers, which are crucial for the properties of this nanocarrier. Dendrimers possess several key features that support their potential use as drug carriers. These include their ability to be taken up by cells with high efficiency, their high density of multiple functional groups (e.g., amines, hydroxyl groups, and carboxylic acids), their versatility, and their capacity to encapsulate or conjugate a high proportion of higher molecular weight drugs. Dendrimers are effective nanocarriers for nucleic acids because cationic dendrimers can form complexes with them. In the field of hematological malignancies, several studies are currently underway. For instance, Chittasupho C. et al [88] demonstrated that a dendrimer that specifically targeted CXCR4 (a chemokine receptor) by attaching a CXCR4 antagonist was effective against NALM-6, a leukemic precursor B-cell line. Despite the promising outcomes of the efficacy of dendrimer-based therapeutics, the efficiency of drug delivery remains a crucial limiting factor in the clinical translation of dendrimers. While the branched structure of dendrimers offers numerous potential drug-loading sites, the loading and release processes of drugs may be constrained, potentially impacting the efficiency of drug delivery [80, 89, 90].

1.2.6. Polymeric nanoparticles

Polymeric nanoparticles (Figure 1.7E) are colloidal systems composed of natural or synthetic polymers. These include both nanospheres, which are nanostructures characterized by a dense polymeric matrix containing the encapsulated agent, and nanocapsules, which are hollow structures with the payload contained within the polymeric matrix. The high encapsulation efficiency, biocompatibility, and efficient delivery of macromolecules are some of the main features that have led to the application and approval of these nanoparticles [91, 92].

The initial polymeric nanoparticles produced were based on poly(methyl methacrylate) (PMMA), polyacrylamide, polystyrene, and polyacrylates. These materials were not biodegradable, which resulted in several issues regarding disposal, degradation, and toxic accumulation in tissues. Therefore, imperative to facilitate the excretion of nanoparticles via carriers (e.g., feces, urine) or to physically remove them. Furthermore, the use of these polymers frequently resulted in chronic toxicity and inflammation. These shortcomings prompted a shift in focus toward biodegradable polymers. Biodegradable polymers are based on synthetic materials including poly(lactide) (PLA), poly(lactide-*co*-glycolide) copolymers, poly(ε-caprolactone) (PLC), and poly(amino acids), as well as natural materials including chitosan, alginate, and gelatin. The favorable biocompatibility and biodegradability are some of the features that have contributed to their success in drug delivery. The term "biocompatibility" is defined as “*the ability of a material to perform with an appropriate response in a specific* *application*". Therefore, it is essential to consider this property when designing and selecting nanoparticle materials. This suggests that, for a favorable outcome, after administration polymers should be disaggregated into biocompatible molecules disposable via metabolic pathways [93, 94].

1.2.6.1. Polylactide-*co*-glycolide and polyvinyl alcohol

Among the various biodegradable and biocompatible synthetic polymers, poly(lactide-*co*-glycolide) (PLGA) is a prominent and extensively researched material due to its comprehensive properties. PLGA has been approved by both the FDA and the European Medicines Agency (EMA) as a promising drug delivery system for a range of therapeutic agents, including chemotherapeutics, antibiotics, anti-inflammatory or antioxidant drugs, and proteins. PLGA is a copolymer comprising two distinct monomer units, poly(glycolic acid) (PGA) and PLA, linked via ester linkages, resulting in a linear, amorphous aliphatic polyester. Its success is notably attributed to its sustained drug-release capabilities, which differentiate it from conventional devices. *In vivo*, the polymer undergoes hydrolysis, yielding the original monomers (i.e., lactic acid and glycolic acid), which are endogenous and normally produced under physiological conditions (Figure 1.8). Consequently, these monomers are readily processed through metabolic pathways, such as the Krebs cycle, and excreted as carbon dioxide and water, thereby causing minimal systemic toxicity. The negative charge of PLGA is also of great importance in its function, as it significantly influences the interaction between nanoparticles and cells, reducing the number of unspecific interactions. In fact, cationic surfaces facilitate cellular binding and uptake due to the presence of negatively charged phospholipid groups, proteins, and glycans on the surface of cells. Additionally, these surfaces demonstrate rapid clearance and phagocytic uptake. In contrast, anionic nanoparticles, as well as those with a neutral surface, have been observed to exhibit a higher circulating half-life [95, 96]. Due to its low toxicity, biocompatibility, and controlled and sustained-release properties concerning tissue and cells, PLGA has been employed in clinical drug delivery systems. In the literature, several studies investigate the use of PLGA nanoparticles as a platform for the delivery of chemotherapeutic agents [97, 98] as well as several clinical trials are ongoing with targets on several diseases [99].

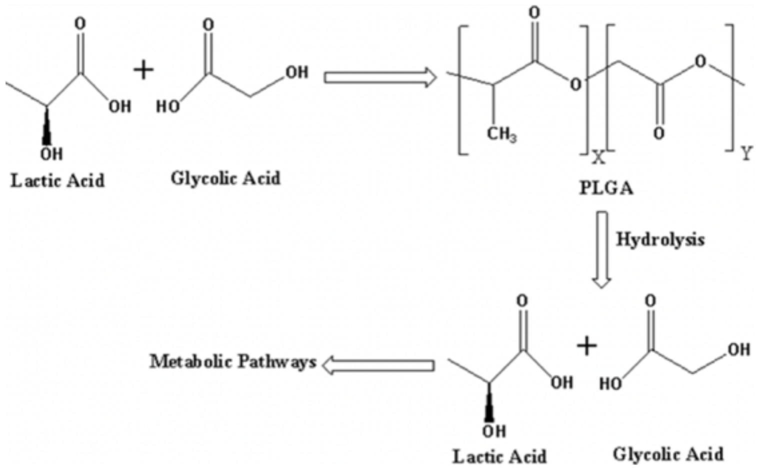

Figure 1.8. Representation of synthesis and metabolism of PLGA. PLGA is composed of monomers, lactic acid, and glycolic acid. The hydrolysis of PLGA results the formation of the endogenous monomers, lactic acid and glycolic acid, which can be processed via metabolic pathways, such as the Krebs cycle. X and Y represent the number of lactic acid and glycolic acid units, respectively. Alvi et al., 2022.

Another extensively studied synthetic and biocompatible polymer is poly(vinyl alcohol) (PVA). PVA is utilized in both clinical and non-clinical research, spanning the industrial and medical sectors. This versatility is attributed to the low toxicity of the polymer to human tissues and its advantageous physicochemical properties, including film-forming capability, emulsifying ability, flexibility, thermostability, and water solubility. In the field of nanomedicine, PVA is frequently employed as an emulsifier in the formulation of PLGA nanoparticles due to its ability to form an interconnected structure with PLGA, thereby facilitating the production of nanoparticles with relatively uniform small sizes [100].

Considering these factors, nanoparticles, including those based on PLGA-PVA, are regarded as promising tools in the field of nanomedicine due to their numerous potential applications. Nevertheless, when designing a drug carrier, it is crucial to recognize that the human body presents a multitude of obstacles that must be overcome. Accordingly, an understanding of the biodistribution of nanoparticles is of paramount importance.

1.3. Considerations of the biological limits in nanocarriers delivery

The principal objective of nanocarriers is to address the limitations associated with conventional drug formulations by enhancing the pharmacokinetic profile of drugs, thereby improving therapeutic performance and reducing adverse effects. To achieve this, it is essential to maintain optimal drug levels, preferably at the site of the disease. However, these platforms encounter considerable obstacles *in vivo*, including biological barriers, opsonization processes, and hepatic or renal clearance, which greatly influence their circulation time. Therefore, a comprehensive evaluation of these variables is essential for optimal nanoparticle characterization [101].

Upon intravenous administration, nanoparticles initially interact with the various components of the blood, including erythrocytes, platelets, white blood cells, complement system, and other serum proteins. This interaction has the potential to give rise to several pathophysiological processes, and thus, it is of great importance to be aware of it in order to evaluate the associated health risks. The contact between nanoparticles and erythrocytes should not cause hemolysis and then affect their function. Similarly, the adhesion of nanoparticles to the surface of platelets can result in the activation of a cascade of signals, leading to fibrin cross-linking and clot formation. This process may contribute to the development of stroke-related complications. Similarly, lymphocytes and monocytes, which constitute the host defense system, can release a variety of inflammatory mediators in response to their activation [102].

In addition to cellular components, biological barriers also play a significant role. The kidneys play a pivotal role in blood filtration and waste elimination, exerting a considerable influence on the transport and clearance of nanoparticles. The kidneys efficiently filter and rapidly remove nanoparticles from the body, reducing the potential toxicity of nonbiodegradable ones. The rate of renal clearance is dependent upon the dimensions and charge of both the nanoparticles and the glomerular basement membrane (GBM). The GBM, with pores measuring between 2 and 8 nm and a negative charge, facilitates the higher elimination of cationic nanoparticles with a diameter of 6-8 nm in comparison to anionic or neutral ones [103].

Furthermore, the foreign nature and surface properties of nanoparticles influence opsonization processes (Figure 1.9), thereby facilitating phagocytosis. In fact, nanoparticles in the bloodstream interact with plasma proteins resulting in the formation of a coating layer called protein corona, which will be discussed in greater detail in the next paragraph. In general, this coating renders nanoparticles more visible to phagocytic cells, which recognize these materials via ligand-receptor interactions, resulting in their rapid elimination. Some opsonins are proteins that are part of the complement system. Consequently, their involvement leads to complement system deposition and possible activation, resulting in the release of anaphylatoxins (e.g. C3a, C5a), C3b, and C5b-C9 lytic complex. This, in turn, causes inevitable local inflammation. The main actor involved in this recognition process is the mononuclear phagocyte system (MPS), comprising macrophages primarily located in the spleen, lymph nodes, and liver [79] [104, 105].

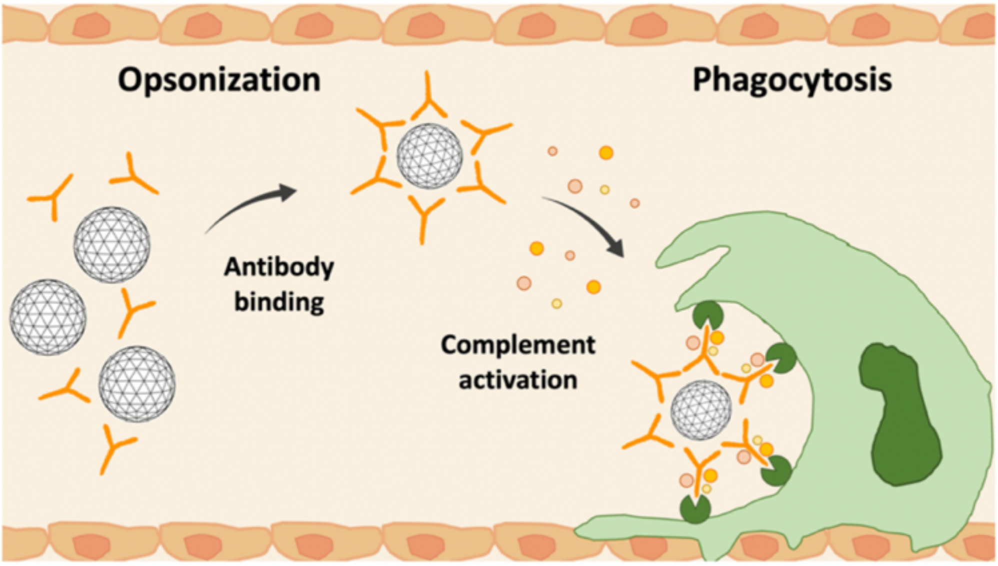

Figure 1.9. Opsonization process. The absorption of serum proteins on the surface of nanoparticles initiates the opsonization process. In the liver vessels (endothelial cells in orange), opsonized particles are subsequently recognized by receptors on phagocytic cells and then internalized. Bozzer et al., 2022.

In particular, the liver contains Kupffer cells, which are resident macrophages that manage hepatic phagocytic activity through highly differentiated surface receptors. Consequently, the hepatic clearance of nanoparticles affects both drug delivery and safety as a result of the increased risk of undesired liver accumulation and toxicity. The rate of liver uptake is significantly influenced by the physicochemical properties of nanoparticles, including size, surface charge, and shape. For example, nanoparticles sized 400-600 nm or those that are positively charged are preferentially eliminated by Kupffer cells in comparison to neutral nanoparticles [106].

Successful strategies to reduce and avoid the engulfment of nanoparticles by the MPS have been developed. These include the surface functionalization of nanoparticles with sterically shielding and hydrophilic polymers, such as PEG. This strategy serves to prevent, minimize, or modify protein absorption, thereby reducing vulnerability and prolonging the circulation half-life. In addition to PEG, alternative surface modification approaches are being explored, including those involving endogenous components such as proteins and lipids [102, 107].

1.3.1. Protein corona formation

The protein corona is a dynamic, multilayered structure that forms as a result of the spontaneous interaction of nanoparticles with highly concentrated proteins in biological fluids, particularly blood. This process is time-dependent, resulting in alterations to the identity, size, and surface charge of nanoparticles. These changes significantly impact the interactions of nanoparticles with cell membranes, internalization pathways, cytotoxicity, targeting ability, and *in vivo* clearance. The nature of this process allows for the distinction between a hard and a soft protein corona. The hard protein corona is constituted by high-affinity proteins that rapidly and directly adsorb onto the surface of nanoparticles, remaining stable over time. In contrast, the soft protein corona is composed of proteins that exhibit a weak interaction with the pre-bound hard corona. The primary distinction between hard and soft coronas is the native conformation of the adsorbed proteins. Proteins in the soft corona maintain their native conformation, whereas those in the hard corona undergo structural changes. The assessment is further complicated by the continuous binding and exchanging that are the fundamental processes underlying this phenomenon. These processes can be described by the Vroman effect (Figure 1.10) which posits that proteins with a higher or lower concentration and smaller size (e.g., albumin) interact first with nanoparticles, forming the soft corona. As they possess a low affinity, the exchange rates are relatively short, contributing to a reversible bond. This process facilitates the replacement of less abundant proteins with those that exhibit a higher affinity, thereby leading to the formation of the hard corona [108-110].

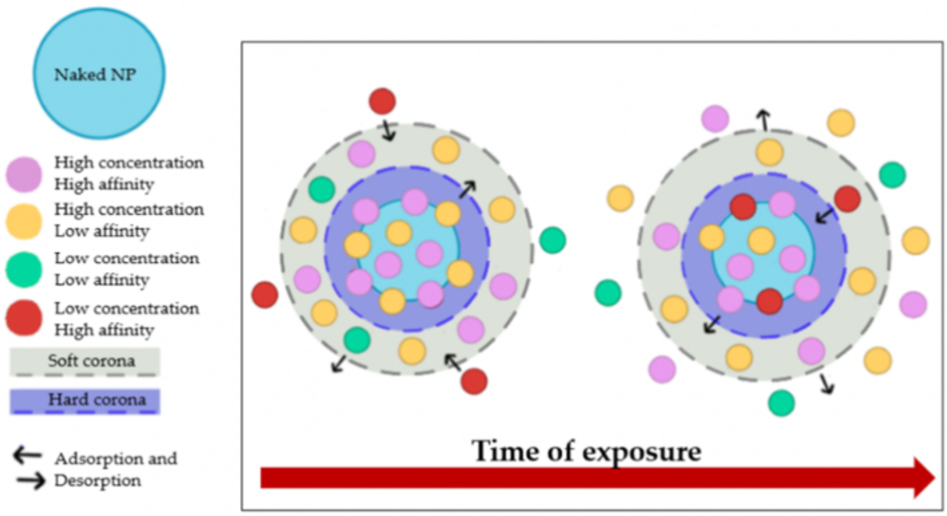

Figure 1.10. Overview of the Vroman effect. Over time, proteins with a higher affinity displace proteins with a lower affinity. Panico et al., 2022, modified.

Among the proteins involved, two distinct categories can be identified: opsonins and dysopsonins. Specifically, opsonins (e.g., complement system, IgG, IgA, and IgM) are proteins that reduce the half-life of nanoparticles and accelerate their degradation *in vivo* by activating the immune system. In contrast, the term dysopsonins (e.g., histidine-rich glycoprotein, apolipoprotein, albumin, and surfactant proteins A and D) refers to any substance capable of inhibiting immune system activation and phagocytosis through a phenomenon known as "stealth". This interaction is unavoidable, yet there is a mounting interest in developing strategies to disguise various types of nanoparticles. Potential approaches include coating with dysopsonins [111], polymers (e.g., PEG [112]), or biomimetic coatings (e.g., erythrocytes [113], and cancer membranes [114]). These methods aim to reduce serum protein absorption and enhance the *in vivo* therapeutic efficacy of nanoparticles in diverse contexts [106, 108].

It is therefore evident that, in addition to enhancing the half-life of nanoparticles, it is of paramount importance to address the issue of the unintended accumulation of nanoparticles in the body. To overcome this obstacle and guarantee the targeted delivery of nanocarriers to the intended site, research has been concentrated on developing targeting mechanisms.

1.3.2. The impact of targeting

The ability of nanocarriers to target specific cells is a crucial aspect of drug delivery, as it allows for the enhancement of therapeutic efficacy while minimizing the risk of cytotoxicity to normal cells. Numerous studies have explored the targeting design of nanoparticle-based drugs. It is evident that in order to effectively address the challenges of tumor targeting and nanocarrier system design, it is of the utmost importance to first gain a comprehensive understanding of tumor biology and the interaction between nanocarriers and tumor cells [115]. Targeting mechanisms can be broadly classified into two categories: passive targeting and active targeting which is also associated with stimuli-sensitive mechanisms. In fact, drug release can be triggered by internal conditions (e.g., pathophysiological or pathochemical conditions) or external stimuli (e.g., temperature, light, ultrasound, and magnetic force). These approaches facilitate intracellular delivery and achieve suitable therapeutic outcomes by exploiting conditions present in neoplastic tissue, thereby minimizing systemic exposure and limiting potential harm [116].

1.3.2.1. Passive targeting

Passive targeting (Figure 1.11) relies on distinct tumor features and the surface properties of the nanocarrier, including size, shape, and charge. It entails the delivery of nanoparticles to the target area via mechanisms such as endocytosis, adsorption by diverse tissues and cells, capillary entrapment, or the exploitation of the elevated permeability of blood vessels in diseased tissues [117].

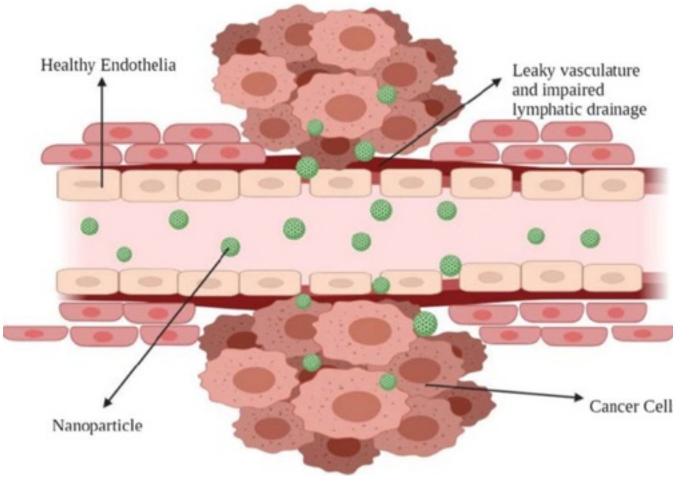

Figure 1.11. Representation of the passive targeting mechanism of nanoparticles in both a healthy blood vessel and a vessel adjacent to cancer cells. In healthy endothelium (left) nanoparticles remain in the bloodstream. In the presence of cancer cells (middle), the leaky vasculature and the impaired lymphatic drainage allows the passage of nanoparticles through the fenestrations, ultimately reaching cancer cells. Gavas et al., 2021.

The theoretical foundation for exploiting tumor passive targeting is the enhanced permeability and retention (EPR) effect, initially delineated by Maeda and colleagues [118]. In accordance with this phenomenon, the endothelial layer of blood vessels exhibits increased permeability under conditions such as hypoxia or inflammation. In hypoxic conditions, rapidly growing tumor cells induce the formation of new blood vessels or co-opt existing ones to meet their metabolic demands, a process known as neovascularization. The newly formed blood vessels are leaky and possess large pores, or fenestration, in the range from 200 to 2000 nm. This results in poor permeability selectivity compared to normal blood vessels. This provides minimal resistance to extravasation, allowing nanoparticles to diffuse from blood vessels to the tumor microenvironment (TME) and ultimately collect within cancer cells [118, 119].

Furthermore, in addition to the EPR effect, the TME plays a pivotal role in passive targeting. Rapidly proliferating tumor cells primarily rely on glycolysis for energy, which results in the generation of an acidic surrounding environment. The lowered pH of the TME can be exploited by utilizing pH-sensitive nanoparticles. These modifications to the TME play a significant role in the activity of stimuli-responsive nanoparticles. When these nanoparticles react to environmental factors such as temperature or enzymatic activity, it enhances the specificity of drug release, which has the potential to transform cancer therapy [120]. Despite the approval of formulations that exploit this process, passive targeting has encountered numerous challenges in clinical trials. It is evident that the EPR effect is a highly heterogeneous phenomenon, exhibiting considerable variability between different tumors and between individual patients. This variability can be attributed to various factors, including the degree or extent of angiogenesis and lymph angiogenesis, the extent or degree of perivascular tumor invasion, and intratumor pressure. Nevertheless, the EPR effect can be regulated, either mechanically or chemically, using nitric oxide, peroxy nitrate, bradykinin, vascular permeability factor (VPF), ultrasound, radiation, and hyperthermia, despite the existence of certain limitations and contraindications. Consequently, an intriguing alternative entails the examination of tumor-selective active targeting nanoformulations, which can optimize accumulation at the target sites [121, 122].

1.3.2.2. Active targeting

Active targeting systems (Figure 1.12) are designed to selectively deliver cargo to cancerous cells while sparing normal cells. The selectivity is contingent upon the molecular recognition of overexpressed receptors or antigens on cancerous cells, which is achieved through the use of targeting molecules on the surface of nanosystems. For the active targeting strategy to be effective, the specific antigen must be present and accessible on the targeted cells. Furthermore, the localization of the tumor antigen and its expression must remain consistent throughout the treatment period [119, 120, 123].

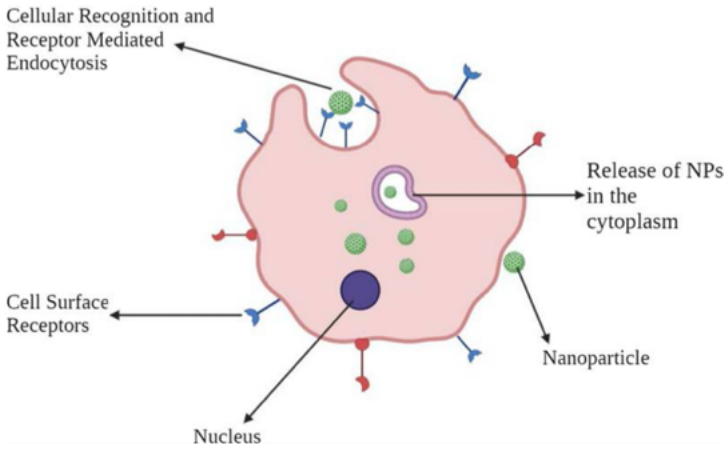

Figure 1.12. Representation of the active targeting system of nanoparticles. Nanoparticles with ligands on their surface interact with specific surface receptors (blue and red) expressed on cells, resulting in the internalization of the nanoparticles into the cytoplasm via endocytosis. Gavas et al., 2021.

In this context, nanoparticles, particularly polymeric nanoparticles, offer a high degree of versatility in terms of modification possibilities and can serve as functional platforms for the assembly of well-defined multifunctional structures. Minor variations in polymeric composition and ligand surface functionalization have been demonstrated to enhance the targeting ability of nanoparticles in biological systems. Specifically, active drug targeting employs a variety of affinity ligands to direct the binding of nanoparticles to numerous biological targets, primarily antigens overexpressed in tumor cells, the endothelial cells of tumor vasculature, or other diseased tissues within the tumor microenvironment [123-125].

The principal function of the targeting ligand is to facilitate the internalization of nanoparticles into target cells. Active targeting is expected to enhance the therapeutic efficacy in comparison to non-targeted nanoparticles due to an increase in internalization in target cells. While the biodistribution of nanoparticles is closely related to their colloidal properties, the targeting ligand is of paramount importance for enhancing cell recognition and uptake at target sites [124, 126]. A crucial aspect of nanocarrier design is the selection of an appropriate targeting ligand. A variety of targeting agents can facilitate the delivery of nanoparticles to specific tissues. These include proteins (e.g., antibodies [83] or their fragments), aptamers [127], and small molecules such as vitamins and peptides [82]. An illustration of these agents is provided in Figure 1.13.

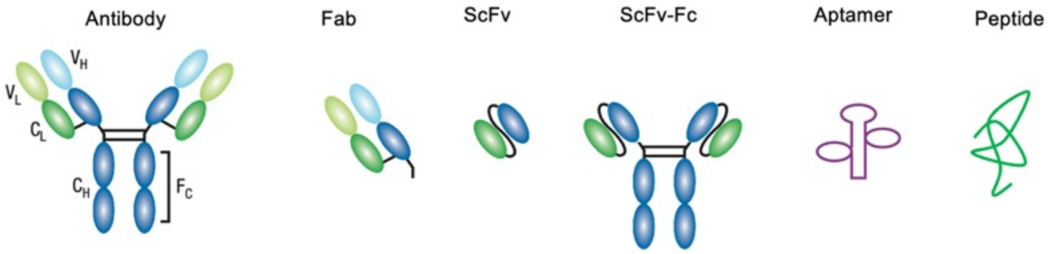

Figure 1.13. Examples of targeting agents. Starting from left are there is the structure of a full antibody which includes the VH, VL, CL and CH domains. Next, there are examples of antibody fragments such as Fab, scFv, and scFv-Fc. Finally, small targeting molecules, including aptamers and peptides, are show. Peer et al. 2007, modified.

Antibodies are the most commonly used targeting ligands due to their high degree of specificity and affinity, offering novel insights into disease treatment [117, 119]. Several studies have been conducted employing antibody-targeted nanoparticles for the treatment of various diseases [82, 128], including B-cell malignancies [83, 129, 130]. While these studies have yielded promising results *in vitro* and *in vivo*, it is essential to consider the potential limitations associated with their size and immunogenicity when contemplating their clinical application. These limitations restrict the number of antibodies that can be attached to the surface of nanoparticles and can increase the diameter of the nanoparticles themselves. However, advances in molecular technology have enabled the overcoming of these challenges through the engineering of antibodies, including single-chain Fragment variable (scFv), which can be covalently fused to an Fc thereby generating scFv-Fc, or antigen-binding fragments (Fab) [95].

While targeting is generally perceived as advantageous in preclinical studies, numerous complicating factors can constrain the success of targeted nanoparticle therapies. One significant challenge is poor tissue penetration. Additionally, issues such as heterogeneous antigen expression and the loss of cell surface antigen expression during disease progression further complicate targeted nanoparticle therapies. Another complicating factor is the formation of a protein corona on nanoparticles, which may impact the targeted delivery [131].

1.4. Gene therapy: the future of medicine?

The recent advancements in cell and gene therapies have enabled the treatment of a diverse array of conditions, ranging from congenital disorders to solid cancers. Since the first gene therapy procedure in 1990, considerable research has resulted in the approval of numerous gene therapy products in recent years, signifying the advent of a new era in this field. Gene therapy is defined as the treatment of disorders or diseases by transferring engineered genetic material into human cells using various strategies. To date, the expression of a specific gene or protein has been achieved through the introduction of plasmid DNA (pDNA) or mRNA into target cells. Conversely, the suppression of a particular gene has been accomplished through the use of small interfering RNA (siRNA) or RNA interference (RNAi) technology [132].

Gene therapy originated in 1989 when Dr. James A. Wyngaarden approved the first clinical protocol to insert an exogenous gene into the immune cells of a cancer patient as an immunotherapy approach for melanoma. Subsequently, gene therapy has become a prominent therapeutic approach, having been approved as an advanced therapy medicinal product for the treatment of distinct monogenetic diseases and B-cell malignancies. Notable examples include oligonucleotide-based therapies (Spinraza, for the treatment of Spinal Muscular Atrophy, SMA), cell therapies (Kymriah, and Yescarta, for the treatment of ALL and DLBCL respectively), and *in vivo* gene therapies (Luxturna and Zolgensma for the treatment of *retinitis pigmentosa* and SMA respectively) [133, 134].

Based on previous clinical trials and currently approved products, the field of gene therapy is advancing rapidly, with numerous new products expected to receive approval in the near future. As previously stated, gene therapies typically entail the transfer of genetic material into cells with the objective of reversing an abnormal condition or inducing a new trait. The specific approach employed depends on the underlying genetic issue. Potential strategies include addition, editing (repair), and deletion/knockout (inactivation) [135]. For instance, gene therapy can introduce a modified gene into cells to confer new characteristics, such as CAR structures in CAR-T cells [136], or suicide genes like Thymidine Kinase into cancer cells [137]. Furthermore, some gene therapies seek to elicit an immune response through the introduction of a specific antigen, a strategy that gained prominence with the advent of the SARS-CoV-2 vaccine [138]. Gene therapy can also be employed to repair or edit a mutation or defective genes by exploiting CRISPR technology or methods such as siRNA (antisense oligonucleotides). Although gene therapy is a treatment option for various genetic disorders, it is most used for cancer. In fact, from 2010 to 2020, the majority of clinical trials focused on cancer-related gene therapies and hematological cancers were particularly well-studied, largely due to the advent of CAR-T cells [139].

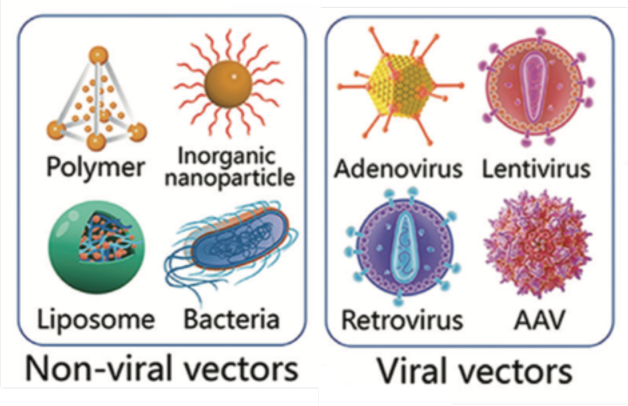

Figure 1.14. Overview of gene therapy strategies. Therapeutic nucleic acids are delivered directly to the patient’s target cells via viral or non-viral vectors. Yu et al., 2021, modified.

Gene delivery strategies can be broadly classified into two categories: viral vector-mediated and non-viral vector-mediated (Figure 1.14). This classification will be discussed in the following paragraphs.

1.4.1. Viral vector-mediated gene delivery

Gene therapies approved for clinical use predominantly employ viral delivery systems, including those derived from adeno-associated viruses (AAVs), retroviruses, lentiviruses, and adenoviruses, due to their high transfection efficacy. The selection of the vector is contingent upon the disease indication and the desired duration of gene expression. In the case of acute diseases such as infectious diseases and cancers, high-level transient expression from replication-deficient viral vectors can provide the necessary therapeutic efficacy. In contrast, chronic diseases often necessitate long-term expression, which can be achieved through the extrachromosomal presence or chromosomal integration of the viral vector or transgene to ensure sustained therapeutic activity. It is generally accepted that replication-deficient and non-integrating vector systems are only capable of providing long-term transgene expression in post-mitotic tissues [132, 140].

For instance, viral-based techniques have been employed for the production of CAR-T cells, specifically for the delivery of CAR genes into T cells through the use of retroviral or lentiviral vectors. Nevertheless, despite the advantages of viral vector-based gene delivery, the main drawbacks are their immunogenicity and cytotoxicity, which may result in inflammatory reactions. It is therefore imperative to guarantee the security of oncolytic and replication-proficient vectors. Furthermore, concerns have been raised regarding the safety of chromosomal integration, as random integration events into the host cell genome have been associated with severe adverse outcomes [141]. In addition, the inherent immunogenicity, and the presence of pre-existing host antibodies against viral components can diminish the efficacy and utility of viral vehicles in clinical settings. It is also noteworthy that the restricted capacity for DNA (less than 8 kb) and the inherent difficulties associated with manufacturing (complex, time-consuming, and expensive) impose further limitations on the use of viral-based vectors [142].

1.4.2. Non-viral vector-mediated gene delivery

If the viral vector-mediated approaches ensure greater efficiency but lack biocompatibility, conversely, the non-viral vector-mediated ones guarantee high biocompatibility but fail to achieve the efficacy of their viral counterparts [141]. Moreover, they have the advantages of low cost, simple preparation, facile mass production, safety, and the potential for delivering an unlimited length of exogenous genes. In addition, they are more readily stored and have longer shell lives due to their stability [132].

Non-viral approaches include physical methods (e.g., electroporation and magnetofection) which are primarily utilized, as well as chemical carriers which encompass lipid- and polymer-based vectors [141].

1.4.2.1. Lipid-based vectors

In recent times, lipid-based vectors have emerged as a prominent contender in the field of nucleic acid delivery systems, particularly in the context of SARS-CoV-2 vaccines. This delivery method exploits the anionic nature of nucleotides. To enhance the stability of the genetic cargo, nucleotides are bound to cationic liposomes (forming structures called lipoplexes), which increase the cellular uptake by exploiting the electrostatic interaction with negatively charged glycoproteins and proteoglycans of the cell membrane. Challenges occur because lipid-based vectors are often not sufficiently effective [143]. As previously stated, these are extensively utilized in gene therapies, particularly in the development of RNAi and mRNA vaccines, including those used for the treatment of SARS-CoV-2, as exemplified by the vaccines created by BioNTech/Pfizer and Moderna. Despite their efficacy as vaccines, it is estimated that only 2% of lipid vectors that reach a cell are able to deliver their cargo to the cytosol, primarily due to the shortened half-life in the blood. Additionally, the potential immunotoxicity of cationic lipids provides insights for the improvement of these formulations [141, 144].

1.4.2.2. Polymer-based vectors

In contrast to lipid-based vectors which typically rely only on electrostatic interactions to bind nucleic acids, biodegradable polymer-based vectors can bind the nucleic acid by exploiting electrostatic interactions and also physically entrap it. In the first case, cationic polymers, including polyethyleneimine (PEI) [145] and chitosan are combined with nucleic acid to form nanosized complexes termed polyplexes which exhibit enhanced stability compared to lipoplexes [141]. This approach is advantageous, particularly in regard to the capacity to deliver both small and large pDNA [81]. Focusing on nanoparticles, these latter can entrap the nucleic acid during the synthesis of the particles. Among the most extensively studied and previously cited polymers, PLGA has been successfully employed for the development of platforms loaded with a range of nucleic acid-based therapies, including RNAi and pDNA. PLGA vectors effectively protect nucleic acids from degradation, allowing for controlled release into the cytoplasm and sustained gene expression for periods exceeding one month. This capability has been demonstrated by various studies both *in vitro* and *in vivo*. PLGA vectors are capable of encapsulating both large nucleic acid cargoes, such as pDNA, and small ones, like siRNA. Nevertheless, short oligonucleotides frequently demonstrate burst release kinetics, which may result in off-target delivery *in vivo* [144].

1.4.3. Nucleic acid-loaded nanoparticles delivery into the cell

The primary obstacles to the systemic administration of DNA-based therapies are the potential degradation of the therapeutic gene by endonucleases and the process of cellular entry (Figure 1.15).

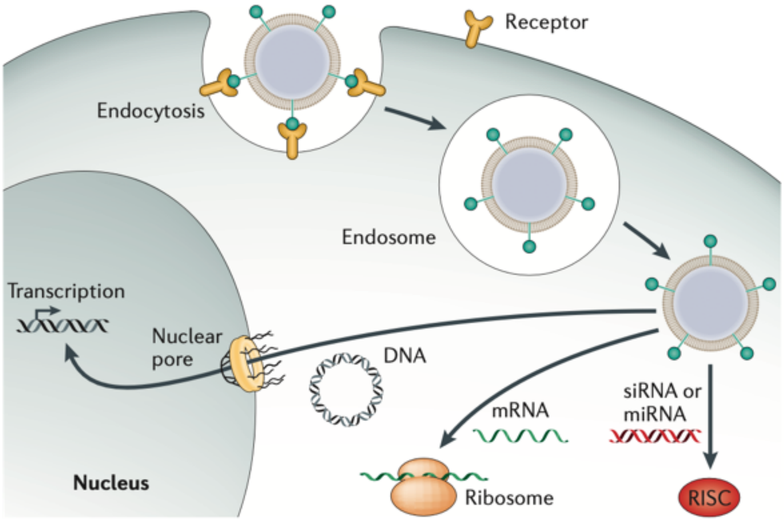

Figure 1.15. Barriers to successful delivery of nucleic acids using non-viral vectors. Non-viral vectors can be employed to facilitate the delivery of nucleic acids by initially mediating cellular uptake through endocytosis mechanisms. These vectors also afford protection to the genetic cargo and facilitate compartmental escape as the endosome undergoes a gradual acidification. Subsequently, siRNA and miRNA must be loaded into the RNA-induced silencing complex (RISC) within the cytosol, whereas mRNA must bind to cellular ribosomes to promote translation. In contrast, DNA requires nuclear translocation. Yin et al., 2014, modified.

Nanoparticles typically enter cells via endocytosis, whereby they are enclosed in a membrane and engulfed into an intracellular vesicle that matures through the endo/lysosomal pathway [146]. The primary mechanisms of nanoparticle uptake include clathrin-mediated endocytosis, clathrin-independent carrier pathways, macropinocytosis, and phagocytosis. Although caveolin-mediated endocytosis has been widely documented, emerging evidence indicates that it may not be a predominant pathway for cellular uptake [147]. In targeted systems, endocytosis in nonphagocytic cells is typically associated with clathrin-mediated or independent endocytosis. Conversely, nonspecific binding and internalization of particles frequently occur through macropinocytosis, which is often linked to membrane turnover [144].

The vesicles that are formed during the process of endocytosis fuse with the early endosomes and then gradually mature into the late endosomes through the process of acidification. Ultimately, these late endosomes combine with the lysosomes. Lysosomes are acidic organelles with a pH of approximately 5 and contain a variety of enzymes. Consequently, if nanocarriers loaded with nucleic acids do not escape promptly, both the carrier and its cargo will be degraded in the harsh lysosomal environment [148]. Endosomal escape represents a significant obstacle to improving therapeutic efficacy. However, the underlying mechanisms governing this process remain poorly understood [149]. In this context, several proposed strategies for endosomal escape have been discussed in the literature [144].

While numerous nucleic acid therapeutics function in the cytoplasm (i.e., mRNA, miRNA, siRNA), double-stranded DNAs (i.e., pDNA) act within the nucleus. The process of crossing the nuclear envelope, particularly in non-dividing cells, remains a significant challenge. In cells undergoing mitosis, nuclear entry is facilitated by the disassembly of the nuclear envelope [150]. However, numerous target cells for gene therapy do not undergo mitosis during the transfer of genetic material, necessitating the use of active transport mechanisms. Active transport into the nucleus is achieved through the nuclear pore complex, which is a group of proteins that regulate nuclear entry in a tightly controlled manner [151]. However, a study by Lechardeur et al. revealed that the half-life of DNA delivered in HeLa cells' cytoplasm is approximately 90 minutes, resulting in rapid DNA degradation and a consequent reduction in the amount of DNA available for nuclear entry [152]. On these bases, it appears that mRNA-based therapy may offer a more advantageous approach, given that mRNA transcripts have been shown to exhibit relatively high transfection efficiency and low toxicity, thus avoiding the need for nuclear entry and ensuring functional activity. Nevertheless, mRNA does not pose the risk of opportunistic insertional mutagenesis. However, the instability of mRNA structure and its susceptibility to ubiquitous RNases, in comparison to DNA, have diminished the potential of mRNA-based therapeutics to combat diseases [153], with major applications in the vaccine context [154].

1.4.4. *Ex vivo* or *in vivo* gene therapy?

The aforementioned delivery methods are employed in disparate approaches to gene therapy administration, specifically *ex vivo* or *in vivo*.

In the *ex vivo* method, specific cell types are harvested from either the patient (autologous) or a donor (allogeneic). A vector is then employed to deliver the therapeutic gene into the cells. Following potential activation or expansion, the transduced cells are reintroduced into the patient (Figure 1.16). In the majority of cases, stem cells are the primary focus of this approach, as the genetically modified cells can rapidly replace cells with a dysfunctional gene. This strategy allows for the use of both viral vectors and non-viral approaches, thereby conferring significant advantages. Additionally, the potential for toxic effects on cells is less critical in *ex vivo* gene therapy, as researchers can select undamaged, edited cells for reintroduction. Accordingly, the capacity to select and refine the cells of interest prior to transplantation holds significant therapeutic implications, ensuring the desired characteristics of the cells and providing flexibility in choosing from a diverse range of vectors. This approach has yielded remarkable outcomes in patients with hematological malignancies, as evidenced by the use of CD19-targeted CAR-T cells. However, is necessary to consider that this approach requires the availability of highly specialized facilities and personnel with extensive experience. In fact, despite the previously cited advantages, the *ex vivo* method of genetic manipulation involves several significant limitations. Firstly, the approach is restricted to certain types of cells, and only a small percentage of cells can be effectively modified using this approach. Furthermore, the *ex vivo* process is intricate and expensive. With regard to the potential applications, this method is particularly well-suited to the treatment of blood diseases and infectious diseases such as HIV, as well as the enhancement of cancer immunotherapy. At present, a considerable number of clinical trials are being conducted for gene editing therapies based on the *ex vivo* approach. These trials are focused on the optimization of delivery methods through the use of a range of gene editing platforms. The trials typically target blood cells for the treatment of blood disorders and T cells for cancer immunotherapy, particularly CAR-T cell therapies. In contrast, the *in vivo* method requires less extensive laboratory work and is more straightforward in terms of applications [139, 143, 155].

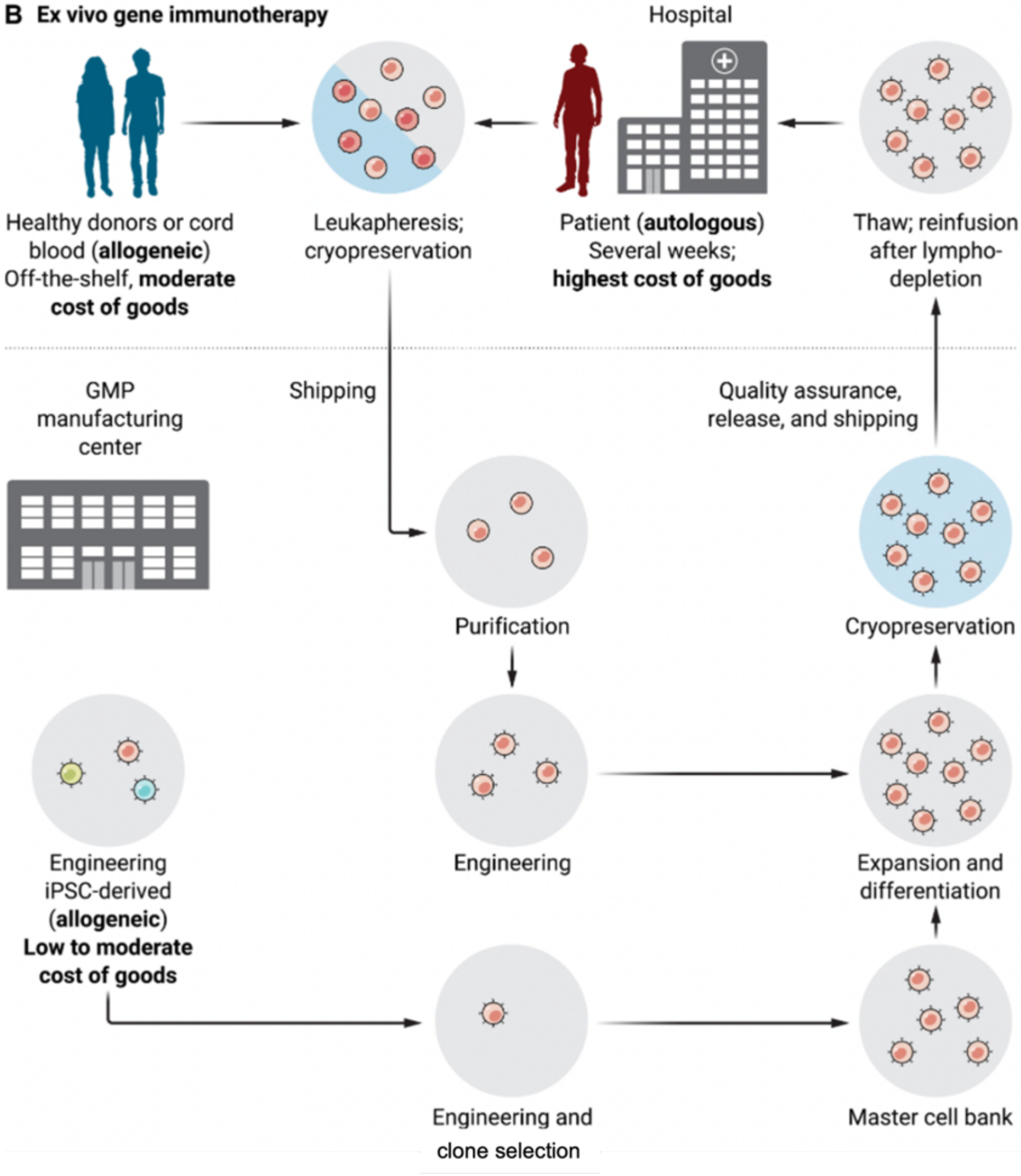

Figure 1.16. *Ex vivo* workflow for immune cell therapies. *Ex vivo* workflows for producing immune cell therapies are characterized by their complexity, time-consuming nature, and multi-institutional processes. The use of allogeneic donor cells, which can include cells from healthy donors or cord blood, as well as materials derived from induced pluripotent stem cells (iPSCs), enables the development of off-the-shelf therapies but inherently adds complexity to the process. Mai et al., 2022, modified.

In vivo gene therapy entails the direct introduction of a viral or non-viral vector into a patient's body, obviating the necessity for cellular intermediaries (Figure 1.17). This approach allows the gene transfer process to occur within the body, either directly into an organ or through the vascular system in proximity to the target organ [156].

Therefore, the primary objective is to achieve not only high efficiency but also to minimize therapy-related toxicity. In contrast to *ex vivo* approaches, *in vivo* gene therapy does not entail the additional steps of harvesting, modifying, and reintroducing the patient's cells, simplifying the therapeutic process and reducing costs. However, this method presents several challenges, including the potential for the patient's immune system to react to the viral vectors, difficulties in targeted delivery of genetic material to the cell and nucleus, low efficiency of non-viral delivery systems, potential toxicity, and often short-term effects. *In vivo* approaches are typically employed to treat or develop therapies for monogenic diseases affecting organs such as the liver, eyes, lungs, and muscles. The advancement of gene editing-based therapies to clinical trials has been hindered by concerns regarding the potential adverse effects on patients resulting from the administration of gene editing *in vivo* [143]. *In vivo*, gene manipulation represents a crucial approach when cells are not separable from the body or are unable to survive *ex vivo* for an extended period. Moreover, the *in vivo* method is most appropriate for easily accessible tissues. Nevertheless, the non-specific contact of the vector with cells and the elevated risk of immune reactions have constrained its application [155, 157].

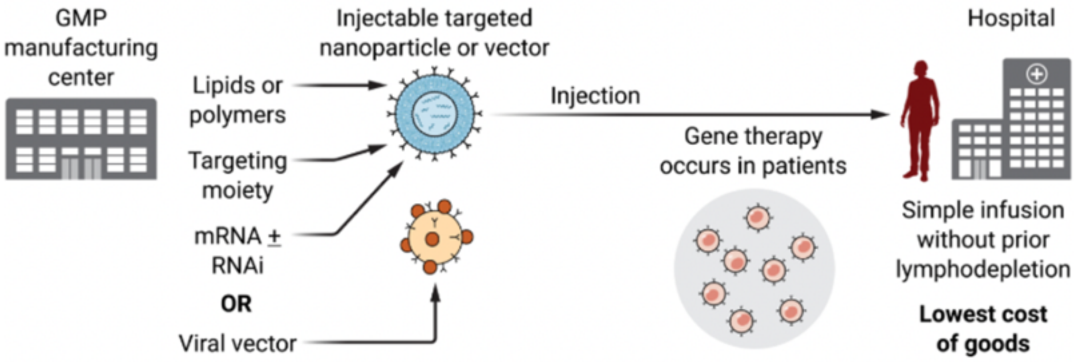

Figure 1.17. *In vivo* workflow for immune cell therapies. *In vivo* gene therapy involves scalable and efficient treatment of patients through the administration of targeted gene immunotherapy carriers directly to the patient's tumor or immune cells. Mai et al., 2022, modified.

From 2010 to 2020, there were 1,035 (54%) clinical trials for *ex vivo* gene therapy and 872 (45%) for *in vivo* gene therapy, which provides substantial evidence to support the remarkable advancement in this field. Surely, further studies are necessary to yield significant advancements and expand the potential applications [139].

Recently, nanoparticles have been the subject of investigation as potential gene delivery systems, given their favorable properties in terms of safety, non-immunogenicity, controllability, and cost-effectiveness, which make them particularly advantageous for this application. Despite the extensive research conducted thus far, nanoparticle-based gene therapies are still in the early stages of development, with the majority of studies still in the trial or preclinical phases [158-160].

Given the aforementioned considerations, it is of interest to pursue a strategy that combines targeted nanocarriers, gene therapy, and therapeutic antibodies, as an alternative to traditional immunotherapy for B-cell malignancies, which involves the injection of therapeutic antibodies into the bloodstream or CAR-T cells. In this manner, a novel therapeutic approach may be developed based on biodegradable nanoparticles, equipped with an antiCD19 specific targeting mechanism and containing a pDNA coding for an antiCD20 therapeutic antibody. This approach would allow for the specific induction of local protein production in the B-cell TME, with the objective of transforming cells within the body into "*in situ* bioreactors."

2. Aim of the project

BL is a highly aggressive B-cell NHL that predominantly affects children and adolescents, accounting for 1-2% of all NHL cases. The use of immunotherapy approaches, such as Rituximab, an antiCD20 antibody, has led to a notable improvement in survival outcomes, with long-term complete remission achieved in 95% of patients. However, it is crucial to emphasize that Rituximab can also act on normal B cells, potentially leading to B-cell depletion and subsequent effects on antibody production, cytokine networks, B-cell-mediated antigen presentation, and activation of T cells and macrophages.

In light of the aforementioned considerations, it is of interest to pursue a strategy that combines targeted nanocarriers, gene therapy, and therapeutic antibodies, as an alternative to traditional antibody-based immunotherapy for B-cell malignancies. This approach would enable the targeted induction of protein production in the B-cell TME, with the objective of transforming specific cells within the body into "*in situ* bioreactors," thereby reducing the incidence of adverse effects.

The planned strategies and the related main points to reach the proposed purposes are summarized below:

- To demonstrate the efficacy of an antiCD19 recombinant antibody as a targeting mechanism to address tumoral B cells;
- To develop and characterize an optimal DNA delivery system based on biodegradable nanocarriers equipped with an antiCD19 targeting mechanism to facilitate the selective delivery of the treatment to target cells;
- To demonstrate the effectiveness of this nanoplatform in ensuring target cell transfection, both *in vitro* and *in vivo*;
- To evaluate the ability of this DNA-loaded nanoplatform to induce the production of a therapeutic protein, represented by an antiCD20 recombinant antibody, within the TME, thereby modifying it and obtaining a subsequent therapeutic effect.

The conceptualization, production, and characterization, both *in vitro* and in animal models, of this nanotechnological approach for the treatment of BL were summarized in the data collected during the PhD period.

3. Materials and methods

3.1. Cells culture and count

BJAB (BL cell line), NALM-6 (B-ALL cell line), JURKAT (T-ALL cell line) and RPMI-8226 (Plasmacytoma cell line) were defrosted warming the cryovial at 37°C, then 5 mL of culture medium were added to cells to eliminate Dimethylsulfoxide (DMSO, Sigma-Aldrich Co., St Louis, MO, USA), and cells were centrifuged for 5 minutes at 400 g. Cells were maintained in suspension in Roswell Park Memorial Institute 1640 (RPMI-1640, Sigma-Aldrich Co.) medium supplemented with 10% (v/v) fetal bovine serum (FBS, Sigma-Aldrich Co.), 100 µg/mL streptomycin (Sigma-Aldrich Co.), and 100 U/mL penicillin (Sigma-Aldrich Co.). Cells were incubated at 37°C in a humidified atmosphere with 5% CO_2. Fresh medium was substituted every 48 hours. To count cells, the trypan blue (TB) exclusion assay was used; cells were diluted 1:1 (v/v) with TB and counted with the Bürker chamber and defining the number of cells per mL of culture medium in accordance with the following formula:

$$Quadrant1 + Quadrant2 + Quadrant3 \times (dilution\ with\ TB) \times 10{,}000\ (conversion\ factor) = cells/mL$$

3.2. Production of the targeting mechanism (antiCD19 scFv-Fc) and therapeutic protein (antiCD20 scFv-Fc)

The design of the antiCD19 scFv takes the cue from the VH and VL regions of MOR208 (Patent n°: US 2014/0227277 A1), also known as Tafasitamab, a Fc-modified, humanized, antiCD19 antibody; instead, the design of the antiCD20 scFv takes the cue from the VH and VL regions of 2B8 (Patent n°: N.5,736,137), also known as Rituximab. The monoclonal Chinese Hamster Ovary (CHO) cell population transfected with the vector pcDNA3.1/Hygro+ (Thermo-Fisher Scientific, Waltham, MA, USA) coding for the targeting mechanism (scFv of MOR208 linked to a human Fc) or the therapeutic protein (scFv of 2B8 linked to a human Fc) were cultured in the CELLine^{TM} Device bioreactor (BD Biosciences, New Jersey, USA.), to maximize production. The culture started by adding ~15x10^6 cells to the cultivation chamber of the bioreactor in ExpiCHO™ Expression Medium (Sigma-Aldrich Co.). Twice a week, the supernatant containing the high concentration of targeting mechanism or therapeutic protein produced by cells was collected from the cultivation chamber and replaced with fresh cells. The medium of the chamber was changed every 2 weeks. The collected supernatant was centrifuged at

1,500 g for 20 minutes to remove any debris, and the resulting sample was stored at -20°C. Once a sufficient quantity of collected supernatants had been obtained, the targeting mechanism or the therapeutic protein were purified by protein “A” affinity chromatography. Finally, the fractions containing the purified targeting mechanism, or the therapeutic protein were dialyzed overnight in PBS at 4°C. The final concentration of the targeting mechanism (antiCD19 scFv-Fc, defined antiCD19) or therapeutic protein (antiCD20 scFv-Fc, defined antiCD20) after dialysis was quantified by absorbance assay at 280 nm using a spectrophotometer (Eppendorf BioPhotometer Plus, Milan, Italy).

3.2.1. SDS-Page and Western Blot of antiCD19

AntiCD19 (300 ng) was diluted in non-reducing or reducing 4x Laemmli Sample Buffer (Bio-Rad Laboratories, CA, USA) and boiled for 5 minutes. Samples were resolved on SDS-polyacrylamide gel. For the SDS-Page analysis, the gel was stained in Coomassie Blue, while for the Western Blot analysis, the separated proteins were transferred to a nitrocellulose membrane (GE HealthCare, Chicago, IL, USA). Following a blocking step of 45 minutes with 2% skim milk in PBS at room temperature, the membrane was incubated for 1 hour at room temperature with an alkaline phosphatase-conjugated anti-Human IgG antibody (Sigma-Aldrich Co., final concentration 2 ng/µL). After three washes, with PBS-Tween 20 0.1% and three with PBS, the membrane was developed with BCIP and NBT (Sigma-Aldrich Co.) in alkaline phosphatase buffer (100 mM Tris-HCl, 0.1 M NaCl, 5 mM $MgCl_2$, pH 9.6).

3.3. Synthesis of PLGA-PVA nanoparticles

PLGA-PVA nanoparticles (NPs) were synthesized by the double emulsion solvent evaporation method described by Vasir and Labhasetwar [161] with modifications. Briefly, PVA (Sigma-Aldrich Co., molecular weight. 30,000-70,000, 87-90% hydrolyzed) dissolved 1 mg/mL in MES buffered saline (0.1 M MES, 0.9% NaCl, pH 4.7) was covalently linked to 300 µg of antiCD19, through the EDC/sulfo-NHS crosslinking protocol (Thermo-Fisher Scientific) and then added to 4 mL of 2% (w/v) PVA solution in cold 10 mM Tris -1 mM EDTA, pH 8 (TE buffer). After, PLGA (30 mg, Sigma-Aldrich Co., molecular weight 30,000-60,000, lactide: glycolide 50:50) was dissolved in 1 mL of chloroform (Sigma-Aldrich Co.). To start the synthesis, 300 µL of TE buffer or FITC-bovine serum albumin (BSA, 20 mg/mL in TE buffer, Sigma-Aldrich Co.) or pEGFP-N1

(1.7 mg/mL in TE buffer, #V012021, NovoPro) or pAntiCD20 (1.7 mg/mL in TE buffer) or Cyanine 5.5 (3 mg/mL in TE buffer, Cytiva, Global) were added to the PLGA solution and vortexed and sonicated (30 seconds at 15 W of the maximum power) with Bandelin Sonopuls HD 2070 (Bandelin electronic GmbH & Co. KG, BER, Germany) to form the primary emulsion. The obtained emulsion was added to the PVA solution and sonicated for 1 minute as described above to form a secondary emulsion. The resulting emulsion was stirred (750 rpm) overnight to allow for chloroform evaporation. NPs were collected by centrifugation at 12,000 g for 30 minutes at 4°C and the pellet was washed in TE buffer. Finally, NPs were resuspended in 2 mL of PBS filtered 0.2 µm and stored at 4°C. The production of untargeted NPs was conducted in accordance with the same protocol but skipping the antibody coupling step.

3.4. Characterization of nanoparticles

3.4.1. Dynamic Light Scattering (DLS)

Particle size (average diameter), polydispersity index, and surface charge (zeta potential) were determined by the DLS technique using Zetasizer Nano ZSP (Malvern Panalytical, Malvern, UK). NPs were diluted 1:200 (v/v) in H_2O MilliQ filtered 0.2 µm and measurements were done at 37°C and a scattering angle of 173°.

3.4.2. Scanning Electron Microscopy (SEM)

NPs were diluted 1:50 (v/v) in H_2O MilliQ filtered 0.2 µm. A drop of the sample was deposited on a glass coverslip and left to dry at room temperature. Glass coverslips were mounted on aluminum stubs coated with double-sided carbon tape. Samples were carbon coated using the Q150T ES plus sputter coater (Quorum Technologies, Laughton, UK). Samples were analyzed using a Gemini 300 SEM (Zeiss, Oberkochen, Germany, UE), working in secondary electron mode, at an acceleration voltage and a working distance of 2 kV and 3 mm.

3.4.3. Cryogenic Electron Microscopy (Cryo-EM)

TEM grids (C-Flat 1.2/1.3 Cu 300, Protochips) were treated by glow discharge with PELCO easiGlow (Ted Pella, Inc., CA, USA) for 45 seconds and with 20 mA to make grids hydrophilic and mounted inside the Vitrobot instrument (Thermo-Fisher Scientific). NPs were diluted 1:100 (v/v) in PBS and 4 µL were deposited onto the grid. The Vitrobot automatically performed the plunge freezing by blotting: after a few microliters of NPs were adsorbed onto a grid, the sample was blotted with filter paper to make a thin aqueous layer and then plunge frozen into liquid ethane for instant vitrification. The blotting was done at 20°C, with humidity of 95%, and for 3 seconds blot time. Then, TEM grids were placed inside the sample holder and kept at the temperature of liquid nitrogen. Finally, the grids were clamped and inserted in the Cryo-EM microscope Glacios (Thermo-Fisher Scientific) for the imaging.

3.4.4. Nanoparticle Tracking Analysis (NTA)

NTA was performed using NanoSight LM10 (Malvern Panalytical, Lissone, Italy) diluting NPs 1:4000 (v/v) in H_2O milliQ immediately before the measurements.

3.4.5. Enzyme-linked immunosorbent assay (ELISA) for the evaluation of the antiCD19 coating on the surface of nanoparticles

ELISA wells were coated overnight at 4°C with an anti-Human IgG antibody (Sigma-Aldrich Co., #AP112, final concentration 2 ng/µL in a final volume of 100 µL/well). The unbound sites were blocked by incubation with 2% skim milk in PBS for 1 hour at room temperature with 150 µL/well. Following three washes with PBS-Tween 20 0.1% and three with PBS, the plate was incubated for 1 hour at room temperature with different amounts (5-10-25 µL of NPs in a final volume of 100 µL/well). Following washes, the presence of antiCD19 was revealed through an alkaline phosphatase-conjugated anti-Human IgG antibody (Sigma-Aldrich Co., #A9544, final concentration 4 ng/µL) which was added for 1 hour at room temperature in 100 µL/well. After washes, the alkaline phosphatase substrate p-Nitrophenyl phosphate (PNPP, 1 mg/mL, Sigma-Aldrich Co.) in glycine buffer (0.1 M glycine, 0.1 mM $MgCl_2$, and 0.1 mM $ZnCl_2$, pH 9.6) was added to develop the reaction. The optical density (OD) was read at 405 nm with ELISA Reader TECAN Infinite M200 (Tecan Italia S.r.l., Milan, Italy).

3.4.6. Western Blot for the evaluation of the integrity and quantification of antiCD19 coating on the surface of nanoparticles

30 µL of NPs were centrifuged at 8,000 g for 5 minutes. Following the removal of the supernatant, NPs were resuspended in 15 µL of non-reducing 4x Laemmli Sample Buffer (Bio-Rad Laboratories) and boiled for 30 minutes. The positive control of purified antiCD19 (300 ng) was diluted in the same buffer and then boiled for 30 minutes. Samples were resolved on SDS-polyacrylamide gel and transferred onto a

nitrocellulose membrane (GE HealthCare). Following a blocking step of 45 minutes with 2% skim milk in PBS at room temperature, the membrane was incubated for 1 hour at room temperature with an alkaline phosphatase-conjugated anti-Human IgG antibody (Sigma-Aldrich Co., #A9544, final concentration 2 ng/µL). After three washes, with PBS-Tween 20 0.1% and three with PBS, the membrane was developed with BCIP and NBT (Sigma-Aldrich Co.) in alkaline phosphatase buffer. The same protocol was employed to evaluate the antiCD19 coupling efficiency, with samples resuspended in reducing 4x Laemmli Sample Buffer. The intensity of the bands was quantified using a ChemiDoc Imaging System (Bio-Rad Laboratories). A calibration curve was constructed using note amounts (600-300-150-75-37.5 ng) of purified antiCD19 with the resulting band intensities plotted against the note amounts. The linear regression coefficient (R^2) was determined to be 0.99. The total amount of bound antiCD19 was calculated by interpolation of the intensity of bands relative to the samples of NPs to the calibration curve. The total number of antiCD19 in the preparation was calculated using the molecular weight of the molecule. The number of bound antiCD19 per NP was calculated by dividing the total number of antiCD19 by the total number of NPs in the preparation, as determined by NTA.

3.4.7. CH50 screening assay

Functional activity of the complement system was performed by measuring complement hemolytic activity 50% (CH50) on sensitized mutton erythrocytes (EA, Microbiol S.r.l., Cagliari, CA, Italy) as previously described [105]. Briefly, normal human serum (NHS, 100 µL) and NPs (8 µL) were incubated for 2 hours at 37°C under shaking conditions (750 rpm). Then samples were centrifuged for 5 minutes at 8,000 g, and the supernatants were diluted in Complement Fixation Diluent (CFD, 142 mM NaCl, 5 mM Na-5-5-diethylarbiturate, 0.5 mM $MgCl_2$, 0.05% agar, 0.01% NaN_3, 10 mM EGTA). The samples were then diluted 1:50, 1:100, 1:200, and 1:400 (v/v) to a final volume of 200 µL. Subsequently, 50 µL of EA 1% were added to each sample and incubated for 30 minutes to activate the classical complement pathway. The total lysis is represented by EA 1% diluted in H_2O, while the blank is represented by EA 1% diluted in CFD. The reaction was terminated by the addition of EDTA (final concentration 20 mM). The percent lysis was quantified at 415 nm with an ELISA Reader TECAN Infinite M200 (Tecan Italia S.r.l.) after centrifugation at 12,000 g for 1 minute. Complement activation was checked by preparing a standard curve using NHS as a positive control. The percentage of lysis was calculated using the following formula:

$$\text{Lysis (\%)} = \frac{OD\ 415\ Sample - OD\ 415\ Blank}{OD\ 415\ Total\ lysis - OD\ 415\ Blank} \text{ x } 100$$

The percentage of lysis was plotted against the serum dilution, and the dilution required for 50% hemolysis was calculated. The CH50 (U/mL) provides the number of hemolytic units present in 1 mL of NHS.

3.4.8. Hemolytic assay

Direct erythrocyte lysis was performed by incubating 1% EA (Microbiol S.r.l.) with NPs (8 µL) diluted in CFD for 2 hours at 37°C under shaking conditions (750 rpm). The percentage of lysis was calculated as described in the paragraph “3.4.7. CH50 screening assay”.

3.4.9. Clotting test

NPs (4 µL/well), and normal human-citrate anticoagulated plasma (NHP, 80 µL/well) were seeded in a 96-well plate. To assess the clotting capacity of NPs, $CaCl_2$ (final concentration 20 mM) was added to initiate the clotting reaction. The eventual coagulation resulted in an increase in the turbidity of the well, which was read at 405 nm every 2 minutes for 70 minutes with an ELISA Reader TECAN Infinite M200 (Tecan Italia S.r.l.). The half-coagulation time is defined as the point at which 50% of the coagulation process has occurred.

3.4.10. Cell viability test

BJAB or JURKAT (1000 cells/µL) were incubated for 24 hours at 37°C under shaking (800 rpm) with 10 µL of NPs in a final volume of 200 µL of RPMI-1640 supplemented medium. 20 µL of 3-(4,5-dimethylthiazol-2-yl)-2,5-diphenyltetrazolium bromide (MTT, 5 mg/mL, Sigma-Aldrich Co.) were subsequently added, and samples were incubated for 4 hours at 37°C under shaking conditions (800 rpm). Afterward, samples were centrifuged for 3 minutes at 20,000 g to precipitate all the formazan crystals. The supernatant was removed, and the deposited crystals were solubilized in 200 µL of DMSO (Sigma-Aldrich Co.). The OD was measured at a wavelength of 570 nm ELISA Reader TECAN Infinite M200 (Tecan Italia S.r.l.). The viability percentage was calculated using untreated cells as a reference point, with 100% represented by the untreated control group. This was expressed as a percent of mitochondrial activity.

3.4.11. Encapsulation efficiency and fluorescence quantification of nanoparticles

The fluorescence signal corresponding to the FITC-BSA (maximum excitation/emission 495/519 nm) or Cyanine 5.5 (Cy5.5, maximum excitation/emission 683/703 nm) was acquired with ChemiDoc Imaging System (Bio-Rad Laboratories) and expressed as corrected total cell fluorescence (CTCF) calculated according to the following formula:

$$\text{CTCF} = \text{IntegratedDensity} - [(\text{Area}_{\text{Region Of Interest, ROI}}) \times (\text{MeanFluorescence}_{\text{Background}})]$$

The CTCF corresponding to the unencapsulated compound was interpolated with a FITC-BSA or Cy5.5 calibration curve (0.07-0.15-0.31-0.62-1.25 mg/mL for FITC-BSA and 24-12-6-3 µg/mL for Cy5.5), to extrapolate the amount of FITC-BSA or Cy5.5 unencapsulated. The encapsulation efficiency (EE%) was calculated indirectly using the following formula:

$$\text{EE (\%)} = \frac{Total\ amount\ of\ compound - unencapsulated\ compound}{Total\ amount\ of\ compound} \text{ x } 100$$

The fluorescence signal corresponding to the FITC-BSA loaded NPs was acquired with a ChemiDoc Imaging System (Bio-Rad Laboratories) immediately after synthesis and after 1 year. The data were expressed as CTCF.

3.4.12. *In vitro* release

The release profile of the FITC-BSA-loaded NPs was analyzed in 50 µL of PBS or NHS diluted 1:10 in PBS, or cytosol mimic buffer [83] (142 mM KCl, 5 mM NaCl, 5 mM $MgCl_2$, 25 mM Hepes-KOH, pH 7.2, 1 mg/mL BSA) at 4°C or 37°C under shaking conditions (750 rpm) over 0.5-1 hours. Subsequently, the samples were centrifuged at 8,000 g for 5 minutes. Following this, a standard volume of the supernatant was collected, and the fixed volume was maintained by the addition of the same volume at each subsequent time point. The release was indirectly quantified by interpolating the fluorescent signal (expressed as CTCF) corresponding to the released compound with a FITC-BSA calibration curve thereby extrapolating the amount of FITC-BSA released as described in the paragraph "3.4.11. Encapsulation efficiency and fluorescence quantification of NPs".

3.4.13. FITC-BSA fluorescence sensibility at different pH

FITC-BSA-loaded NPs or FITC-BSA were diluted 1:10 (v/v) in 0.9% NaCl, pH 4-8 for 1 hour. The fluorescence signal was acquired using a ChemiDoc Imaging System (Bio-Rad Laboratories). The fluorescence signal was expressed as CTCF, and the fluorescence variation was quantified by setting the fluorescent signal at pH 8 (standard conditions) as the 100% reference.

3.4.14. Human whole blood-endothelial cell model for the evaluation of nanoparticles toxicity

Whole blood sampling, plasma preparation, human lung microvascular endothelial cells (HLMVECs; Cell Applications Inc, San Diego, CA) culturing, incubation of NPs on HLMVECs in combination with the human whole blood model, immunoassays, and flow cytometry tests were performed as described in [162]. Whole blood sampling and analysis were performed according to the ethical guidelines from the Declaration of Helsinki. Informed written consent was obtained from all blood donors. The study was approved by the ethical committee of the Norwegian Regional Health Authority, ethical permit REK#S-04114, 2010/934. In brief, HLMVECs were cultured up to passage 5, before seeding to 48-well cell culture plates. After 2-3 days of daily growth medium exchanges, cells were washed with 37°C PBS and incubated with 300 µL of lepirudin-anticoagulated (final concentration 50 µg/mL) whole blood pre-mixed with 60 µL NPs for 4 hours at 37°C, 5% CO_2 and 50 rpm shaking. 10 µL whole blood was isolated after 15 minutes for monocyte and granulocyte flow cytometry. EDTA was added to a final concentration of 20 µM after sampling. After 4 hours of incubation, whole blood was isolated and supplemented with EDTA (final concentration 20 mM). One 10 µL-aliquot whole blood was isolated for platelet flow cytometry, also supplemented with 10x CTAD (8 mM trisodium citrate, 1.1 M theophylline, 26 mM adenosine, 14 mM dipyridamole; Greiner Bio-One, Kremsmünster, Austria) to limit any further platelet activation. Plasma was prepared from the remaining whole blood by centrifugation at 3,000 g for 15 minutes at 4°C. All plasma samples were kept at -80°C before immunoassays. Granulocytes, monocytes, platelets, and HLMVECs were analyzed on an Accuri C6 (BD Biosciences, Franklin Lakes, NJ), and data was analyzed with FlowJo, version 10

(Tree Star, Ashland, OR). The complement activation markers C3b/C3c, as a marker of C3-cleavage, and the soluble terminal complement complex sC5b-9 were analyzed as described in [163-165]. Platelet factor-4 (PF-4) and neutrophil-activating peptide-2 (NAP-2) were analyzed with ELISA DuoSets (R&D Systems, Minneapolis, MN). Tecan plate reader Sunrise (Tecan Nordic, Stockholm, Sweden) was used for absorbance measurement, and Magellan software, version 7.1 (Tecan Nordic AB), was used for data analysis. Cytokines IL-1β, IL-6, IL-8, and Tumor Necrosis Factor (TNF) with a 4-plex kit (R&D systems). Blood cell counts were acquired with Swelab Alfa blood cell counter (Boule International, Spånga, Sweden) according to the manufacturer's instructions.

3.4.15. Agarose gel electrophoresis

pDNA topology and encapsulation by NPs were investigated by agarose gel electrophoresis. NPs were resuspended 1:1 (v/v) in chloroform (Sigma-Aldrich Co.) and incubated for 90 minutes at 37°C under shaking conditions (750 rpm). Samples were diluted 1:2 (v/v) with cold TE buffer, vortexed for 1 minute, and centrifuged for 5 minutes at 12,000 g. The aqueous phase which contained the pDNA, was recovered and subjected to electrophoresis on a 1% agarose gel in TAE buffer (40 mM Tris, 1 mM EDTA, 20 mM acetate, pH 8.6) containing SYBR Safe DNA gel staining dye (Thermo Fisher Scientific), for 30 minutes. pDNA was visualized with a ChemiDoc Imaging System (Bio-Rad Laboratories).

3.5. Flow cytometric analysis

3.5.1. Binding of antiCD19 and antiCD20 on cells

BJAB, NALM-6, JURKAT and RPMI-8226 (250,000 cells) were incubated with antiCD19 (final concentration 5 ng/µL) or with antiCD20 (final concentration 10 ng/µL) at 37°C for 1 hour in PBS added with 2% BSA, 0.7 mM $CaCl_2$ and 0.7 mM $MgCl_2$ under shacking (750 rpm); then, three washes were performed to eliminate the excess of primary antibody and cells were incubated with the secondary FITC-conjugated anti-Human IgG antibody (Sigma-Aldrich Co., dilution 1:2000) at 37°C for 1 hour under shacking. In the end, cells were washed to remove the excess antibody and fixed in 1% paraformaldehyde diluted in PBS added with 2% BSA, 0.7 mM $CaCl_2$ and 0.7 mM $MgCl_2$. The binding on the surface of cells was evaluated by flow cytometric analysis which was performed by Attune® NxT Acoustic Focusing flow cytometer (Thermo

Fisher Scientific), acquiring 10,000 events; data were analyzed with Attune NxT Software.

3.5.2. Binding and internalization of nanoparticles in cells

BJAB or JURKAT (250,000 cells) were resuspended in 1 mL of RPMI-1640 supplemented medium and incubated at 37°C for 1 hour in rotation with 10 μL of FITC-BSA-loaded NPs. For the internalization studies, cells were treated with 100 μL of Pronase (2 mg/mL, Sigma-Aldrich Co.) for 30 minutes at 4°C. The interaction between the cells and NPs was evaluated by flow cytometric analysis performed with an Attune® NxT Acoustic Focusing flow cytometer (Thermo Fisher Scientific), acquiring 10,000 events; data were analyzed with Attune NxT Software. The percentage of positive cells with only bound NPs was calculated by subtracting the percentage of positive cells with only internalized NPs from that of positive cells with bound and internalized NPs. Similarly, the Mean Fluorescence Intensity of only internalized NPs was subtracted from that of bound and internalized NPs thereby obtaining the Mean Fluorescence Intensity of only the bound NPs.

3.5.3. *In vitro* transfection studies

BJAB or JURKAT (250,000 cells) were resuspended in 400 μL of RPMI-1640 supplemented medium and treated with NPs at a volume corresponding to approximately 3 μg of encapsulated pEGFP, at 37°C and 5% CO_2. Following a 24-hour incubation period, cells were washed with PBS and incubated for a further 96 hours with fresh medium. Transfection efficiency was evaluated by flow cytometric analysis performed on an Attune® NxT Acoustic Focusing flow cytometer (Thermo Fisher Scientific), acquiring 10,000 events; data were analyzed with Attune NxT Software.

3.5.4. Competition assay between Rituximab and antiCD20

BJAB (250,000 cells) were preincubated with Rituximab (final concentration 50 ng/μL) at 37°C for 30 minutes in PBS added with 2% BSA, 0.7 mM $CaCl_2$ and 0.7 mM $MgCl_2$ under shacking (750 rpm); then, three washes were performed to eliminate the excess of primary antibody and cells were incubated with antiCD20 (final concentration 10 ng/μL) at 37°C for 1 hour under shacking. Following washes, the mouse anti-SV5 antibody (dilution 1:2000) was incubated at 37°C for 1 hour under shacking. Finally, following washes, the secondary FITC-conjugated anti-Mouse IgG antibody (Sigma-

Aldrich Co., dilution 1:2000) was incubated at 37°C for 1 hour under shacking. In the end, cells were washed to remove the excess antibody and fixed in 1% paraformaldehyde diluted in PBS added with 2% BSA, 0.7 mM $CaCl_2$ and 0.7 mM $MgCl_2$. The binding on the surface of cells was evaluated by flow cytometric analysis which was performed by Attune® NxT Acoustic Focusing flow cytometer (Thermo Fisher Scientific), acquiring 10,000 events; data were analyzed with Attune NxT Software.

3.6. Immunofluorescence analysis

3.6.1. Binding of antiCD19 on cells

BJAB and NALM-6 (250,000 cells) were incubated with antiCD19 (final concentration 5 ng/μL) at 37°C for 1 hour in PBS added with 2% BSA, 0.7 mM $CaCl_2$ and 0.7 mM $MgCl_2$ under shacking (750 rpm); then, three washes were performed to eliminate the excess of primary antibody and cells were incubated with the secondary FITC-conjugated anti-Human IgG antibody (Sigma-Aldrich Co., dilution 1:2000) at 37°C for 1 hour under shacking. In the end, cells were washed to remove the excess antibody and fixed in 1% paraformaldehyde diluted in PBS added with 2% BSA, 0.7 mM $CaCl_2$, and 0.7 mM $MgCl_2$. Cells were then cytocentrifuged at 400 g for 5 minutes on a slide. The nuclei were stained with DAPI (dilution 1:200) for 5 minutes; the excess of DAPI was eliminated by 2 washes with PBS. Slides were covered with a mounting medium and a coverslip. Slides were analyzed using a fluorescence microscope Nikon Eclipse Ti-E live cell imaging system. Images were analyzed using Image-J software.

3.6.2. *Ex vivo* immunofluorescence on organ slides

Explanted organs were conserved at -80°C after embedding in the Killik solution (Bio Optica, Milan, Italy); then, they were cut through the cryostat with a section thickness of 14-16 μm. Sections were stored at -20°C. Organ sections were fixed in 4% paraformaldehyde and rehydrated in PBS for 5 minutes at room temperature. Slices were incubated with 50 μl of blocking solution for 30 minutes at room temperature. Then, the blocking solution was removed, and slices were incubated with:

- Rabbit anti-Mouse von Willebrand Factor antibody (Dako, Santa Clara, CA, USA, dilution 1:50) and FITC-conjugated anti-Rabbit IgG antibody (Thermo Fisher Scientific, dilution 1:2000)
- FITC-conjugated anti-Human IgG antibody (Sigma-Aldrich Co, dilution 1:200)

- Rat anti-Mouse C1q antibody (Hycult Biotech, Uden, Netherland, dilution 1:400) and FITC-conjugated anti-Rat IgG antibody (Sigma-Aldrich Co, dilution 1:30)
- FITC-conjugated anti-Mouse polymorphonuclear (PMN) cells antibody (Hycult Biotech, dilution 1:50)
- Rat anti-Mouse CD56 antibody (Sigma-Aldrich Co, dilution 1:50) and FITC-conjugated anti-Rat IgG antibody (Sigma-Aldrich Co, dilution 1:30)
- Rabbit anti-Mouse CD14 antibody (Santa Cruz Biotechnology, Dallas, Texas, USA, dilution 1:50) and FITC-conjugated anti-Rabbit IgG antibody (Thermo Fisher Scientific, dilution 1:2000)
- Rat anti-Mouse C3b/iC3b/C3c antibody (Hycult Biotech, dilution 1:400) and FITC-conjugated anti-Rat IgG antibody (Sigma-Aldrich Co, dilution 1:30)

at 37°C for 1 hour. Sections were stained with DAPI (1:200) for 5 minutes, washed, and covered with a mounting medium and a coverslip; organs were analyzed using a fluorescence microscope Nikon Eclipse Ti-E live cell imaging system Images were analyzed using Image-J software.

3.7. *In vivo* experiments on zebrafish embryos

3.7.1. Zebrafish embryos handling and maintenance

Fertilized zebrafish eggs were placed in E3 Medium (5 mM NaCl, 0.17 mM KCl, 0.33 mM $CaCl_2$, 0.33 mM $MgSO_4$) supplemented with 0.5% methylene blue and incubated at 28°C. At 24 hours post-fertilization (hpf), the eggs were manually dechorionated and placed in E3 Medium supplemented with Phenylthiourea (PTU, Sigma-Aldrich Co., final concentration 0.2 mM) to prevent melanogenesis and thus the pigmentation of the embryos. Zebrafish embryos were handled according to standard rules and procedures for animal wellness “https://zfin.org”. All experimental procedures involving animals were executed after Ministerial Approval NO1832SBL22.

3.7.2. Zebrafish lymphoma xenograft model

Zebrafish embryos were anesthetized using tricaine (Sigma-Aldrich Co., final concentration 0.02%) at 48 hpf and placed on agarose plates, after which the excess water was removed to facilitate injection. For the biodistribution studies, BJAB cells were labeled with Calcein Red Orange-AM (Calcein-AM, Thermo Fisher Scientific, maximum excitation/emission 577/590 nm) according to the manufacturer’s instructions. A total of approximately 2,500 BJAB cells were injected into each embryo, with a final volume of 9.2 nL in the perivitelline space using capillary glasses and a Nanoject II Auto-Nanoliter Injector (Drummond Scientific Co., Broomall, PA, USA). The process was conducted using a SteREO Microscope Discovery.V8 (Zeiss). Following the injection of cells, the embryos were maintained at 30°C and examined using the fluorescence microscope Nikon Eclipse Ti-E live system to ascertain the distribution of the injected cells. The images were subsequently analyzed using the ImageJ software.

3.7.3. Biodistribution studies of nanoparticles

Biodistribution studies of NPs were performed by injecting FITC-BSA-loaded NPs (4.6 nL/embryo) into the duct of Cuvier of zebrafish lymphoma xenograft models using capillary glasses and a Nanoject II Auto-Nanoliter Injector (Drummond Scientific Co.). At 0.5- and 24-hours post-injection (hpi), the biodistribution of the NPs was evaluated using a fluorescence microscope Nikon Eclipse Ti-E live system, and the resulting images were analyzed with ImageJ software. Subsequently, the fluorescence within the designated region of interest (ROI) was quantified for each embryo, and the CTCF was calculated as described in the paragraph "3.4.11. NPs encapsulation efficiency and fluorescence quantification".

3.8. Gene expression studies of Enhanced Green Fluorescent Protein (EGFP)

3.8.1. Gene expression studies of EGFP after *in vitro* transfection

Following a 24-hour incubation period with a volume of NPs corresponding to approximately 3 µg of encapsulated pEGFP, total RNA was extracted from BJAB and JURKAT cells with TRIzol® reagent (Life Technologies, Carlsbad, CA, USA). Subsequently, 1 µg of RNA was reverse transcribed using Xpert cDNA Synthesis Supermix (GRiSP, Porto, Portugal) according to the manufacturer's instructions. The expression of the *EGFP* gene was conducted through quantitative Real Time-PCR (qRT-PCR) using PowerTrack SYBR Green Master Mix in a CFX96 Real-Time PCR System (Bio-Rad Laboratories). qRT-PCR conditions were as follows: 95°C for 3 minutes; 40 cycles at 95°C for 10 seconds and at 60°C for 30 seconds. The human L34 (*RPL34*) transcript was selected as the normalizer, and the relative abundance of the EGFP transcript was determined using the comparative $\Delta\Delta$Ct method. Primer pairs were designed using the open-source Primer3 program version 4.1.0 (https://primer3.ut.ee/) to generate an amplicon of 135 (*EGFP*), and 166 (*RPL34)* bp, and to have a melting temperature of approximately 60°C. The sequences of the primers are provided in the Table in paragraph 3.8.2.

3.8.2. Gene expression studies of EGFP after *in vivo* transfection in zebrafish lymphoma xenograft model

Zebrafish embryos, previously injected with approximately 2,500 BJAB cells, were administered 4.6 nL of NPs (equivalent to approximately 0.8 ng of encapsulated pEGFP) in the duct of Cuvier. At 24 hpi, zebrafish embryos were euthanized with 0.02% tricaine. Total RNA was extracted from experimental groups of 30 embryos with TRIzol® reagent (Life Technologies). Subsequently, 1 µg of RNA was reverse transcribed using Xpert cDNA Synthesis Supermix (GRiSP) according to the manufacturer's instructions. The expression of the *EGFP* gene was conducted through qRT-PCR using PowerTrack SYBR Green Master Mix in a CFX96 Real-Time PCR System (Bio-Rad Laboratories). qRT-PCR conditions were as follows: 95°C for 3 minutes; 40 cycles at 95°C for 10 seconds and at 60°C for 30 seconds. Zebrafish beta-actin (*β-actin*) was selected as the normalizer, and the relative abundance of the EGFP transcript was determined using the comparative ΔΔCt method. The data are expressed as a fold change ratio between samples treated solely with NPs and samples treated with NPs and BJAB cells. Primer pairs were designed using the open-source Primer3 program version 4.1.0 (https://primer3.ut.ee/) to generate an amplicon of 135 (*EGFP*), and 300 (*β-actin*) bp, and to have a melting temperature of about 60°C. Primers' sequences are listed in the following table.

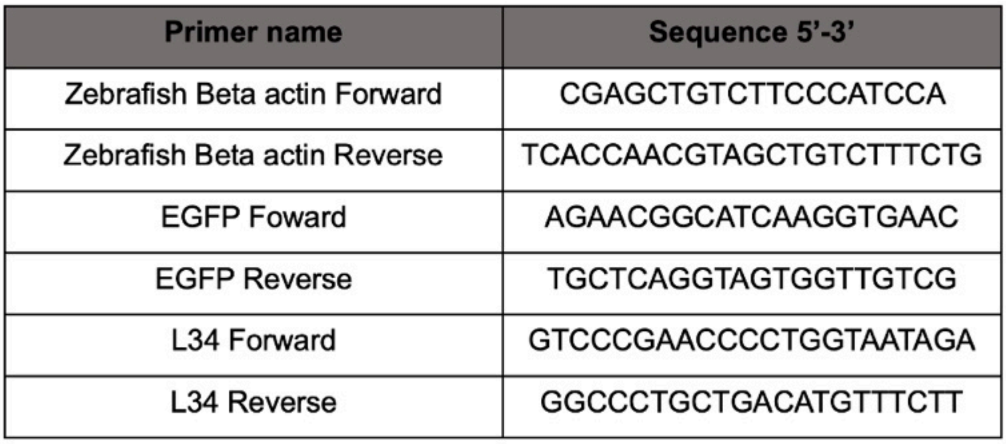

Primer name	Sequence 5'-3'
Zebrafish Beta actin Forward	CGAGCTGTCTTCCCATCCA
Zebrafish Beta actin Reverse	TCACCAACGTAGCTGTCTTTCTG
EGFP Foward	AGAACGGCATCAAGGTGAAC
EGFP Reverse	TGCTCAGGTAGTGGTTGTCG
L34 Forward	GTCCCGAACCCCTGGTAATAGA
L34 Reverse	GGCCCTGCTGACATGTTTCTT

3.9. Calcein retention assay

BJAB (250,000 cells) were labeled with Calcein-AM (Thermo Fisher Scientific) according to the manufacturer's instructions. After 2 washes in 500 µL of PBS, cells were incubated with Rituximab (final concentration 5 ng/µL) or antiCD20 (final concentration 10 ng/µL) at 37°C for 30 minutes in PBS added with 2% BSA, 0.7 mM $CaCl_2$ and 0.7 mM $MgCl_2$ under shacking (750 rpm). Then, normal human serum diluted 1:4 (v/v) in PBS added with 2% BSA, 0.7 mM $CaCl_2$ and 0.7 mM $MgCl_2$ was added to cells and incubated for 1 hour under shacking (750 rpm). Samples were evaluated by flow cytometric analysis performed on an Attune® NxT Acoustic Focusing flow cytometer (Thermo Fisher Scientific) and the cell lysis was calculated with the following formula:

$$\text{Lysis (\%)} = 100- \frac{number\ of\ Calcein\ positive\ treated\ cells}{number\ of\ Calcein\ positive\ untreated\ cells} \times 100$$

3.10. *In vivo* experiments on mice

All the experimental procedures involving animals were done in compliance with the guidelines of the European and Italian laws and were approved by the Italian Ministry of Health as well as by the Administration of the University Animal House (Prot. 42/2012).

3.10.1. Lymphoma xenograft model

A localized BL model was developed based on a previous work published by our laboratory [83] injecting $2x10^6$ BJAB cells in PBS (final volume 100 µL) subcutaneously in the flank of SCID mice (C.B-17/IcrHan®Hsd-Prkdc SCID). A visible tumor mass developed in the animals within a period of 20-25 days. The volume of the tumor mass was subsequently measured using a caliper every two/three days and quantified as follows:

$$Volume = D \times d^2 \times \frac{\pi}{6}$$

where "D" and "d" are the longer and the shorter diameters of the tumor mass, respectively.

3.10.2. Biodistribution studies of nanoparticles

Biodistribution studies were performed in tumor-bearing mice when the tumor mass reached the volume of 250-300 mm^3. Mice were anesthetized, and their abdomen was epilated to avoid the possible scattering owed by the fur; mice were arranged supine in the chamber of the IVIS Lumina (PerkinElmer, Milan, Italy) machine. The parameters of the device, such as exposition, focus, and resolution were set. Then, mice were brought out of the instrument and intraperitoneally injected with 100 µL of Cy5.5-loaded NPs. Mice were analyzed immediately after injection and after 24, 48, or 72 hours. At the end of the analysis, mice were sacrificed, organs explanted and analyzed by IVIS. After that, organs were embedded in the Killik compound (Bio Optica, Milan, Italy) and stored at -80° C.

3.10.3. Evaluation of the therapeutical efficacy of nanoparticles

The evaluation of the NPs therapeutical efficacy was performed in tumor-bearing mice when the tumor mass reached the volume of 250-300 mm^3. Mice were administered a volume corresponding to approximately 3 µg of encapsulated pAntiCD20 in targeted or untargeted NPs in PBS (final volume 100 µL) via intraperitoneal injection three times per week for a total of eight times. Every two days, the volume of the tumor mass was measured by a caliper, and when it reached 10% of the mouse weight, mice were sacrificed. Then, organs were explanted, embedded in the Killik compound (Bio Optica, Milan, Italy), and stored at -80° C.

3.11. Statistical analysis

Measures of the mean, standard deviation (SD), standard error of the mean (SEM), biological replicates, and statistical analyses are indicated in each figure legend. The data were analyzed using GraphPad (San Diego, CA) Prism version 9 by one-way ANOVA with Dunnett multiple-comparison test for the comparison of multiple columns, t-tests for the comparison of two columns, and Log-rank test. A p-value < 0.05 was considered statistically significant and shown in the figures.

4. Results and discussion

4.1. Design and characterization of PLGA-PVA nanoplatform

As previously discussed in the introduction to this thesis, recent literature indicates that NPs can be designed to increase specificity for a target cell type, thereby reducing off-target effects and subsequent toxicity. In alignment with the project rationale, core-shell biodegradable polymeric NPs in PLGA and PVA were produced. These included NPs that were not targeted (untargeted NPs, or NP) and those that were targeted (targeted NPs, or tNP) which were conjugated with the targeting mechanism. The production of this targeting mechanism will be discussed in the following paragraph. To develop this project, a range of NPs was manufactured, incorporating varying payloads.

4.1.1. Production and characterization of the targeting mechanism

The antiCD19 targeting mechanism involved a scFv linked to the human Fc fragment of an IgG1 (scFv-Fc) as a recombinant protein. In detail, this structure comprised a scFv, which is a fusion protein of the variable regions VH and VL of immunoglobulins connected by a short linker peptide (Figure 4.1A). The scFv is encoded in frame with the Fc region, specifically the Hinge-CH_2-CH_3 domains of an antibody. The scFv design was based on the VH and VL regions of MOR208 (Patent n°:US 2014/0227277 A1), also known as Tafasitamab. Tafasitamab is an Fc-modified, humanized, antiCD19 antibody that is currently being investigated in combination with the immunomodulatory drug lenalidomide in an open-label, single-arm, phase II study involving patients with relapsed or refractory DLBCL [166]. The published amino acid sequences were optimized for production in CHO cells and subsequently cloned in frame with the Hinge-CH_2-CH_3 domains of human IgG1 in the eukaryotic expression vector pcDNA3.1/Hygro+. CHO cells were transfected and screened to obtain a high-producing population of antiCD19 in the cell supernatant. The protein was purified from the cell-conditioned medium using affinity chromatography, exploiting the binding between the Fc region and protein “A”. The molecular weight and quality of the produced and purified protein were assessed by SDS-Page stained with Coomassie Blue and Western Blot analysis. As illustrated in Figure 4.1B, the SDS-Page results demonstrated that the purified antiCD19 in its monomeric form comprising the variable domains and the Fc fragment, exhibited three predominant bands under denaturing conditions. The first bands, with an apparent molecular weight of 60 kDa, corresponded to the intact scFv-Fc molecule. The lower bands, with an apparent molecular weight of approximately 50-45 kDa, represented a degraded form of the scFv-Fc molecule. The SDS-Page results indicated that the quantity of non-degraded scFv-Fc was greater than that of the degraded form. These observations were confirmed by Western Blot analysis of the purified scFv-Fc using an alkaline phosphatase-conjugated anti-Human IgG antibody (Figure 4.1C). In non-reducing conditions, an approximately 110 kDa band represented the intact scFv-Fc, while higher and lower bands indicated aggregates and degraded protein, respectively.

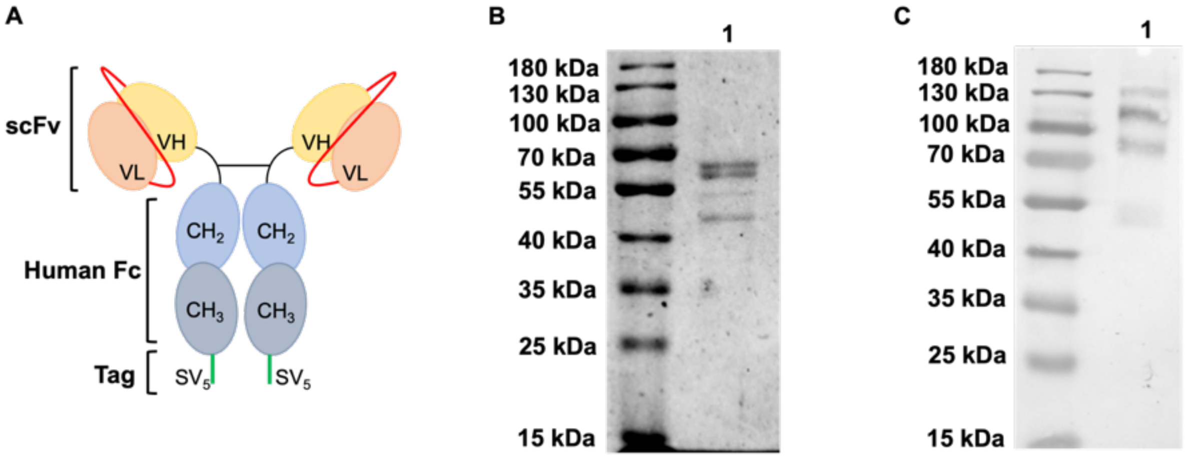

Figure 4.1. AntiCD19 targeting mechanism. (A). Schematic representation of the targeting mechanism comprising a scFv (VH, yellow, and VL, orange) linked through a hinge to the human Fc (CH_2-CH_3, blue), which is fused with an SV_5 tag (green). (B) SDS-Page stained with Comassie Blue conducted in reducing conditions of 300 ng of the antiCD19 (Lane 1) which show the correct molecular weight of ~60 kDa. (C) Western Blot conducted in non-reducing conditions of 300 ng of the antiCD19 (Lane 1) which show the correct molecular weight of ~110 kDa.

The purified antiCD19 was evaluated for its binding to the CD19 antigen. To this end, antiCD19 was incubated with a variety of cell lines. The relevant $CD19^+$ cell models included BJAB (a BL cell line) and NALM-6 (a B-ALL cell line), while the relevant $CD19^-$ cell models were JURKAT (a T-ALL cell line) and RPMI-8226 (a plasmacytoma cell line). The antigen-targeting mechanism interaction was evaluated through the use of a FITC-conjugated anti-Human IgG antibody (excitation/emission 495/519 nm) as the secondary antibody in flow cytometric analysis (Figure 4.2) and fluorescence microscopy (Figure 4.3).

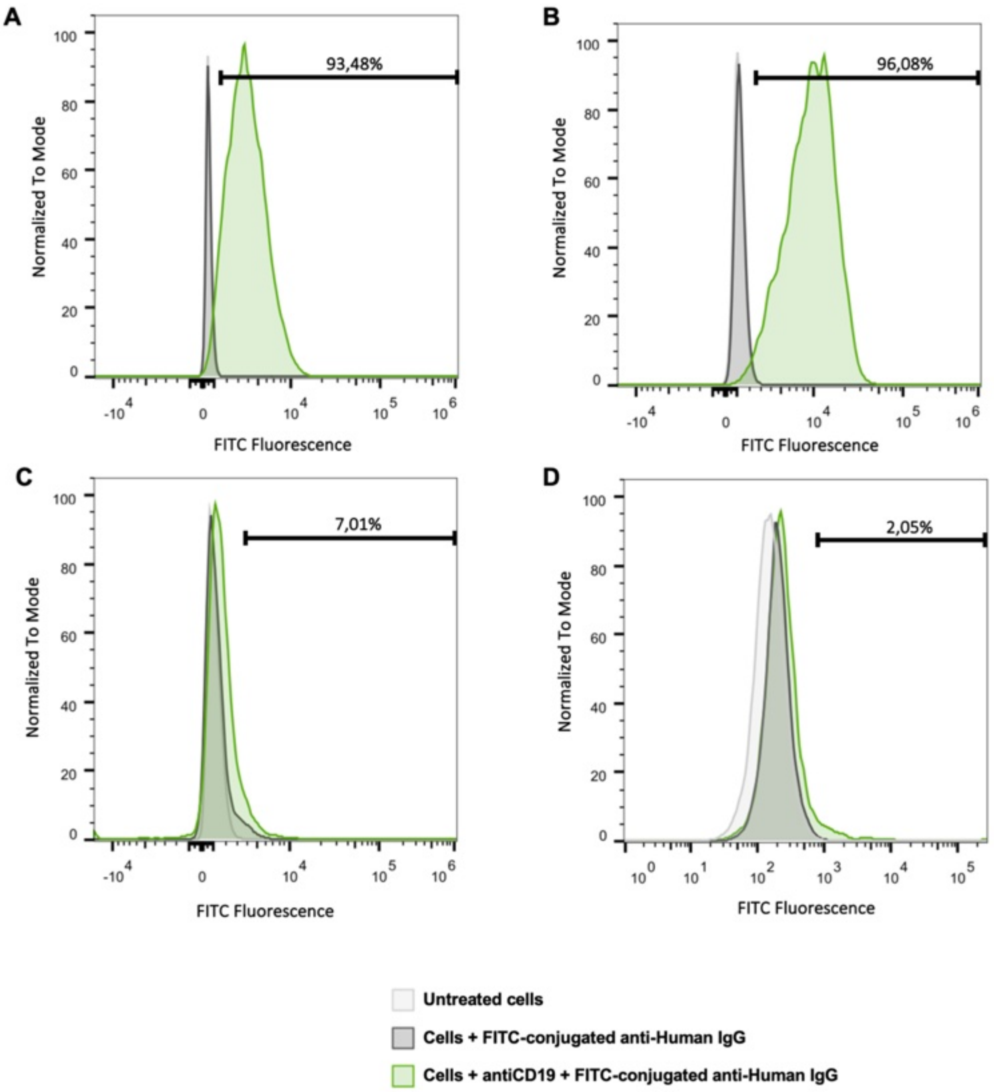

Figure 4.2. Binding of the antiCD19 targeting mechanism to cells by flow cytometry. BJAB (A), NALM-6 (B), JURKAT (C) and RPMI-8226 (D) were incubated with antiCD19 and FITC-conjugated anti-Human IgG antibody (green peaks) or FITC-conjugated anti-Human IgG antibody alone (grey peaks) and analyzed by flow cytometry. Untreated cells (light grey peaks) and cells + FITC-conjugated anti-Human IgG antibody act as negative controls. Data are expressed as % of CD19$^+$ cells.

Flow cytometric analysis revealed that the percentage of cells bound by the antiCD19 exceeded 90%, with specific values of 93.48% for BJAB cells (Figure 4.2A) and 96.08% for NALM-6 cells (Figure 4.2B). The peak of the FITC fluorescence signal, expressed as Mean Fluorescence Intensity (MFI), exhibited a shift in cells incubated with antiCD19 and the secondary antibody in comparison to untreated cells or cells incubated with only the secondary antibody. This shift was not observed in JURKAT cells (Figure 4.2C) and RPMI-8226 cells (Figure 4.2D), where the three peaks overlap. These findings corroborate the binding specificity of the targeting mechanism only in CD19$^+$ cells, which was further substantiated by fluorescence microscopy analysis on BJAB and NALM-6 cells.

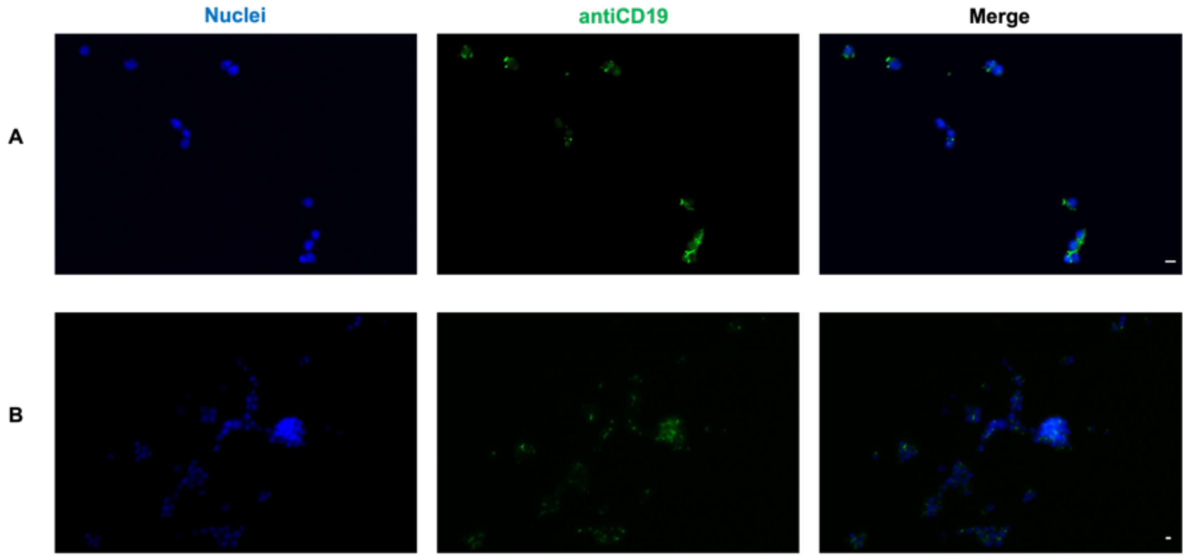

Figure 4.3. Binding of the antiCD19 targeting mechanism to CD19-expressing cells by fluorescence microscopy. BJAB (A) and NALM-6 (B) cells were incubated with antiCD19 and FITC-conjugated anti-Human IgG antibody (green fluorescence). Nuclei were stained with DAPI. Magnification 400X (BJAB), 200X (NALM-6). Scale bar 10 μm.

In BJAB cells (Figure 4.3A) and NALM-6 cells (Figure 4.3B), the green fluorescence signal is prominent on all cell surfaces, indicating that CD19 is an optimal target and antiCD19 is an ideal candidate as a targeting mechanism.

4.1.2. Developing the structure of the nanoplatform

The objective of the strategy delineated in the aim is to guarantee a specific therapeutic effect while circumventing off-target effects. As previously stated in the introduction, recent literature indicates that NPs can be designed to enhance specificity for target tissues, thereby reducing associated toxicity. In light of this rationale, biodegradable polymers, such as PLGA and PVA, were identified as optimal materials for the production of NPs, given their capacity to disaggregate into biocompatible molecules that can be metabolically cleared following administration.

PLGA-PVA NPs were synthesized in our laboratory using a standardized double emulsion solvent evaporation method as described by Vasir and Labhasetwar [161] with minor modifications. The methodology was found to be highly reproducible, yielding approximately $2x10^{12}$ NPs/mL by NTA analysis. In view of the promising results regarding the selectivity of antiCD19 in binding exclusively to $CD19^+$ cells, PLGA-PVA

NPs were subjected to a covalent coating process with antiCD19, thereby establishing a targeting mechanism.

The initial phase of this project was primarily focused on the development and characterization of an optimal nanoplatform for selective delivery. Two types of NPs were produced: untargeted (NP0) and targeted (tNP0). The structures are illustrated in Figure 4.4. Both preparations consisted of an aqueous inner core (TE buffer for these formulations) and an outer shell of PLGA and PVA. In tNP0, the shell was covalently coated with antiCD19 as a targeting mechanism. Specifically, antiCD19 (starting amount 300 µg) was covalently linked to PVA through the EDC/sulfo-NHS crosslinking protocol. The starting amount of antiCD19 was determined through preliminary experiments to achieve an optimal interaction with CD19$^+$ target cells.

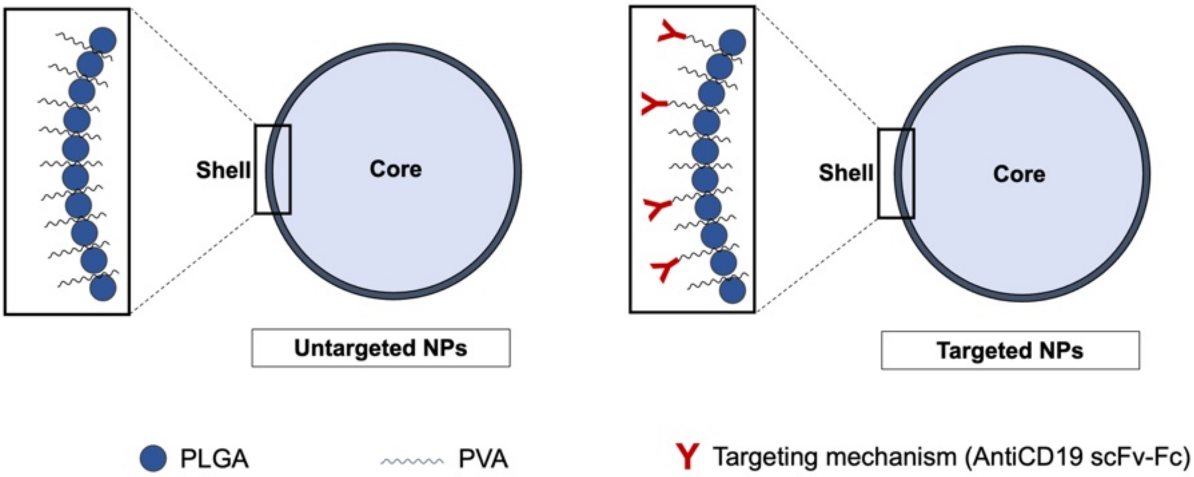

Figure 4.4. Structure of NPs. Schematic representation of untargeted NPs (NP0, left) and antiCD19 targeted NPs (tNP0, right). NP0 are composed by an aqueous inner core (light blue) and a polymeric shell in PLGA (blue sphere) and PVA (black wavy line). In tNP0 the polymeric shell is composed of PLGA and PVA which is covalently linked to the antiCD19 targeting system (red).

DLS analysis of NPs revealed their physicochemical parameters, including size, polydispersity index (PDI), and charge. These findings are summarized in Figure 4.5. The NPs exhibited an average diameter of less than 300 nm (280 ± 2.04 nm for NP0 and 236 ± 4.48 nm for tNP0), with uniform distribution indicated by low PDI values (0.17 ± 0.01 for NP0 and 0.09 ± 0.01 for tNP0). Both NP0 and tNP0 exhibited a negative surface charge with values of -14 ± 0.50 mV and -15 ± 0.76 mV, respectively. Specifically, the negative charge, expressed as zeta potential, minimizes undesired interactions with the MPS and is associated with lower toxicity compared to positively charged NPs. As evidenced in the literature, cationic NPs demonstrate enhanced cellular uptake [167-169] due to favorable electrostatic interactions. However, this phenomenon often coincides with elevated toxicity and a lack of specificity. The diameter of the NPs is of great consequence concerning their clearance, circulation time, and internalization mechanisms. It has been demonstrated that larger NPs exhibit a reduced internalization rate [170, 171] and tend to accumulate primarily in the liver [106]. The PDI is a pivotal parameter that describes the heterogeneity of particle size distribution within a solution. The PDI values range from 0 to 1, with values approaching 0 indicating monodisperse particles and values approaching 1 indicating polydisperse particles. The decrease in size and PDI values of tNP0 compared to NP0 (as well as other formulations described in the next paragraphs) can be attributed to a small, intrinsic variability in the NPs production method, where these variations are consistently observed.

Name	Structure	Coating agent	Encapsulated agent	Average diameter (nm)	Polydispersity index (PDI)	Zeta potential (mV)
NP0		none	none	280 ± 2.04	0.17 ± 0.01	-14.2 ± 0.50
tNP0	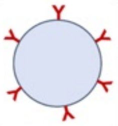	AntiCD19 (~10.5 μg/mL)		236 ± 4.48	0.09 ± 0.01	-15.0 ± 0.76

Figure 4.5. Physicochemical characterization of NPs. Summary of the composition and features of NP0 and tNP0 obtained by DLS.

The spherical shape of NPs was verified by SEM imaging (Figure 4.6) which was conducted at the Centro Interdipartimentale di Microscopia Avanzata “Carlo e Dirce Callerio” (CIMA) as a service by the University of Trieste. The data obtained from the DLS analysis corroborated the results of the size measurements, indicating that the conjugation of antiCD19 on the surface of the NPs did not exert a considerable influence on their physicochemical but also morphological characteristics. The stability of the nanoplatforms was demonstrated by comparable results obtained by DLS and SEM for NPs stored at 4°C for one year, which indicated that the nanoplatforms remained stable over time.

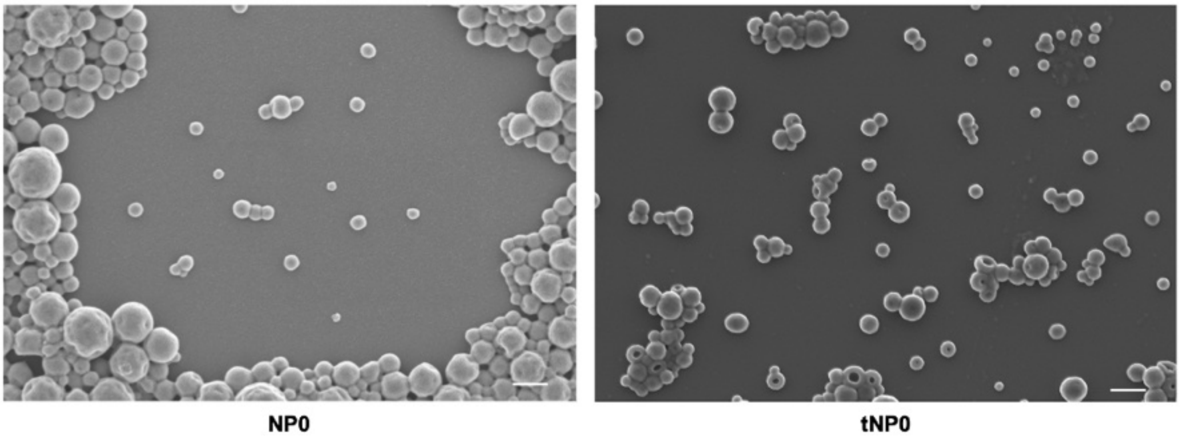

Figure 4.6. Morphological characterization of NPs. SEM images of NP0 and tNP0 (scale bar 300 nm).

The presence of the targeting mechanism in tNP0 was confirmed by ELISA and Western Blot. An ELISA assay (Figure 4.7A) was established to ascertain the presence of antiCD19 on the surface of NPs. In summary, an anti-Human IgG antibody was coated on the plate wells, and then increasing amounts of NP0 and tNP0 were incubated. Their binding was revealed through an alkaline phosphatase-conjugated anti-Human IgG antibody and PNPP as substrate. The OD was read at 405 nm.

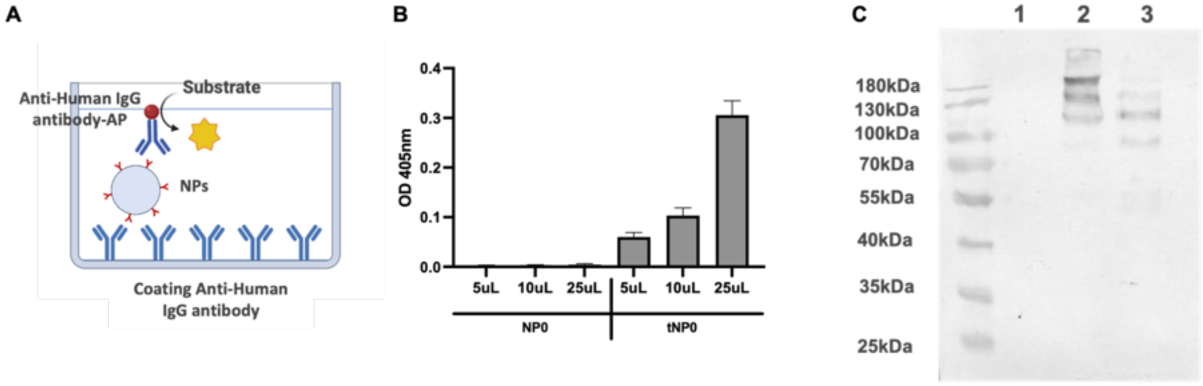

Figure 4.7. Evaluation of the antiCD19 targeting mechanism on the surface of NPs. (A) Schematic representation of the ELISA test performed to verify the presence of the antiCD19 on NPs. (B) Results of ELISA test about the comparison between different amount of NP0 (as negative control) and tNP0 incubated with an alkaline phosphatase-conjugated anti-Human IgG antibody to detect the presence of antiCD19. The values are shown as mean ± SD of n=2. (C) Western Blot conducted in non-reducing condition to evaluate the integrity of the antiCD19. NP0 (Lane 1) is the negative control and tNP0 (Lane 2) and 300 ng of purified antiCD19 (Lane 3) show the expected molecular weight (~110 kDa).

The anti-Human IgG antibody demonstrated a selective interaction with tNP0, thereby confirming the presence of antiCD19 on the external shell of these NPs (Figure 4.7B). Subsequently, the absence of a signal from NP0 validated the specificity of the test.

These data were corroborated by Western Blot analysis (Figure 4.7C) where the presence of antiCD19 was revealed through the same antibody employed in the ELISA assay. This approach allowed for the evaluation of both the integrity of antiCD19 and the efficiency of the coupling binding. As a result, the synthesis of NPs and the conjugation process did not affect the structure of antiCD19, allowing the visualization of the targeting mechanism covalently linked to polymers in tNP0 with the expected molecular weight of 110 kDa added to PVA (30-70 kDa). In fact, bands at higher molecular weight were detected in comparison to the purified antiCD19. Furthermore, a Western Blot under reducing conditions was employed to assess the quantity of antiCD19 attached to the surface of NPs. Specifically, the quantity of antiCD19 present on tNP0 was calculated by exploiting a calibration curve with known concentrations of purified antiCD19. The calculation was based exclusively on the bands that corresponded to the intact scFv-Fc. The analysis revealed that approximately 7% (equivalent to approximately 21 μg total in 2 mL of tNPs) of the initial amount of antiCD19 utilized in the preparation was present on the surface of tNP0. The concentration of NPs obtained by NTA was utilized to calculate the number of molecules present on a single tNP0, which was determined to be approximately 40. Furthermore, it was assumed that the orientation of the antiCD19 and the accessibility of the variable regions for target binding were comparable to those previously demonstrated by our laboratory for scFv-Fc constructs with a similar design [82].

4.1.3. *In vitro* biocompatibility of nanoparticles

In order to assess the potential toxicity of NPs, each formulation was initially tested *in vitro*. In this study, BJAB and JURKAT cells were selected as relevant $CD19^+$ and $CD19^-$ cell models, respectively. The interaction between cells and NPs did not result in cell death after 24 hours of incubation. Instead, it was observed that the mitochondrial activity of cells treated with NPs was increased in both cell lines in comparison to the PBS-treated cells, as determined by the MTT assay (Figure 4.8A). As previously stated, *in vivo* PLGA undergoes degradation by hydrolysis, forming the original monomers (i.e., lactic acid and glycolic acid), which are readily processed via metabolic pathways such as the Krebs cycle. The results confirmed the cytocompatibility of these biodegradable and biocompatible NPs, corroborating prior data in the literature [172, 173].

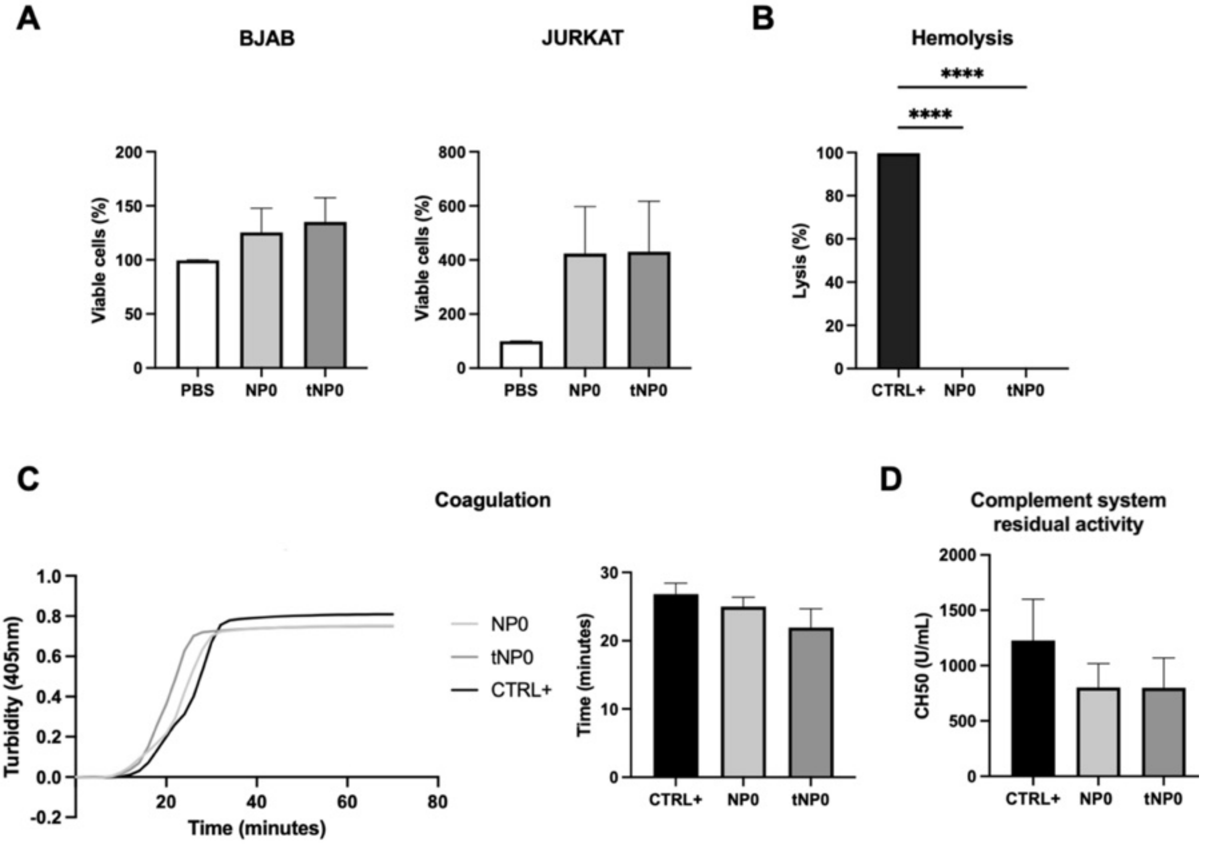

Figure 4.8. *In vitro* tests for safety examination of NPs. (A) MTT cytotoxicity analysis of BJAB (left) and JURKAT (right) cell lines incubated with NP0 and tNP0 for 24 hours. Data are presented as % of mitochondrial activity compared to cells treated with PBS and reported as mean ± SD of n=3. (B) *In vitro* analysis of the direct hemolysis. Data are presented as % of lysis and compared to erythrocytes treated with H_2O ($CTRL^+$ as positive control) and reported as mean ± SD of n=3. Statistics was calculated with One-way ANOVA multiple comparison test. **** = $P \leq 0.0001$. (C) *In vitro* turbidity curve trend of NP0 and tNP0 in activated plasma during time, compared with to a not-treated activated plasma ($CTRL^+$ as positive control) (left) and half coagulation time expressed as NPs-treated-activated plasma turbidity compared to a not-treated activated one ($CTRL^+$ as positive control), reported as mean ± SD of n=3 (right). Statistics was calculated with One-way ANOVA multiple comparison test. (D) Complement system residual activity expressed as number of hemolytic units per mL (CH50) of NPs-treated serum compared to a no treated one ($CTRL^+$ as positive control), reported as mean ± SD of n=2. Statistics was calculated with One-way ANOVA multiple comparison test.

The capacity of NPs to lyse red blood cells was also evaluated by assessing the release of hemoglobin as a product of direct hemolysis. No mechanical disruption of erythrocytes was observed (Figure 4.8B). A turbidity assay was conducted to establish if NPs interfere with the coagulation process (Figure 4.8C); NPs were incubated with normal human citrate-anticoagulated plasma, and a solution containing Ca^{2+} was added to trigger the coagulation. The turbidity resulting from the activation of the coagulation process was analyzed over time, demonstrating that the coagulation exhibited a similar trend in the presence and absence of NPs. In fact, the kinetic profile of the reaction (Figure 4.8C, left) exhibited a distinctive trend: the curve grows at a relatively consistent rate in accordance with the coagulation speed until it reaches a plateau. From these curves, the half-coagulation time was extrapolated, and the data demonstrated a non-significant difference between NPs-treated plasma and the positive control (CTRL$^+$) that had not been treated with NPs (Figure 4.8C, right).

As previously stated in the introduction, NPs injected into the bloodstream can interact with serum proteins forming a coating layer called protein corona. Among these proteins, complement system components can be adsorbed on the surface of NPs, resulting in a slight settling of them on the external shell and a subsequent reduction in the number of complement system molecules capable of activating the cascade. Accordingly, the result of this potential deposition was investigated in a CH50 hemolytic assay (Figure 4.8D), which expressed the residual activity of the classical pathway. This assay tested the capability of serum complement proteins to lyse red blood cells through the activation of the classical pathway, specifically. To this end, normal human serum was incubated with both NPs and PBS (representing the CTRL$^+$, which served as the control). Consequently, the percentage of lysis caused by each sample and then the amount of serum required to achieve 50% lysis of red blood cells in our test were calculated. The CH50, representing the number of hemolytic units required to achieve 50% lysis of red blood cells, was subsequently calculated based on the obtained results. A reduction in CH50 values relative to the reference serum indicates a decrease in the number of hemolytic units, which suggests that the complement system has been interfered with. As demonstrated, the number of hemolytic units per milliliter, in serum treated with NP0 and tNP0, was comparable across all conditions, indicating that these NPs did not significantly impair complement system function through the classical pathway. These findings are consistent with those of other PLGA-PVA NPs currently under development in our laboratory.

To further investigate the impact of these NPs on physiological processes, a human whole blood with endothelial cells model was developed in collaboration with Prof. Per Nilsson (Linnèuniversitet, Kalmar, Sweden) [162] with the objective of mimicking the response in a blood vessel. To this end, lepirudin-anticoagulated human blood from 6 distinct healthy donors was incubated with HLMVECs with or without NPs, for up to 4 hours (Figure 4.9). Lepirudin is a highly specific thrombin inhibitor that does not show interference with the complement system, thereby allowing for the study of this system [174].

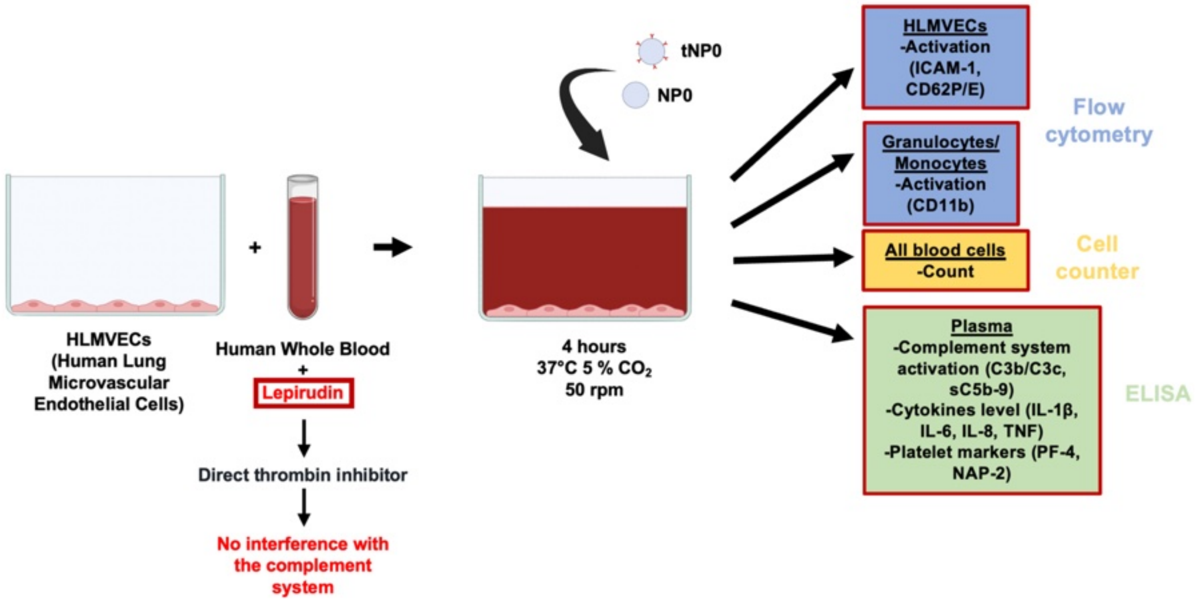

Figure 4.9. Schematic representation of the human whole blood-endothelial cell model. HLMVECs were incubated with lepirudin-anticoagulated human whole blood from 6 different and with or without NPs, for up to 4 hours at 37°C, 5% CO_2 at 50 rpm. Flow cytometry analysis allow to evaluate HLMVECs and blood cells (specifically monocytes and granulocytes) activation by evaluating ICAM-1, CD62P/E, and CD11b. Variations in cell blood count were analyzed by a cell counter. ELISA assay on plasma allowed to evaluate complement system activation (C3b/C3c and sC5b-9), the cytokine release (IL-1β, IL-6, IL-8, and TNF) and platelets activation markers (PF-4, NAP-2).

To evaluate if NPs affected complement system activation, the complement C3-activation markers C3b/C3c, and the soluble terminal complement sC5b-9 complex were quantified by ELISA (Figure 4.10A). The results demonstrated that, in comparison to whole blood treated with PBS, NPs significantly enhanced complement system activation, independently from the presence of the targeting mechanism. In fact, the use of an antibody that recognizes neoepitopes in activated C3 fragments (i.e., C3b, iC3b, and C3c) [175, 176] confirmed the complement system activation. Furthermore, it is noteworthy that C3 acts as a convergence point for the classical, alternative, and lectin pathways, which precludes the ability to discern whether all three pathways were activated. Moreover, the significantly elevated levels of sC5b-9 in NP-treated samples indicate not only the activation of C3 but also the complete activation of the complement cascade, thereby confirming the activation of the system from its initial stage to the terminal pathway.

Subsequently, the inflammatory response elicited by NPs in HLMVECs-whole blood interactions was investigated through the quantification of cell surface inflammation markers and cytokine release by flow cytometry and ELISA, respectively.

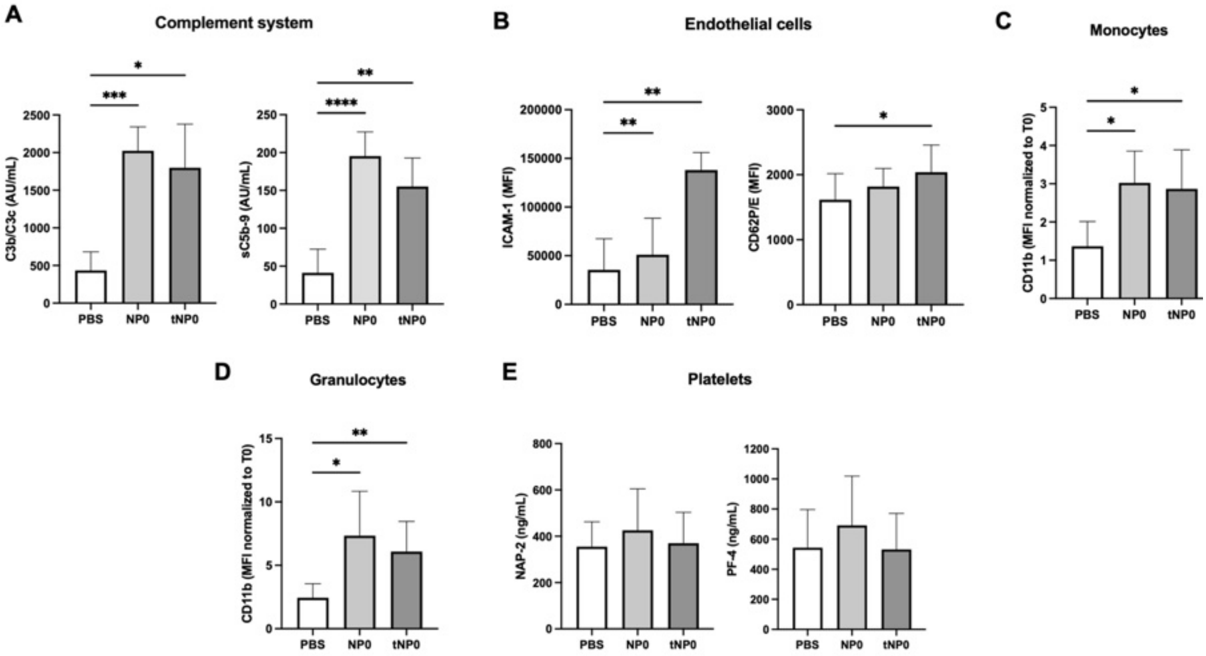

Figure 4.10. Endothelial cells and human blood cells activation. (A) Complement activation by NP0 and tNP0 in human whole blood evaluated by measuring the formation of C3b/C3c (left) and sC5b-9 (right) by ELISA. PBS as negative control. The values are shown as mean ± SD of n=6. (B) HLMVECs endothelial cells activation evaluated by measuring ICAM-1 (A) and CD62P/E (B) expression by flow cytometry. Cell surface activation marker CD11b was measured on monocytes (C) and granulocytes (D) by flow cytometry. (E) Plasma was analyzed by ELISA for soluble markers NAP-1 (E) and PF-4 (F) for platelets activation. Statistical was calculated with One-way ANOVA multiple comparison test. * = P ≤ 0.05; ** = P ≤ 0.01; *** = P ≤ 0.001; **** = P ≤ 0.0001.

As illustrated in Figure 4.10B, the flow cytometry data revealed that following exposure to NPs, HLMVECs and blood cells (monocytes and granulocytes) exhibited activation. This is evidenced by the increase in the MFI signal relative to the labeled antibodies targeting inflammation markers used for the evaluation, in comparison to the PBS treatment. Of particular note is the crucial role played by endothelial cells in regulating the function of blood vessels. Consequently, endothelial dysfunction can result in increased vascular permeability, augmented interactions between leukocytes and endothelial cells, and an inflammatory state [177]. Specifically, the activation of HLMVECs endothelial cells was evaluated by examining the expression of two key adhesion molecules: ICAM-1 (Intracellular Adhesion Molecule 1) and CD62P/E Selectin. These molecules are known to increase upon endothelial cell activation as part of the inflammatory response. HLMVECs exhibited a significantly higher expression of ICAM-1 following exposure to both NP0 and tNP0, as evidenced by the elevated MFI values in comparison to the negative control (PBS). Conversely, a significant enhanced expression of CD62P/E Selectin was observed exclusively in samples treated with tNP0, in contrast to those treated with PBS. However, several factors warrant further consideration with regard to this response. Firstly, it has been demonstrated in the literature that endothelial cell activation may be potentiated directly by local complement system activation in response to stress conditions [178], particularly given the presence of C5a receptors on their cell surfaces [179-181]. Moreover, it has been demonstrated that under static conditions, similarly to this model, endothelial cells are susceptible to nonspecific interactions with NPs [182]. It can be reasonably deduced that the absence of fluid flow may have resulted in the local activation of the complement system, which subsequently activated the endothelial cells. It seems reasonable to posit that this phenomenon would not occur in a fluidics system, where the interaction between cells and NPs would be limited. Both ICAM-1 and CD62P/E are expressed in response to complement activation fragments and several proinflammatory cytokines, including IL-1β and TNF [183]. The values of these cytokines, as well as those of IL-6 and IL-8, were generally low in this test and will be discussed later. Nevertheless, it is not possible to establish from our data whether PLGA-PVA NPs would directly trigger complement system deposition on the endothelial cells. These findings align with those of previous studies, which have demonstrated that direct exposure of endothelial cells to various types of NPs can lead to their activation, characterized by the expression of adhesion molecules, the release of inflammatory markers, and monocyte adhesion [162]. In addition, it is relevant to underline that ICAM-1 and CD62P/E expression on activated cells can be detected within 4 hours after induction [162, 184, 185], as done in our test, suggesting their effective activation.

Monocytes and granulocytes were isolated from the whole blood after the initial 15 minutes of incubation with NPs or PBS, as these cells exhibited a rapid activation process. To account for the considerable inter-donor variability in the response to NPs, the MFI values were normalized to the basal levels observed at T0, which was defined as the time point preceding exposure. The cell surface activation marker CD11b, in both monocytes (Figure 4.10C) and granulocytes (Figure 4.10D) treated with NPs, is more expressed than in samples incubated with PBS. However, these cells exhibited only a marginal activation, as evidenced by the expression of surface adhesion molecules and the absence of inflammatory cytokines that can be produced following their activation, as will be described subsequently. It is established that ICAM-1 and CD62P/E interact with activated granulocytes and monocytes in the circulation, which provides an explanation for the increased expression of CD11b integrin [186-188]; furthermore, the ability of granulocytes to interact with exogenous agents (i.e., NPs), as well as monocytes, could stimulate their activation [189]. C5a receptors are also present in these cell types, establishing a link with the previously detected complement system activation [190].

The role of platelets, cell fragments with an important function in the thrombo-inflammatory response, was examined. Although the coagulation and complement systems are two distinct systems, both represent a defense mechanism against external agents and are interconnected through crosstalk between their components [191]. Consequently, in addition to the previously described clotting test, the impact of NPs on platelet activation in whole blood was also evaluated. Soluble activation markers NAP-2 and PF-4, which are specifically released by activated platelets, were analyzed in plasma isolated from the whole blood after incubation with NPs or PBS for 4 hours (Figure 4.10E). No significant activation was observed, as evidenced by the comparable levels following incubation with both NPs and PBS. This finding corroborates the previous data obtained from the clotting test.

Given the observed activation of endothelial cells, monocytes, and granulocytes, the potential release of IL-1β, IL-6, IL-8, and TNF was then quantified in plasma.

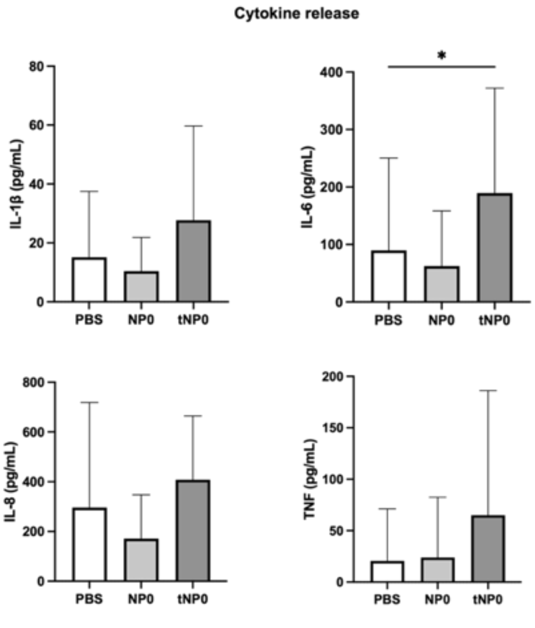

Figure 4.11. Cytokine release. Cytokine release in plasma was analyzed with a 4-plex cytokine Luminex assay for IL-1β (upper left), IL-6 (upper right), IL-8 (lower left) and TNF (lower right). PBS as negative control. The values are shown as mean ± SD of n=6. Statistical was calculated with One-way ANOVA multiple comparison test. * = P ≤ 0.05.

As illustrated in Figure 4.11, despite the activation of the aforementioned cell types, the cytokine release remains comparable to that induced by PBS. Only an IL-6 release is discernible following exposure to tNP0. In contrast to the evaluation of ICAM-1 and CD62P/E, which entailed assessing the increase in expression of an existing protein, this investigation necessitates the production and release of a novel protein. The incubation period of 4 hours appears to be sufficient for this process, as evidenced by the release induced by the positive control (represented by a mixture of Zymosan 100 µg/mL and Lipopolysaccharides 10 ng/mL) in our experiments (data not shown). In fact, PLGA-PVA NPs do not induce cytokine release, in contrast to other types of NPs tested with the same model, where higher amounts of protein were detectable [162].

Moreover, variations in cell blood count were considered (Figure 4.12). The number of red and white blood cells and hemoglobin remained unaltered, confirming the absence of erythrocyte lysis or leukocyte toxicity. However, a slight reduction was observed in platelet numbers in comparison to the negative control (PBS).

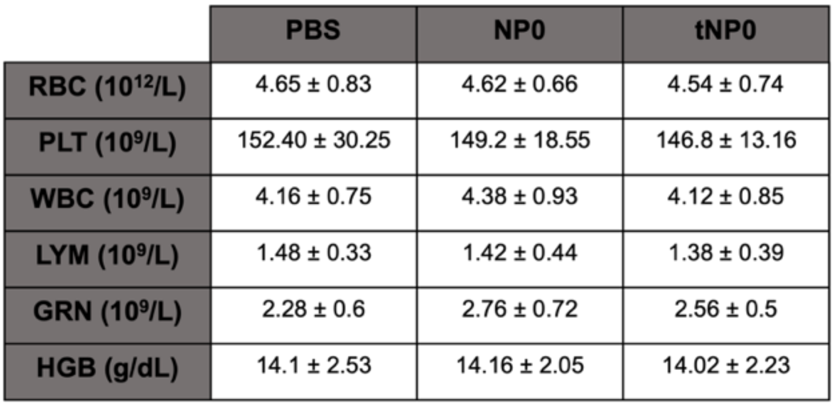

	PBS	NP0	tNP0
RBC (10^{12}/L)	4.65 ± 0.83	4.62 ± 0.66	4.54 ± 0.74
PLT (10^{9}/L)	152.40 ± 30.25	149.2 ± 18.55	146.8 ± 13.16
WBC (10^{9}/L)	4.16 ± 0.75	4.38 ± 0.93	4.12 ± 0.85
LYM (10^{9}/L)	1.48 ± 0.33	1.42 ± 0.44	1.38 ± 0.39
GRN (10^{9}/L)	2.28 ± 0.6	2.76 ± 0.72	2.56 ± 0.5
HGB (g/dL)	14.1 ± 2.53	14.16 ± 2.05	14.02 ± 2.23

Figure 4.12. Blood cells count and parameters variations. Red Blood Cells (RBC), platelets (PLT), White Blood Cells (WBC), Lymphocytes (LYM) and Granulocytes (GRN), hemoglobin (HGB) values in human whole blood treated with NP0, tNP0, or PBS evaluated by cell counter.

4.1.4. Encapsulation efficiency and release studies

Two new NPs formulations were produced, employing the identical protocol utilized for the previous ones. Differently from the preceding formulations, these encapsulated FITC-BSA within the inner core, resulting in the formation of untargeted (NP FITC) and targeted NPs (tNP FITC). These allowed us to establish the encapsulation efficiency of NPs, the rate of payload release, and the interaction between the NPs and target cells.

Name	Structure	Coating agent	Encapsulated agent	Average diameter (nm)	Polydispersity index (PDI)	Zeta potential (mV)
NP FITC	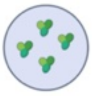	none	FITC-BSA (~2 mg/mL)	252 ± 4.30	0.11 ± 0.03	-15.0 ± 0.36
tNP FITC	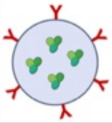	AntiCD19 (~10.5 μg/mL)		275 ± 3.63	0.08 ± 0.01	-14.0 ± 0.10

Figure 4.13. Physicochemical characterization of FITC-BSA-loaded NPs. Summary of the composition and features of NP FITC and tNP FITC obtained by DLS.

The payload did not affect both the antiCD19 coupling efficiency and physicochemical parameters, which are summarized in Figure 4.13. The encapsulation efficiency of FITC-BSA was estimated by an indirect method, whereby the difference between the initial amount of FITC-BSA added during the preparation process and the remaining amount in the aqueous suspension after centrifugation and washing steps was calculated. This remaining amount was defined as the unencapsulated protein (or compound) present in the supernatant. The fluorescent properties of FITC were employed to quantify the fluorescent signal of FITC-BSA at an emission wavelength of 519 nm. The fluorescence signals of the unencapsulated and that of pure FITC-BSA were quantified and expressed as CTCF. The fluorescence values for the unencapsulated were interpolated with those of a standard curve of FITC-BSA, and the amount of FITC-BSA that was not encapsulated in the core of NPs was extrapolated. The amount of FITC-BSA encapsulated in NPs was calculated and found to be approximately 70% for both preparations, thereby supporting the reproducibility of the synthesis process. Furthermore, the uniformity of the two formulations was confirmed by directly quantifying the fluorescent signal expressed as CTCF of both NPs immediately after synthesis, which was defined as T0 (Figure 4.14A). The spontaneous payload release was evaluated over a one-year period at storage conditions of 4°C by quantifying the fluorescence signal of NPs, as previously described. As illustrated in Figure 4.14B, both formulations exhibited a slight loss of FITC-BSA, confirming their stability and enabling their prolonged use.

To further characterize the structure of NPs, release studies were conducted in a variety of buffers and conditions for a maximum period of 1 hour (Figure 4.14C), which represents the incubation time for binding and internalization studies, described in detail in the subsequent paragraph. In storage conditions (PBS at 4°C) the payload release was observed to be low and comparable between the two formulations. At 37°C and pH 7.4 which correspond to physiological conditions, both FITC-BSA-loaded NPs exhibit a burst release with approximately 20% of the payload dispersed in PBS and reaching a plateau. A similar trend was observed in diluted normal human serum, which mimics the presence of all serum proteins. The primary release was observed to be approximately 40% in a simulated cytosol (cytosol mimic buffer), which prompted an assessment of fluorescence stability following cell internalization.

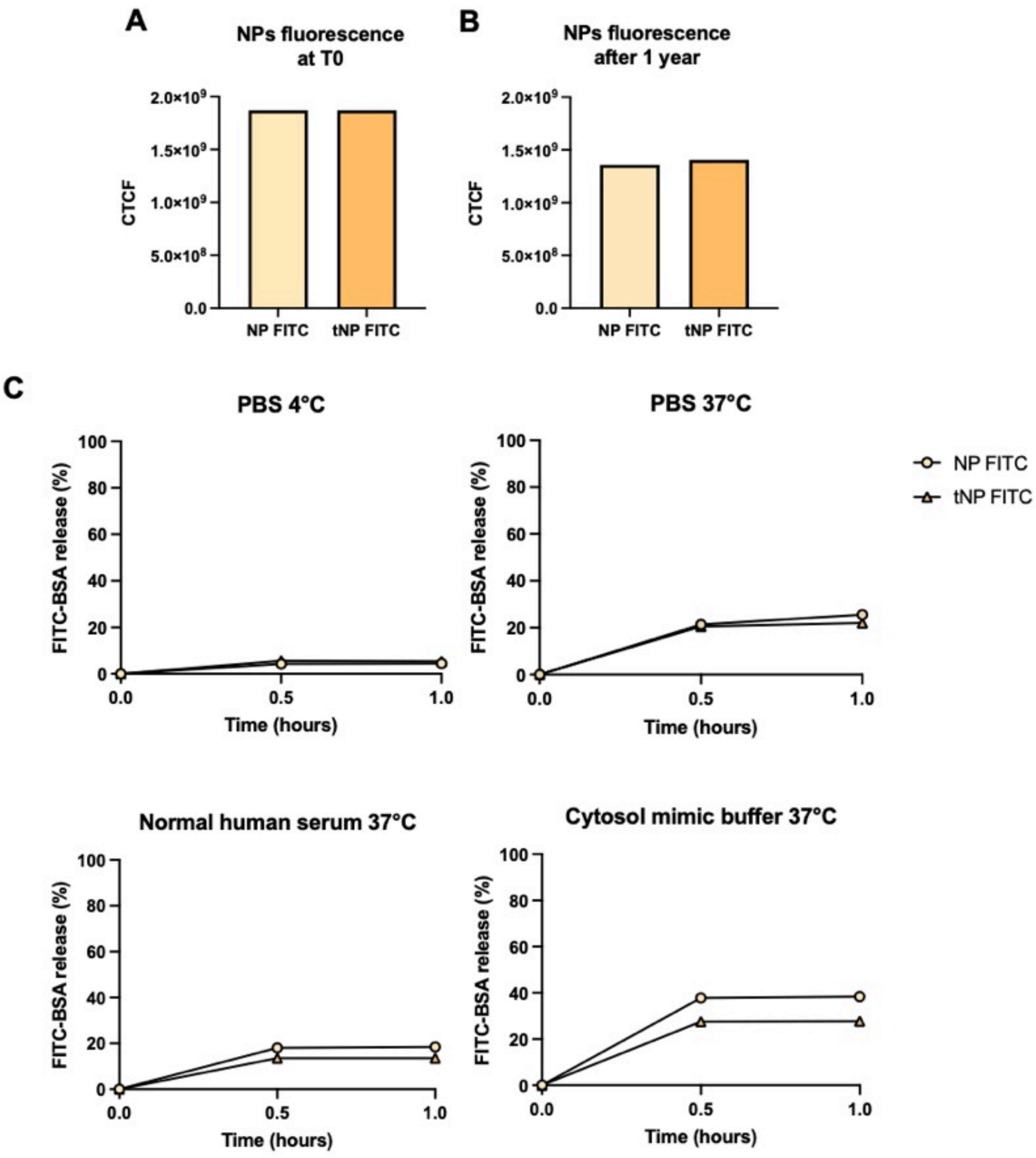

Figure 4.14. Evaluation of FITC-BSA-loaded NPs fluorescent properties. (A) Quantification of fluorescence of NPs loaded with FITC-BSA at T0 (immediately after synthesis). Data are expressed as CTCF. (B) Quantification of fluorescence of FITC-BSA-loaded NPs after 1 year. Data are expressed as CTCF. (C) Release studies of FITC-BSA from NPs in PBS at 4°C, PBS at 37°C, normal human serum at 37°C or cytosol mimic buffer at 37°C for 0.5-1 hour. The values are shown as mean ± SD of n=2.

4.1.5. Targeting tumoral B cells in Burkitt lymphoma

The primary objective of the characterized nanoplatform is to ensure specific interactions with target cells, thereby reducing potential off-target effects resulting from interactions with other cell types. As previously stated, this can be accomplished through the use of targeting mechanisms. Moreover, beyond the initial interaction, NPs must be internalized in order to achieve their intended therapeutic effect. To this end, flow cytometry and fluorescence microscopy techniques were employed to assess the selective interaction of the targeting mechanism with $CD19^+$ target cells, represented by the BL cell line BJAB, both *in vitro* and *in vivo*.

4.1.5.1. *In vitro* binding and internalization studies

The interaction between NPs and cells and the efficacy of the targeting system were investigated through flow cytometry on both BJAB and JURKAT cells that were incubated with NP FITC or tNP FITC for 1 hour at 37°C (Figure 4.15).

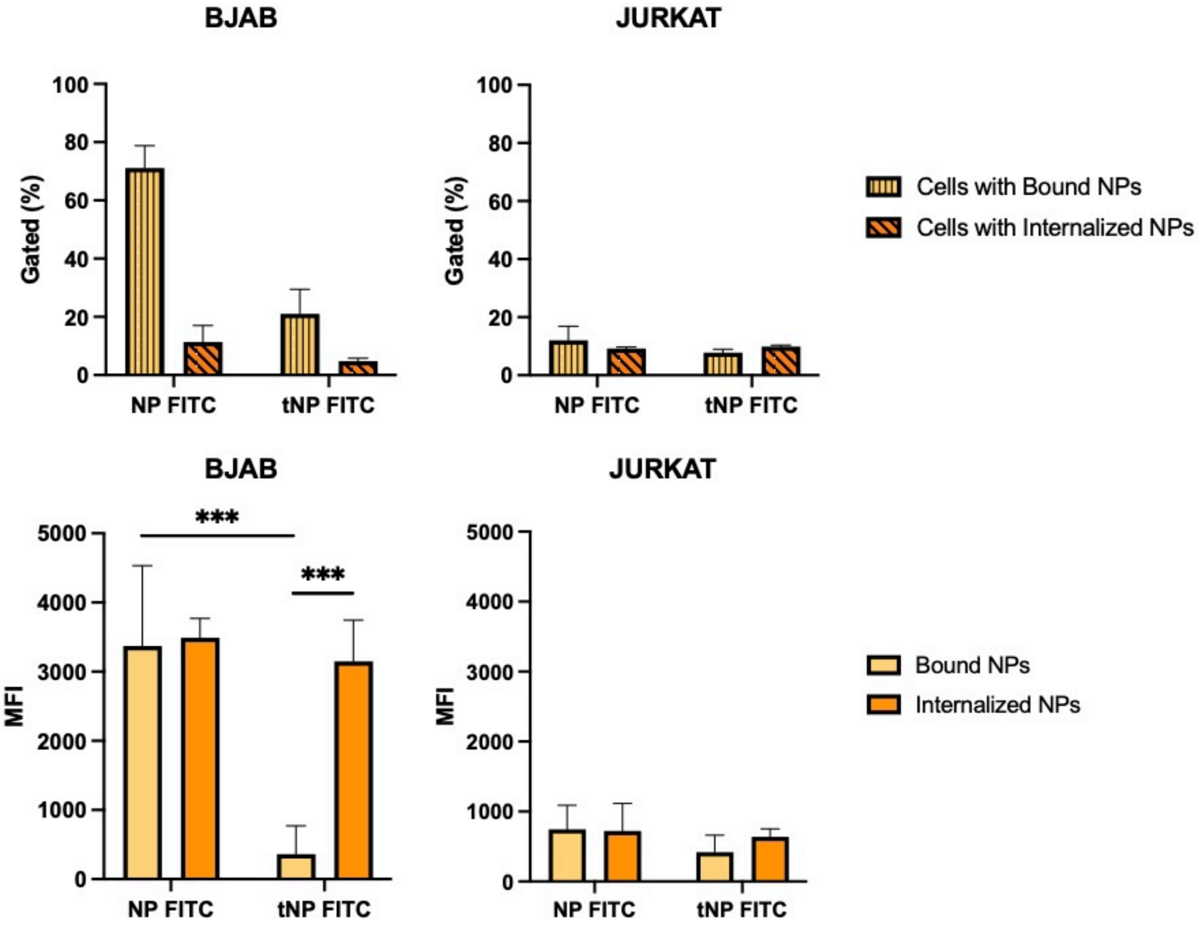

Figure 4.15. *In vitro* effectiveness of the antiCD19 targeting mechanism. Binding and internalization studies of NPs performed for 1 hour on BJAB (left panels) and JURKAT (right panels) cells by flow cytometry. Data are expressed as % of cells interacting with NPs (upper panels) and amount of NPs (lower panels) interacting with cells. The values are shown as mean ± SD of n=3. Statistical was calculated with One-way ANOVA multiple comparison test. *** = P ≤ 0.001.

The percentage of positive events in BJAB cells (Figure 4.15, upper left panel) was analyzed. BJAB cells exhibited greater interaction when incubated with NP FITC. In fact, the percentage of gated cells with bound NP FITC is higher compared to tNP FITC (~70% versus ~20%, respectively). To further investigate this aspect, we focused on the pH-dependent fluorescence properties of FITC-BSA (Figure 4.16). This analysis aimed to ascertain whether FITC-BSA present within internalized NPs retains its fluorescent properties.

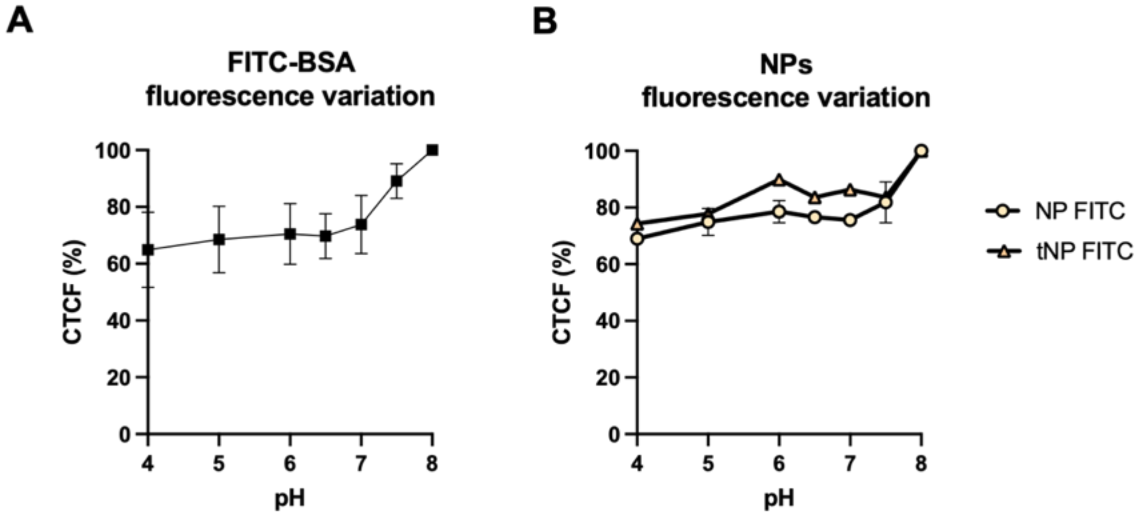

Figure 4.16. Evaluation of pH-dependent FITC-BSA properties. (A) FITC-BSA fluorescence variation at different pH. (B) NP FITC and tNP FITC fluorescence variation at different pH. The values are shown as mean ± SD of n=2.

For this purpose, FITC-BSA was resuspended in a series of buffered solutions with varying pH values (between 4.0 and 8.0), and the fluorescent signal was calculated as previously described. The CTCF of FITC-BSA, expressed as a percentage, demonstrated a higher value at alkaline-neutral pH and a lower value at acidic pH, with a notable decrease of approximately 30% in fluorescence (Figure 4.16A). This demonstrated the pH sensitivity of FITC, and the same trend was observed for NPs encapsulating FITC-BSA (Figure 4.16B). With regard to the process of entry, PLGA NPs are primarily internalized by clathrin-mediated endocytosis [192] with the formation of an endocytic vesicle and progresses to an early endosomal compartment, ultimately maturing into a late endosome [193]. This latter compartment is then fused with a lysosome, where NPs and cargo can be degraded. The surface charge plays a pivotal role in this process, as evidenced by the observation that cationic PLGA NPs are less colocalized with lysosomes compared to anionic ones [194]. Nevertheless, the phenomenon of endosomal escape has been demonstrated to significantly reduce the rate of internalization within this compartment [195]. Furthermore, the CD19 antigen is well documented to be internalized following binding by antibodies [49], which is a fundamental feature in determining the efficacy of many targeted therapeutics. Therefore, the interaction between the antiCD19 on the NPs and the CD19 antigen on the cell surface may potentially enhance the internalization rate. A proportion of NPs undergo endosomal escape, while another part enters the lysosome; these possess an acid pH which results in both FITC-BSA proteolytic degradation [196] and a greater FITC-BSA-loaded NPs fluorescence decrease. This leads to a reduction in the MFI and percentage of positive target cells detected. Conversely, untargeted NPs exhibited reduced internalization, resulting in enhanced fluorescence.

To detect only cells that had internalized NPs, BJAB cells were treated with Pronase, a protease mixture, to differentiate between internalized NPs and those attached to the cell surface. The proteolytic activity of Pronase results in the degradation of surface proteins that are responsible for mediating the attachment of NPs to the cell. This process disrupts both specific (ligand-receptor) and non-specific interactions, resulting in the release of externally bound NPs [197]. NPs that are internalized and protected within the cell remain intact, as the Pronase enzymes are unable to access them. Following treatment, approximately 10% of BJAB cells treated with NP FITC and ~7% of BJAB cells treated with tNP FITC exhibited internalized NPs (Figure 4.15, upper left panel).

In contrast, the MFI was employed to estimate the internalization rate of NPs (Figure 4.15, lower left panel). BJAB cells exhibited a comparable amount of bound and internalized NP FITC (MFI of 3400 versus 3500). On the contrary, the signal associated with tNP FITC interacting with BJAB cells indicated that the majority of NPs were internalized within cells. The MFI values of bound tNP FITC in BJAB cells were significantly lower in comparison to NP FITC (360 versus 3400). In fact, the MFI values of internalized tNP FITC were significantly higher than those of the bound NPs (3150 versus 360). In contrast, in JURKAT cells, no significant differences were observed in the percentage of gated cells with bound NPs for both types of NPs (Figure 4.15, upper right panel). The percentage of cells interacting with NPs was approximately 12% for NP FITC and approximately 7% for tNP FITC. Following treatment with Pronase, this resulted in approximately 9% for both formulations. The relevance of the targeting mechanism was confirmed by analyzing the MFI related to the number of interacting NPs (Figure 4.15, lower right panel). In this instance, the values of the bound or internalized NPs were comparable for both formulations. The MFI for bound NPs is approximately 740 for NP FITC and approximately 420 for tNP FITC while the MFI for internalized NPs is approximately 720 and 640, respectively. These results on CD19$^-$ cells corroborated the preceding hypothesis regarding the pH-dependent fluorescence of FITC-BSA. There was no significant distinction between the untargeted and targeted NPs, indicating that both NPs are not primarily internalized and predominantly remain on the cell surface of JURKAT cells, thereby preserving their fluorescence.

4.1.5.2. Development of Burkitt lymphoma tumor-bearing zebrafish model

The behavior of NP FITC and tNP FITC was investigated in an *in vivo* model through a comparative analysis. Specifically, studies were conducted on zebrafish embryos. Since 2005, when Lee et al. [198] first employed zebrafish as an animal model for xenograft transplantation, the popularity of this model has increased. The choice of zebrafish embryos as a model for *in vivo* studies was influenced by several factors. In fact, the immaturity of the adaptive immune system for up to four to six weeks makes xenografts a viable option. Furthermore, the transparency of embryos allows for the imaging of labeled cells and NPs distribution [199, 200]. In zebrafish, the formation of pigmentation is initiated during the embryonic stage in the retinal epithelium and dorsolaterally in the skin. This process initiates approximately 24 hpf and progresses rapidly [201]. As these pigmented areas are autofluorescent and can influence subsequent steps in the process, the pigmentation was inhibited through the use of PTU, an enzyme that affects the conversion of tyrosine to melanin. Furthermore, prior to hatching, the zebrafish embryo is surrounded by an acellular envelope, the chorion, which was manually removed 24 hpf, ensuring the PTU effect.

A localized BL tumor-bearing zebrafish model was initially established by injecting approximately 2,500 Calcein AM-labeled BJAB cells (which possessed red fluorescence with a maximum excitation/emission of 577/590 nm) into the perivitelline space [202] of wild-type zebrafish embryos at 48 hpf. The model was then visualized by fluorescence microscopy until 24 hpi (Figure 4.17A). As illustrated in Figure 4.17B, BJAB cells, indicated by the red fluorescent signal, remained in close proximity to the injection site, without exhibiting any evidence of spreading into the embryo body. This is a crucial feature as it permitted the establishment of a localized model that closely resembles the clinical characteristics of BL as a solid tumor. It is noteworthy that, although the injected zebrafish were observed until 24 hpi in this model, zebrafish were observed until 48 hpi in our previous models of B-cell malignancies [98]. This enabled us to assess the longevity of the injected cells within the body and the absence of toxicity. As illustrated in Figure 4.17C, by considering two different experimental groups (Group A and Group B), the red fluorescence signal, expressed as CTCF, regarding the amount of cells injected was comparable. This indicated that the animals received the same quantity of cells and that the model was reproducible. Furthermore, the animals did not significantly eliminate the cells because the cell fluorescence signal after 24 hours was comparable to that detected after 0.5 hours.

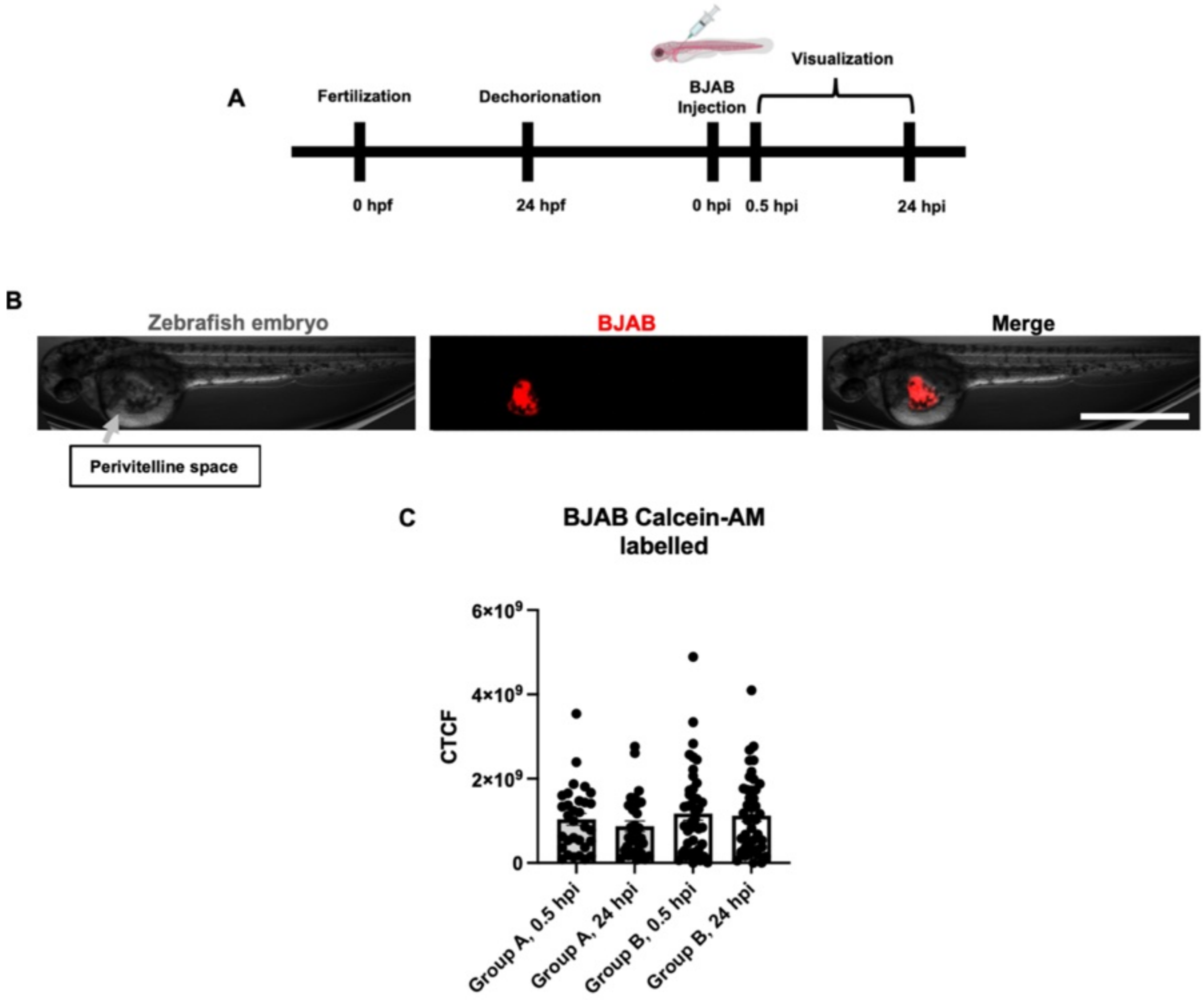

Figure 4.17. Setting of the localized tumor-bearing zebrafish model of Burkitt lymphoma. (A) Timeline of the experimental procedure. (B) ~ 2,500 Calcein AM-labeled BJAB cells (central panel) were injected the perivitelline space (grey arrow) of wild-type zebrafish embryos at 48 hpf, without

spreading into the body. Magnification 40X. Scale bar 1000 µm. (C) Data analysis of the CTCF of the red-fluorescent areas (BJAB cells) in the perivitelline space of zebrafish embryos at 0.5 and 24 hpi. The values are shown as mean ± SEM of n=40. Statistical was calculated with One-way ANOVA multiple comparison test.

4.1.5.2.1. *In vivo* biodistribution studies in Burkitt lymphoma tumor-bearing zebrafish model

The role of the targeting mechanism was also assessed in the localized BL tumor-bearing zebrafish model. Once the model had been established, 4.6 nL of NP FITC or tNP FITC, which is a minimal sufficient amount for visualization in this model, were then injected into the duct of Cuvier which is an embryonic vein structure that collects all venous blood and leads directly to the heart's sinus venosus. It is used to disperse compounds into the bloodstream. The subsequent fluorescence microscopy analysis was conducted for a period of 0.5 and 24 hours. The interaction between BJAB cells in the perivitelline space and NPs injected in the bloodstream was observed by setting a ROI around the perivitelline space (Figure 4.18A-B). The accumulation of NPs in this area was observed to vary based on the presence of the antiCD19 (Figure 4.18C). After 0.5 hpi, the green fluorescence signal of FITC-BSA-loaded NPs in the ROI exhibited higher values for the tNP FITC, indicating the achievement and interaction between BJAB cells and NPs from the bloodstream. These findings align with those of a previous study conducted by our research group using a similar model [98]. However, it was no longer evident at 24 hpi, when both types of NPs had accumulated to a similar extent. Similarly, the lack of a significant difference in the fluorescent signal for tNP FITC was corroborated by the decrease in FITC fluorescence associated with pH-dependent internalization following higher internalization in target cells, both *in vitro* and *in vivo*.

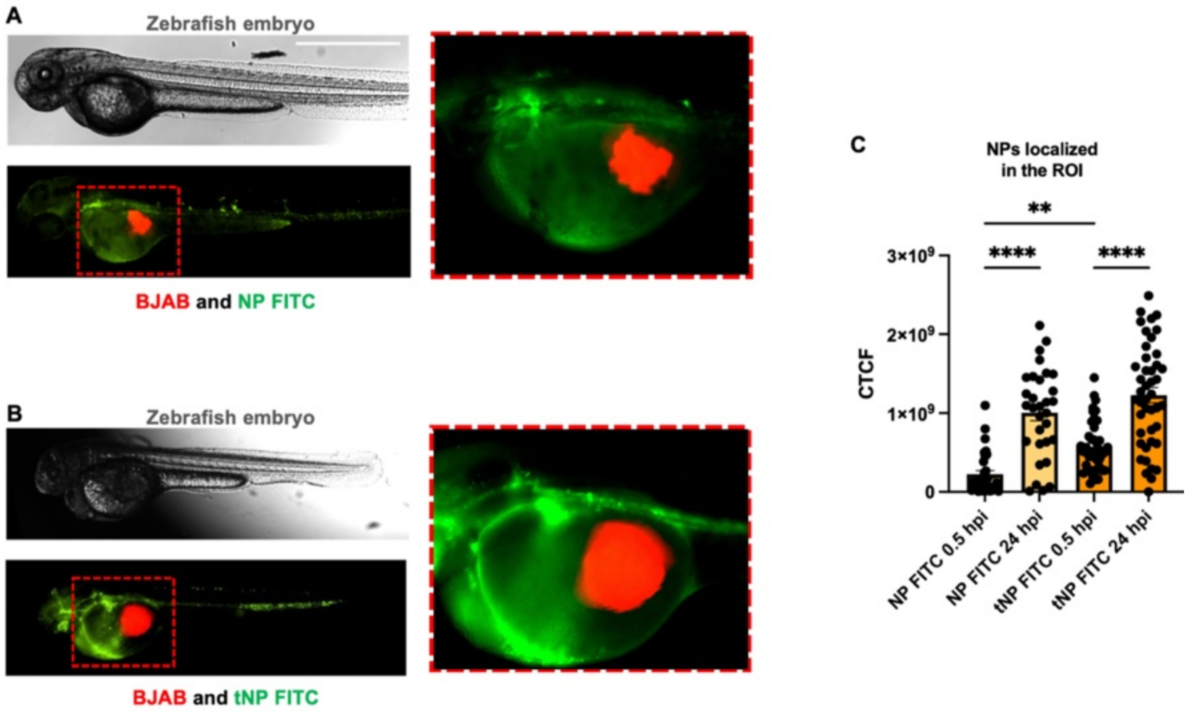

Figure 4.18. FITC-BSA-loaded NPs biodistribution studies in a Burkitt lymphoma tumor-bearing zebrafish model. Representative images at 0.5 hpi of wild type zebrafish embryos (upper panels) injected with Calcein-AM labeled BJAB cells (red fluorescence signal) in the perivitelline space and NP FITC (A) or tNP FITC (B) in the duct of Cuvier (green fluorescence signal, lower panels). ROI chosen for the analysis of the green fluorescence signals represented in the left panels. Magnification 40X (zebrafish embryo), 200X (ROI). Scale bar 1000 µm. (C) Data analysis of the CTCF of the green-fluorescent areas (FITC-BSA-loaded NPs) which arrives in the perivitelline space area of zebrafish embryos at 0.5 and 24 hpi. The values are shown as mean ± SEM of n=40. Statistical was calculated with One-way ANOVA multiple comparison test. ** = $P \leq 0.01$; **** = $P \leq 0.0001$

In conclusion, PLGA-PVA NPs exhibited a favorable safety profile in both *in vitro* and *in vivo* settings, underscoring their biocompatibility and suitability for biomedical applications. The incorporation of an antiCD19 targeting mechanism enhanced the interaction with target cells, suggesting improved cellular uptake. Altogether, these findings support the application of this nanoplatform in gene therapy as a DNA delivery system for the local expression of therapeutic proteins.

4.2. Testing transfection of DNA-loaded PLGA-PVA nanoparticles

In recent years, numerous delivery systems have been developed with the objective of ensuring the safe and effective delivery of gene therapy products. The primary focus has been on cationic NPs, particularly liposomal formulations that interact with negatively charged nucleic acids, forming a protective coating layer [203]. Similarly, polymeric NPs have gained prominence in this field. However, the literature indicates that polycations are more frequently utilized, primarily due to the aforementioned reasons [143].

The *in vitro* and *in vivo* data obtained, in addition to the physicochemical features of these NPs, provide compelling evidence for their potential use in DNA delivery. Significant advancements have been made in the field of RNA technology for medical applications; nevertheless, challenges persist, particularly regarding RNA instability and production costs [145, 153]. Most studies focused on DNA delivery, which is more stable, but on the other hand, it is mainly effective in proliferating cells like cancer cells because, unlike RNA, DNA requires its transfer into the nucleus by crossing the nuclear membrane of the cells [204].

4.2.1. Production and characterization of DNA-loaded nanoparticles

To create a platform for exogenous protein production, pDNA-loaded NPs were produced by encapsulating the EGFP-coding plasmid pEGFP-N1 in the core of NPs. This resulted in two new formulations: untargeted (NP pEGFP) and targeted (tNP pEGFP) NPs. As demonstrated for FITC-BSA-loaded NPs, the distinct payload did not affect the antiCD19 coupling efficiency or size, PDI, and charge parameters, as illustrated in Figure 4.19A. The pDNA release from NPs was evaluated in a manner analogous to that employed for FITC-BSA-loaded NPs in the aforementioned release buffer. These findings demonstrated that pDNA release from NPs was comparable to that of FITC-BSA and that the pDNA remained intact even in cytosol mimic buffer; this was essential for cell transfection. To gain insight into the structural characteristics of the system, cryo-EM technology was employed to construct models for elucidation purposes. This analysis was conducted as a service by the University of Pavia, and Figure 4.19B illustrates the packed and disordered core of nucleic acid. The amount of pDNA incorporated into NPs was determined through an indirect methodology, whereby the difference between the total amount of pDNA introduced during the preparation step and the residual unencapsulated pDNA in the solution following NPs formation was calculated. This revealed an encapsulation efficiency of 70%, comparable to that of FITC-BSA. The structural integrity of the encapsulated pDNA was analyzed by agarose gel electrophoresis after extraction of the payload from the core of NPs (Figure 4.19C). The analysis revealed that the DNA remained largely intact throughout the synthesis process, and the extracted pDNA displayed a conformation comparable to that of the untreated control.

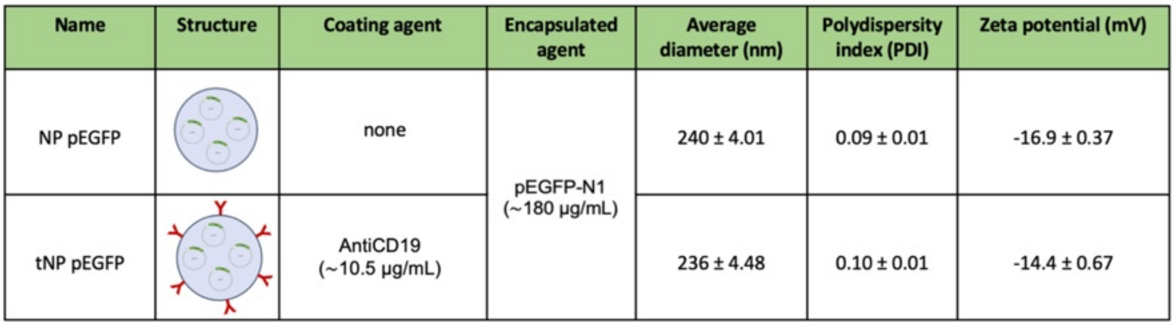

Name	Structure	Coating agent	Encapsulated agent	Average diameter (nm)	Polydispersity index (PDI)	Zeta potential (mV)
NP pEGFP		none	pEGFP-N1 (~180 µg/mL)	240 ± 4.01	0.09 ± 0.01	-16.9 ± 0.37
tNP pEGFP		AntiCD19 (~10.5 µg/mL)		236 ± 4.48	0.10 ± 0.01	-14.4 ± 0.67

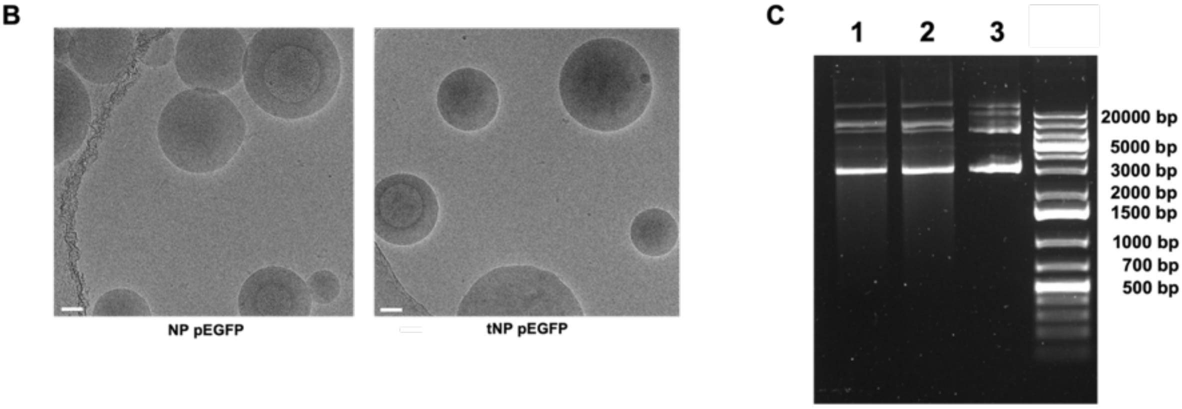

Figure 4.19. Characterization of DNA-loaded NPs. (A) Summary of the composition and features of NP pEGFP and tNP pEGFP obtained by DLS. (B) Cryo-EM images of NP pEGFP and tNP pEGFP (scale bar 50 nm). (C) Agarose gel electrophoresis of NP pEGFP (Lane 1), tNP pEGFP (Lane 2) and purified pEGFP-N1 (Lane 3) in comparison to molecular weight.

4.2.2. *In vitro* transfection studies

The efficacy of this DNA delivery platform was evaluated through *in vitro* transfection studies in both BJAB and JURKAT cells to elucidate the role of the targeting mechanism. Following a 24-hour exposure to a volume of NPs corresponding to approximately 3 µg of encapsulated pDNA, any remaining NPs that had not interacted with cells were removed and substituted with fresh medium. The initial step involved the use of mRNA levels as an indicator of *EGFP* gene expression. Subsequently, after RNA extraction, cDNA was obtained from BJAB and JURKAT cells treated with the two NPs formulations for 24 hours after which a qRT-PCR was conducted (Figure 4.20A). BJAB cells transfected with tNP pEGFP exhibited higher transcription levels of EGFP mRNA, as indicated by Relative Normalized Expression, than those treated with NP pEGFP. A comparable profile was observed in JURKAT cells, although with lower expression values than BJAB cells. This could be attributed to a nonspecific interaction between the cell membrane and NPs, which can be nonspecifically internalized by macropinocytosis [205]. These findings support the relevance of the targeting mechanism in improving the internalization of NPs in the CD19⁺ cell line, which in turn leads to a notable increase in EGFP transcription.

Furthermore, the production of EGFP was assessed over a period of up to 96 hours through flow cytometry (Figure 4.20B). The results, expressed as a percentage of EGFP⁺ cells, confirmed the hypothesis that the presence of the targeting mechanism is a determining factor in transfection efficiency. In fact, at 24 hours post-transfection, approximately 15% of BJAB cells treated with tNP pEGFP exhibited expression of the fluorescent protein in comparison to those treated with NP pEGFP which exhibited a low (~2%) transfection efficiency. The efficiency of transfection mediated by tNP pEGFP decreases over time, reaching 96 hours post-transfection a level comparable to that observed for NP pEGFP. Nevertheless, despite the qRT-PCR results indicating the presence of EGFP mRNA in JURKAT cells, the results of the flow cytometry analysis demonstrated a lack of substantial protein expression. This was corroborated by the low percentage of EGFP⁺, which was approximately 2% for both the untargeted and targeted NPs. These data confirmed that the absence of the CD19 antigen precludes a substantial internalization of NPs, thereby preventing EGFP expression.

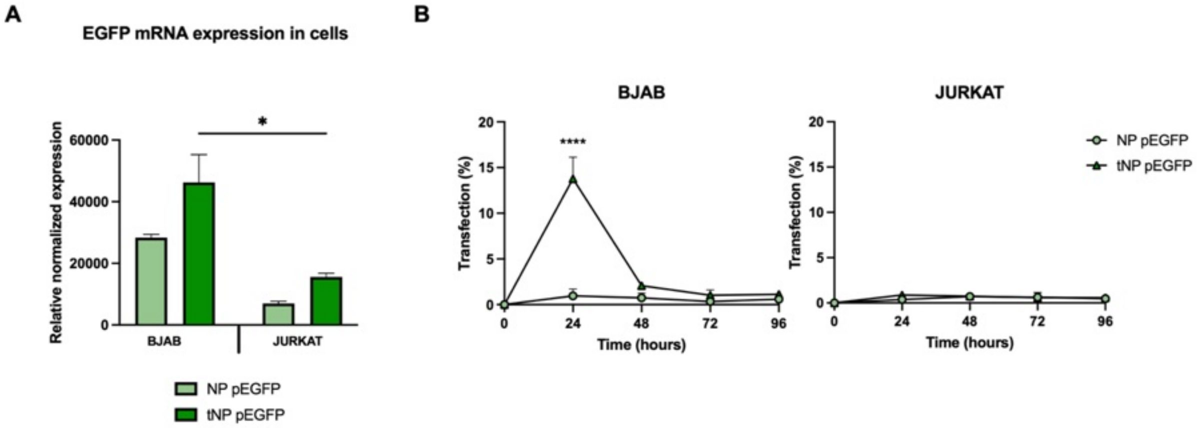

Figure 4.20. *In vitro* evaluation of the transfection efficiency. (A) qRT-PCR expression analysis of EGFP in BJAB and JURKAT cells at 24 hours post transfection with NP pEGFP and tNP pEGFP. Expression data are normalized against human *RPL34* gene. The values are shown as mean ± SD of n=3. Statistical was calculated with One-way ANOVA multiple comparison test. * = $P \leq 0.05$. (B) Transfection studies of NPs performed for up 96 hours on BJAB (left panels) and JURKAT cells (right panels) by flow cytometry. Data are expressed as % of EGFP⁺ cells. The values are shown as mean ± SD of n=3. Statistical was calculated with One-way ANOVA multiple comparison test. **** = $P \leq 0.0001$.

4.2.3. *In vivo* transfection studies in Burkitt lymphoma tumor-bearing zebrafish model

The transfection efficiency was evaluated *in vivo* in the localized BL tumor-bearing zebrafish model previously described. Approximately 2,500 unlabeled BJAB cells were injected into the perivitelline space and 4.6 nL of NP pEGFP or tNP pEGFP (equivalent to approximately 0.8 ng of encapsulated pDNA) were introduced into the duct of Cuvier 48 hpf. At 24 hpi, zebrafish embryos were euthanized and lysed for RNA extraction. Furthermore, cDNA was obtained to perform qRT-PCR (Figure 4.21A).

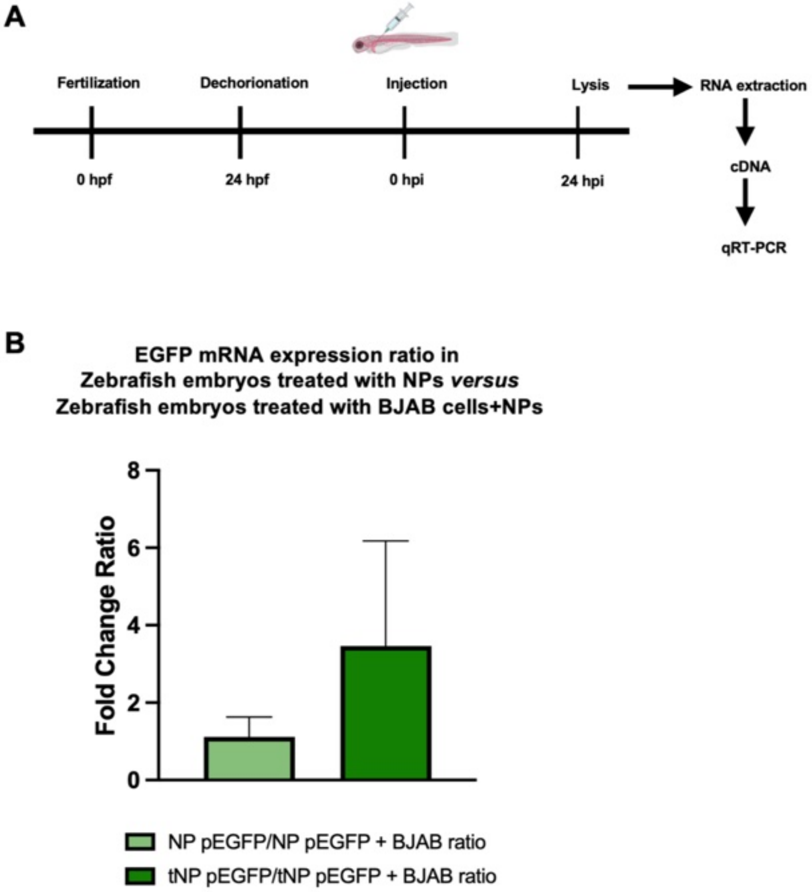

Figure 4.21. *In vivo* evaluation of the transfection efficiency. (A) Timeline of the experimental procedure. (B) qRT-PCR expression analysis of EGFP in zebrafish embryos at 24 hpi. Expression data are normalized against zebrafish *β-actin* gene and expressed as ratio between samples treated with only NPs and samples treated with both BJAB cells and NPs. The values are shown as mean ± SD of n=3. Statistical was calculated with unpaired t-test.

To assess whether the presence of human CD19$^+$ cells could enhance EGFP expression in the embryos, samples of embryos treated with only NPs were compared to those treated with BJAB cells and NPs. The results demonstrated that the ratio between samples treated with only tNP and samples treated with BJAB cells and tNP was approximately 3 times higher than the ratio between samples treated with only NP and samples treated with BJAB cells and NP (Figure 4.21B). This provided evidence that also in a more complex model, the transfection mediated by tNPs was superior to the untargeted ones in the presence of a CD19$^+$ system.

The data obtained from the transfection studies corroborate the hypothesis that the incorporation of a targeting mechanism on the surface of NPs facilitates their internalization and subsequent expression of the delivered pDNA, both *in vitro* and *in vivo*. This evidence lends support to the hypothesis that a targeted approach ensures more efficient delivery of the genetic material, which in turn leads to improved therapeutic outcomes.

4.3. *In vivo* characterization of PLGA-PVA nanoparticles in a Burkitt lymphoma mouse model

The results from zebrafish embryos provided a basis for subsequent investigations in a more complex system, such as a mouse model. In this context, several factors, including pharmacokinetics, can impact the efficacy of a therapeutic intervention. Pharmacokinetics is the study of the processes involved in the absorption, distribution, metabolism, and elimination of drugs. Following administration, the drug is available for absorption and distribution throughout the body, with 100% bioavailability. The distribution of a drug within the body determines its localization, which in turn affects both efficacy and toxicity. Given that NPs are limited in their renal clearance, the primary site for their metabolism and elimination is the liver. Consequently, biodistribution studies were performed to evaluate the accumulation and localization of NPs, followed by the assessment of their therapeutic efficacy.

4.3.1 Biodistribution studies

Biodistribution studies were performed exploiting two novel formulations of NPs encapsulating Cy5.5. The features of untargeted (NP Cyn5.5) and targeted (tNP Cyn5.5) NPs obtained are summarized in Figure 4.22 and revealed a slightly lower negative charge compared to other formulations.

Name	Structure	Coating agent	Encapsulated agent	Average diameter (nm)	Polydispersity index (PDI)	Zeta potential (mV)
NP Cyn5.5		none	Cy5.5 (~315 µg/mL)	258.66 ± 4.25	0.13 ± 0.01	-5.59 ± 0.37
tNP Cyn5.5	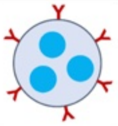	AntiCD19 (~10.5 µg/mL)		259.06 ± 6.40	0.12 ± 0.02	-8.12 ± 0.24

Figure 4.22. Characterization of Cy5.5-loaded NPs for biodistribution studies. Summary of the composition and features of NP Cyn5.5 and tNP Cyn5.5 obtained by DLS.

Biodistribution studies of NPs were conducted using *In Vivo* Imaging Systems (IVIS), a preclinical, non-invasive tool for tracking labeled molecules *in vivo*. This method is rapid, straightforward, and enables repeated assessments of the same anesthetized animal at different time points, thus obviating the necessity for animal sacrifice that is required in traditional *ex vivo* assays. A localized model of BL was induced in SCID mice, as previously described by Capolla et al [83]. SCID mice are characterized by an impairment of the adaptive immune response (B and T lymphocytes), but innate immunity (complement system, NK cells, neutrophils, and macrophages) remains active [206]. Therefore, the use of SCID mice allows the characterization of the immune response to antibody-based immunotherapeutic approaches, such as the use of NPs to produce locally antiCD20. For this purpose, BJAB ($2x10^6$ cells) were injected in the right flank of SCID mice resulting in the formation of a tumor mass at the site of injection within 20-25 days. Once the tumor mass reached a volume of 250-300 mm^3, 100 µL of NP Cyn5.5, tNP Cyn5.5 or PBS, were injected intraperitoneally. The animals were analyzed immediately following the injection and at 24-, 48-, and 72-hours post-injection. Following 48 hours, the fluorescence signal exhibited a marked decline, indicating the rapid elimination of the majority of NPs within this timeframe. Following a 72-hour observation period, the mice were sacrificed, and the organs were explanted for further analysis using IVIS to enhance accuracy. The fluorescent signal of Cy5.5 from NPs in the organs was expressed as Average Radiant Efficiency (as the ratio of emitted radiant power to input power, indicating how efficiently a system converts energy into light) and compared to the base signal of organs from animals treated with PBS, as negative control.

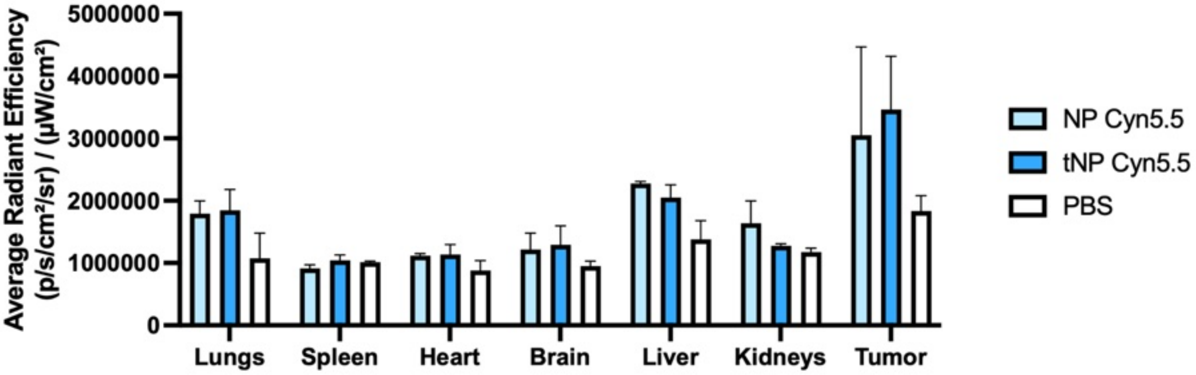

Figure 4.23. ***Ex vivo*** **analysis of Cy5.5-loaded NPs biodistribution in mice.** NPs fluorescent signal in different organs of mice at the end of the experiment. The values are shown as mean ± SEM of n=3.

As illustrated in Figure 4.23, NPs were not observed to accumulate in the spleen, heart, or brain, as evidenced by the comparable values of the fluorescence signal from NPs with the baseline fluorescence of these organs. NPs demonstrated a greater accumulation in the lungs, which can be attributed to their anatomical characteristics. In fact, the lungs possess a considerable surface area and vascular structure that facilitates NPs deposition, which can effectively interact with the alveolar-capillary interface [207], but also with resident macrophages [208]. The relatively low accumulation of NPs in the liver and kidneys can be attributed to several factors. Firstly, the typical size of these particles (exceeding 200 nm) restricts their uptake by these organs, as smaller particles (less than 10 nm) are cleared with greater efficiency. Additionally, the negative charge of the NPs reduces their interaction with serum proteins and cell membranes, which consequently results in decreased uptake by liver Kupffer cells and renal proximal tubular cells. Moreover, the liver's high blood flow rate and its role in clearing substances from the blood may impede the distribution of NPs, while the kidneys primarily filter small molecules, resulting in ineffective retention of larger NPs [103, 106].

The presence of both NP Cyn5.5 and tNP Cyn5.5 was mainly detected in the tumor mass and without a significant difference between particles. It seems reasonable to posit that the accumulation was primarily driven by the EPR effect. In fact, tumors often exhibit an anomalous vascular configuration with augmented permeability, which allows NPs to traverse the leaky blood vessels and accumulate within the tumor tissue [118]. The effective vascularization of the tumor masses was identified by immunofluorescence analysis on tumor masses sections through the use of an anti-Mouse von Willebrand factor antibody. This methodology permitted the assessment of the von Willebrand factor expression, a conventional endothelial cell marker, in tumor masses. As illustrated in Figure 4.24, the presence of blood vessels was discernible in the two representative tumor masses analyzed. Furthermore, both types of NPs were identified in close proximity to the vasculature. This allowed us to hypothesize that the NPs reached the tumor through the bloodstream and then extravasated due to the increased permeability and fenestrations of the vessels, accumulating in the TME. This allowed us to posit that the presence of the antiCD19 targeting mechanism did not contribute to the accumulation in the TME. Nevertheless, previous studies conducted by our laboratory have demonstrated that the presence of a targeting mechanism is a crucial factor in the internalization of NPs within the TME following their arrival at this site, but not for their accumulation [83].

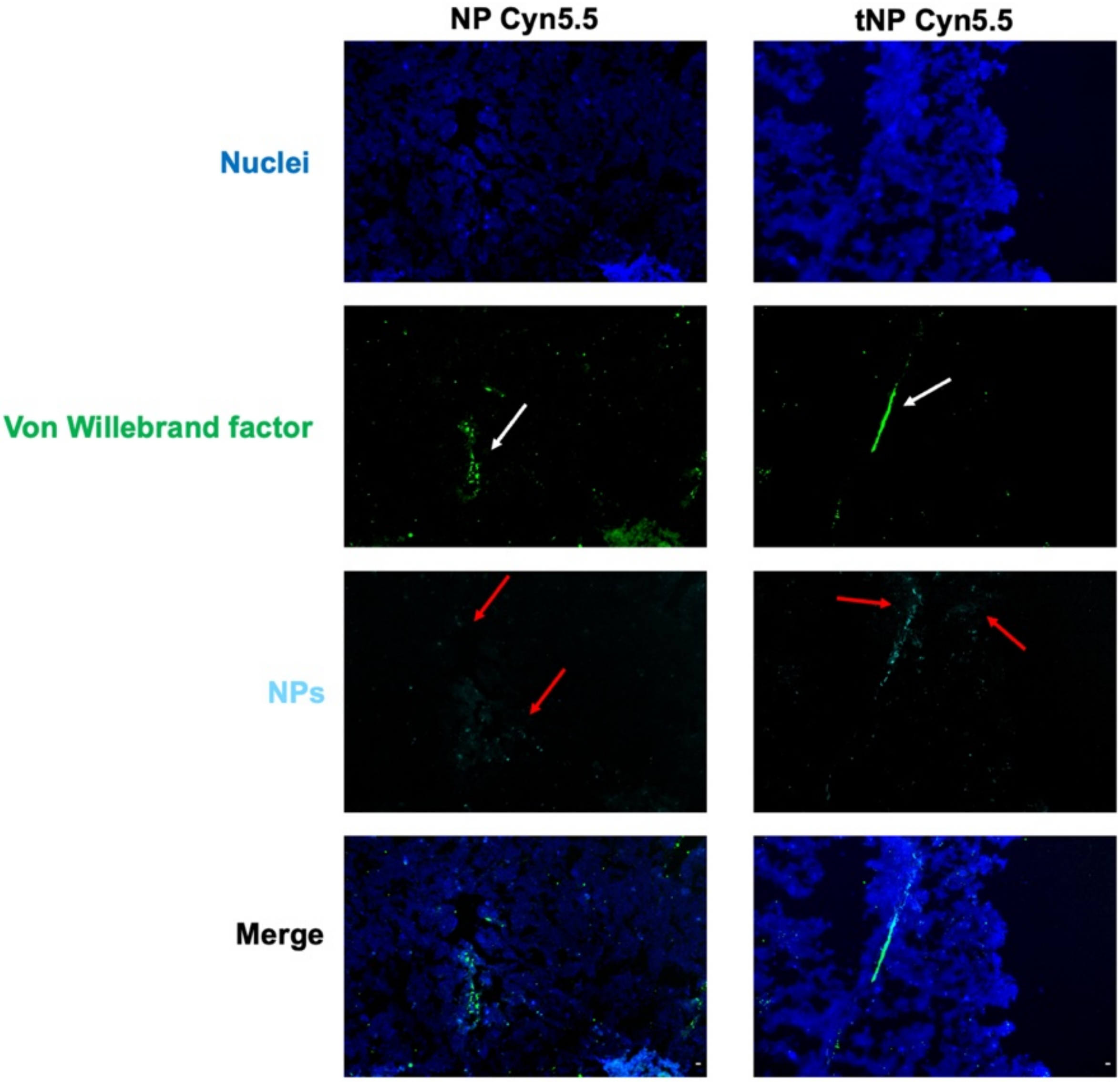

Figure 4.24. Representative images of *ex vivo* analysis of the vascularization and accumulation of Cy5.5-loaded NPs in tumor mass. At the end of the study, tumor mass sections were analyzed by fluorescence microscopy. Nuclei were stained with DAPI. Vasculature (green fluorescence) was stained with Rabbit anti-Mouse von Willebrand Factor and FITC-conjugated anti-Rabbit IgG antibody. The presence of NPs (cyan fluorescence, red arrows) can be appreciated in proximity of blood vessels (white arrows). Magnification 200X. Scale bar 10 µm

The presented evidence provides support for the use of this Burkitt lymphoma tumor model, derived from $CD19^+$ and $CD20^+$ cells, which exhibit a distinctive degree of vascularization that ensures the arrival of NPs, which accumulate mainly due to the EPR effect.

4.4. Therapeutic potential of nanoparticles delivering antiCD20-coding pDNA for targeted therapy

The use of antibodies as a treatment for disease has its origins in experiments conducted in the 1890s. However, the administration of therapeutic monoclonal antibodies frequently necessitates the use of high doses, which are delivered via prolonged infusions or multiple injections. This, in conjunction with the exorbitant costs associated with the production of clinical-grade proteins and the brief serum half-lives that necessitate repeated administrations to achieve therapeutic benefits, presents significant challenges to the large-scale treatment of patients, particularly in developing regions. The potential for nucleic acid-based approaches to deliver antibody gene sequences for *in situ* monoclonal antibody production has long been a goal of the gene therapy field, given the rapid scalability of such techniques. The application of gene therapy to transform the body's cells into "*in situ* bioreactors" that produce therapeutic monoclonal antibodies has the potential to minimize the need for high doses, prolonged infusions, and the associated side effects of monoclonal antibody treatments. This approach could facilitate the administration of single or periodically spaced injections, thereby enabling the continuous and sustained production of therapeutically effective monoclonal antibody levels. The initial outcome should be the alteration of the TME, transforming it from an immunologically cold to an immunologically hot state but also a direct therapeutic effect could be observed.

In this field, non-viral vectors, such as NPs, can be exploited for gene transfer.

4.4.1. Production and characterization of the therapeutic protein

As previously stated, the antiCD20 antibody Rituximab marked a transformative era of treatment for nearly B-cell NHL representing the standard of care. For this reason, it has been selected as a prototype of therapeutic protein to be produced directly in the TME through NPs.

Prior to the production and testing of NPs, it was essential to produce, purify, and characterize the therapeutic protein *in vitro* to confirm its functionality and therapeutic potential.

First, Rituximab was produced as a recombinant protein defined as antiCD20, comprising a scFv, which is a fusion protein of the variable regions VH and VL of immunoglobulins connected by a short linker peptide encoded in frame with the Fc region, specifically the Hinge-CH_2-CH_3 domains of an antibody, as for the antiCD19 targeting mechanism. The scFv design is based on the VH and VL regions of a monoclonal murine antibody (Patent n°: N.5,736,137), also known as 2B8. The published amino acid sequences were optimized for production in CHO cells and subsequently cloned in frame with the Hinge-CH_2-CH_3 domains of human IgG1 in the eukaryotic expression vector pcDNA3.1/Hygro+. The resulting vector coding for the antiCD20 is defined as pAntiCD20. Thus, the antiCD20 shows the same structure (Figure 4.25A) as the antiCD19 except for the VL and VH. The antiCD20 was produced in CHO cells, and it was purified in order to validate it.

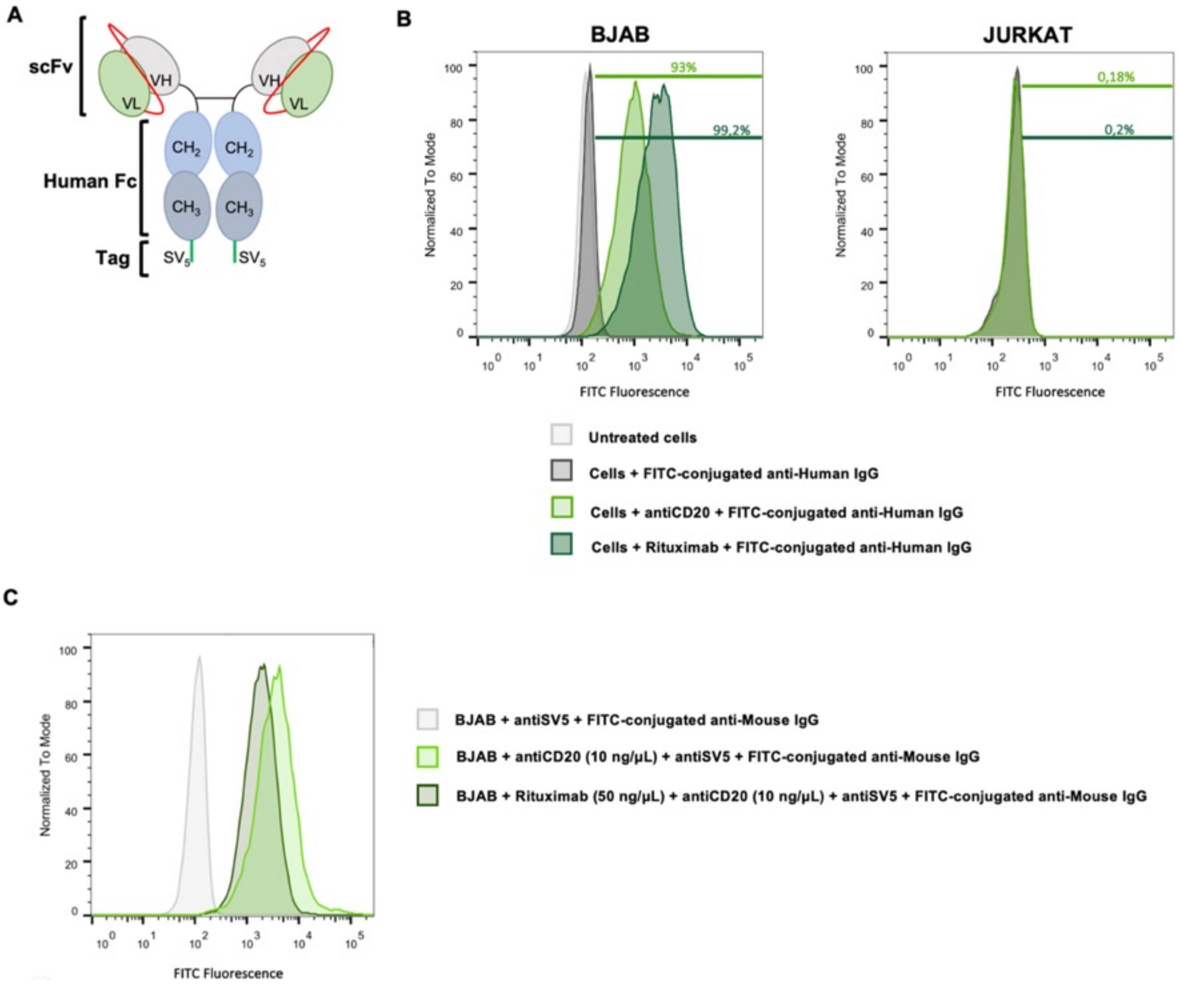

Figure 4.25. AntiCD20 therapeutic protein. (A). Schematic representation of the antiCD20 therapeutic protein constituted by a scFv (VH, grey, and VL, light green) linked through a hinge to the human Fc (CH_2-CH_3, blue), which is fused with an SV_5 tag (green). (B) Binding of the antiCD20 therapeutic protein to BJAB (left panel), and JURKAT (right panel) cells. Cells were incubated with antiCD20 or Rituximab and FITC-conjugated anti-Human IgG antibody (green peaks) or FITC-conjugated anti-Human IgG antibody alone (grey peaks) and analyzed by flow cytometry. Untreated cells (light grey peaks) and cells + FITC-conjugated anti-Human IgG antibody act as negative controls. Data are expressed as % of CD20$^+$ cells. (C) Binding competition between antiCD20 and Rituximab by flow cytometry. BJAB cells were incubated with antiCD20 and a mouse-antiSV5 antibody and FITC-conjugated anti-Mouse IgG antibody (dark green peak) or preincubated with saturating Rituximab and

mouse-antiSV5 antibody and FITC-conjugated anti-Mouse IgG antibody (light green peak). Cells + mouse-antiSV5 antibody and FITC-conjugated anti-Mouse IgG antibody (light grey peak) act as negative control. Data are expressed as % of CD20$^+$ cells.

The purified antiCD20 was tested for its binding to the CD20 antigen and compared to Rituximab. To this end, antiCD20 was incubated with BJAB cells, which served as the relevant CD20$^+$ cell model, and JURKAT cells, which served as the relevant CD20$^-$ cell model. The antigen-antibody interaction was evaluated through the use of a FITC-conjugated anti-Human IgG antibody as the secondary antibody (Figure 4.25B). The flow cytometric analysis demonstrated that the percentage of CD20$^+$ bound cells was comparable between antiCD20 and Rituximab, with the former exhibiting a value of 93% and the latter a value of 99.2%. No shift in fluorescence was observed in JURKAT cells. These findings substantiate the specificity of the protein produced.

Flow cytometry was exploited for a competition assay to confirm that the antiCD20 binds the same epitope as Rituximab. BJAB cells were pre-incubated with Rituximab in order to saturate epitopes on CD20 antigens; then, cells were incubated with antiCD20, which binding was revealed through a mouse-antiSV5 and a FITC-conjugated anti-Mouse IgG antibody in order to evaluate only the binding of antiCD20. Data were compared with BJAB cells incubated only with antiCD20 and revealed with the previously used secondary antibodies to observe the possible maximum binding of the protein. As shown in Figure 4.25C, Rituximab competed with antiCD20 for the binding of the CD20 antigen, resulting in a reduction in the MFI (from 5600 in cells incubated with only antiCD20 to 2500 in cells pre-incubated with Rituximab). These findings substantiated that both Rituximab and antiCD20 recognized the same epitope and that the reconstruction of Rituximab as a recombinant antibody was carried out correctly, about the sequence as well as for the structure and the ability to recognize the antigen.

The subsequent step was to assess the ability of antiCD20 to induce cell lysis via the CDC mechanism. To this end, a Calcein retention assay was conducted, a method used to evaluate CDC in target cells by labeling them with Calcein, a non-toxic fluorescent dye that can diffuse across the cell membrane. Once inside, Calcein is cross-linked and retained within the cytoplasm. After complement activation, the cell membrane becomes permeable, leading to the release of Calcein into the extracellular medium. This results in a reduction in intracellular fluorescence, serving as a marker of CDC. BJAB cells were labelled with Calcein-AM and then incubated with Rituximab or antiCD20; to assess CDC, normal human serum was added for 1 hour at 37°C. The cell lysis was evaluated by flow cytometry counting Calcein-AM positive cells in the samples and expressed as a percentage in comparison to untreated cells. As shown in Figure 4.26, Rituximab and antiCD20 caused comparable cell lysis (~36% and ~23% respectively), confirming the therapeutic potential of antiCD20.

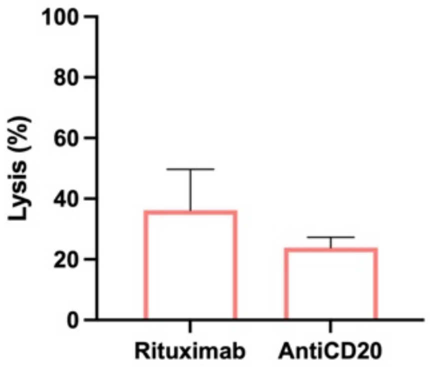

Figure 4.26. CDC performed by antiCD20. % of lysis obtained from the Calcein retention assay by treating BJAB cells with Rituximab or antiCD20 and normal human serum. The values are shown as mean ± SD of n=3. Statistical was calculated with unpaired t- test.

In conclusion, the pAntiCD20 vector was observed to have the capacity to produce a specific and active protein, thereby establishing itself as a model vector for the local production of a therapeutic protein in lymphoma.

4.4.2. Therapeutical efficacy of the antiCD20 produced by tumor B cells transfected *in vivo*

Based on the *in vitro* results obtained regarding the therapeutic efficacy of the antiCD20, two novel formulations of NPs encapsulating the pDNA coding for this protein (pAntiCD20) were produced. The goal was to exploit NPs as a delivery system to induce the production of the therapeutic protein directly within the TME, primarily by CD19$^+$ cells, with the aim of maximizing therapeutic efficacy and minimizing off-target effects. The features of untargeted (NP pAntiCD20) and targeted (tNP pAntiCD20) NPs obtained are summarized in Figure 4.27.

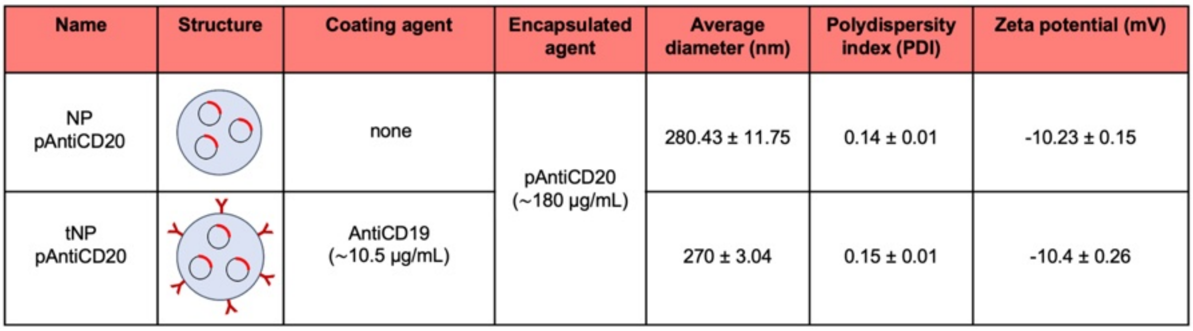

Name	Structure	Coating agent	Encapsulated agent	Average diameter (nm)	Polydispersity index (PDI)	Zeta potential (mV)
NP pAntiCD20		none	pAntiCD20 (~180 µg/mL)	280.43 ± 11.75	0.14 ± 0.01	-10.23 ± 0.15
tNP pAntiCD20		AntiCD19 (~10.5 µg/mL)		270 ± 3.04	0.15 ± 0.01	-10.4 ± 0.26

Figure 4.27. Characterization of DNA-loaded NPs for therapeutical purposes. Summary of the composition and features of NP pAntiCD20 and tNP pAntiCD20 obtained by DLS.

To assess the efficacy of pAntiCD20-loaded NPs in inducing antiCD20 production within the TME, a localized model of BL was established as described in paragraph 4.3.1. Once the tumor mass reached 250-300 mm^3, the mice were administered 8 intraperitoneal injections (on days 0, 2, 4, 7, 9, 11, 14, and 16) of either PBS (as a control group) or a volume of NP pAntiCD20 or tNP pAntiCD20 corresponding to approximately 3 µg of encapsulated pDNA. In order to ascertain the optimal administration schedule, we leveraged the findings of prior biodistribution studies, which indicated that the NPs reached their maximum accumulation in the tumor mass 48 hours following injection. Tumor mass dimensions were measured thrice weekly with a caliper to assess the impact of antiCD20 production on tumor growth. The tumor dimension was expressed as a change in measurement (Δ variation) to consider the progressive increment in size from the initial measurement (250-300 mm^3), which was taken at the commencement of the treatment. Observations were conducted until the tumor mass of the animals reached a size of 10% of the mice's body weight.

Although biodistribution data indicated that NPs could reach the tumor mass, neither type of NP was effective in achieving the secondary aim of this approach, which was a visible therapeutic outcome. However, it should be noted that the primary endpoint was the modification of the TME, and the results of this will be discussed later. As illustrated in Figure 4.28A, the tumor growth patterns observed in mice treated with NP pAntiCD20 or tNP pAntiCD20 were comparable to those observed in mice treated with PBS. However, a slight improvement in survival rate was observed. The Kaplan–Meier curves presented in Figure 4.28B illustrate the survival rates of NPs-treated tumor-bearing mice in comparison to the control group of PBS. It is noteworthy that three of the mice treated with PBS died before the conclusion of the eight-treatment regimen. The remaining two were humanely euthanized prior to three weeks following the initial treatment due to the substantial size of the tumor mass. In contrast, the data indicated that the mean survival of mice treated with NPs was longer than that of the control group. In fact, only one mouse treated with NP pAntiCD20 did not complete the eight treatments, while the other two survived for 25 and 28 days following the initial treatment. The mice treated with tNP pAntiCD20 demonstrated a slight improvement in the survival rate with a maximum lifespan of approximately one month following the initial treatment. The data collectively indicate that treatment with NPs, both with and without a targeting mechanism, may modestly enhance survival rates compared to the control group. However, tNP pAntiCD20 appears to confer a slightly more pronounced benefit.

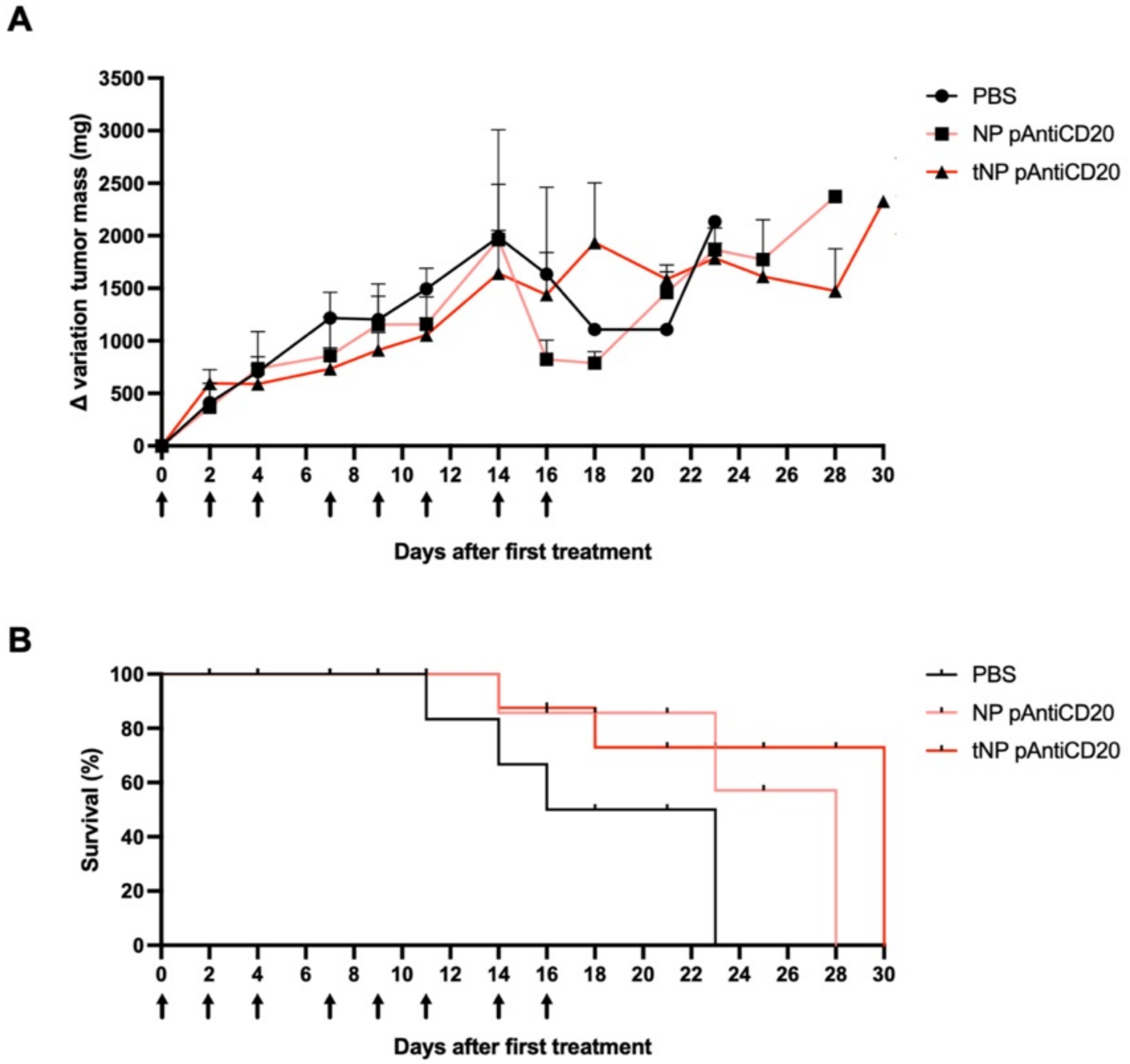

Figure 4.28. *In vivo* therapeutic efficacy of pAntiCD20-loaded NPs. (A) Graph that recapitulates the tumor growth trend of the 3 experimental groups. In black line the tumor growth trend of the group of mice treated with PBS (n = 5); in pink line the tumor growth trend of the group of mice treated with NP pAntiCD20 (n = 3); in red line the tumor growth trend of the group of mice treated with tNP pAntiCD20 (n = 5). Data are represented as mean ± SEM. (B) Kaplan–Meier curve of mice survival. The survival of mice treated with NPs (pink line for NP pAntiCD20 and red line for tNP pAntiCD20) was compared with the mice treated with PBS (black line). Statistical was calculated with Log-rank test.

Furthermore, the mice that received multiple injections of NPs did not demonstrate any adverse effects, including diarrhea, vomiting, convulsions, dehydration, tachypnea, dyspnea, and lethargy. No notable discrepancies in organ weight (i.e., spleen, heart, lungs, liver, and kidneys) were discerned when compared to mice treated with PBS, thereby indicating the absence of overt indications of organ toxicity. This corroborated the favorable safety profile of these NPs, as previously assessed *in vivo* in the lymphoma zebrafish model and *in vitro*, including the endothelial cells-human whole blood model.

In light of the biodistribution study, which demonstrated that NPs reached the tumor mass, a hypothesis was formulated that the absence of a substantial therapeutic effect may be attributed to a low transfection efficiency within the tumor mass, which subsequently results in reduced antiCD20 local production. Consequently, the presence of antiCD20 produced locally by cells in the TME was evaluated through immunofluorescence analysis, utilizing a FITC-conjugated anti-Human IgG antibody.

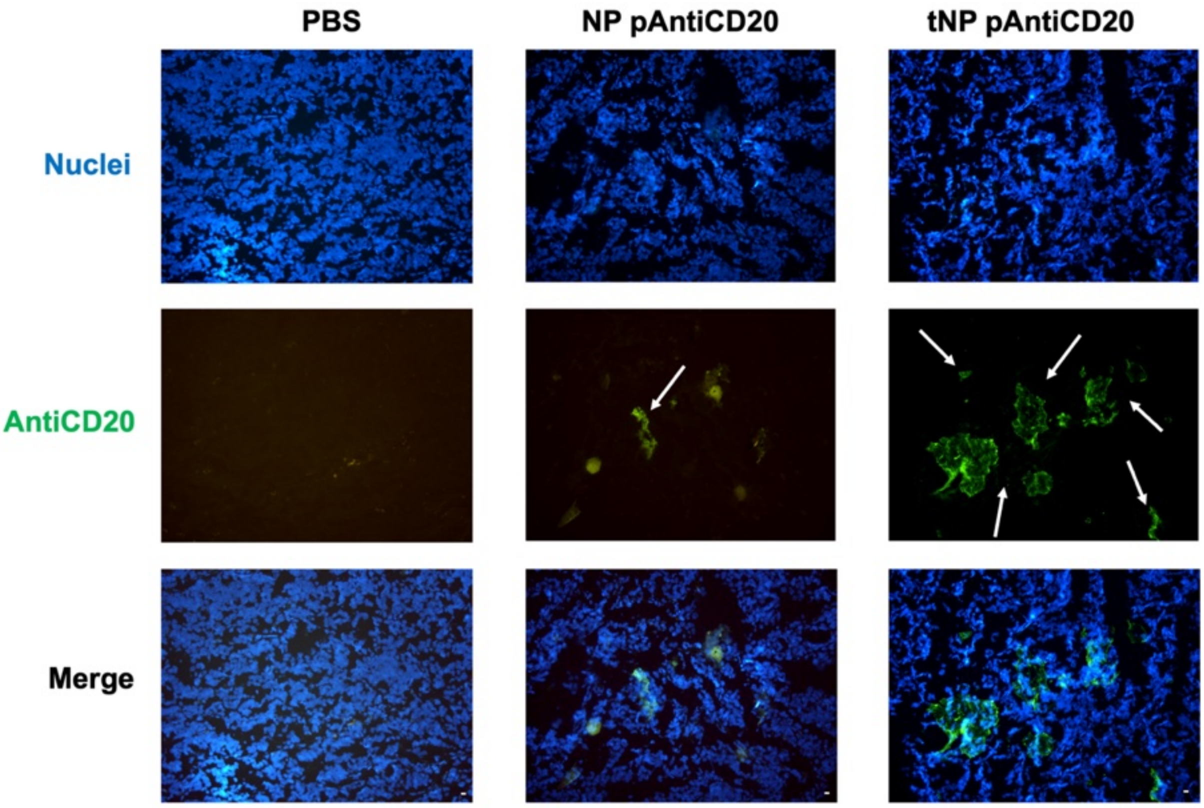

Figure 4.29. Representative images of *ex vivo* analysis of the antiCD20 production in tumor mass. At the end of the study, tumor mass sections were analyzed by fluorescence microscopy. Nuclei were stained with DAPI. AntiCD20 deposition (green fluorescence, white arrows) was stained with FITC-conjugated anti-Human IgG. Magnification 200X. Scale bar 10 µm

Figure 4.29 demonstrates that NP pAntiCD20 is an effective delivery system for the antiCD20-coding pDNA, resulting in the successful production and binding of the antiCD20 therapeutic protein to tumor mass cells, as evidenced by the green fluorescence signal in the NP pAntiCD20 group. In the absence of the antiCD19 targeting mechanism, which has been demonstrated to enhance the internalization of NPs *in vitro*, the result obtained from untargeted pAntiCD20-loaded NPs is probably attributable to a minimal endocytosis process, as has been observed previously also *in vitro*. The green fluorescence signal in the tNP pAntiCD20 group is more pronounced and discernible, suggesting augmented antiCD20 production *in vivo* and consequent binding to tumor mass cells in accordance with the enhanced transfection efficiency observed *in vitro*. However, it is essential to consider that the FITC-conjugated anti-Human IgG antibody utilized in the analysis may recognize any human IgG. Consequently, a portion of the signal may be attributed to the antiCD19 on tNP pAntiCD20, potentially complicating the interpretation of the presence and distribution of the antiCD20. However, it is essential to consider the transfection results obtained *in vitro*, which indicated that tNPs exhibited superior cellular uptake compared to untargeted formulations. This observation may support the hypothesis that tNP pAntiCD20 leads to higher pDNA delivery and, consequently, greater antiCD20 local production and binding to CD20$^+$ B cells of the tumor mass. Additionally, the absence of a green fluorescence signal in the control group of PBS demonstrated the efficacy of the NP-mediated delivery system. Notwithstanding the identification of a signal of Human IgG in tumor masses sections, the therapeutic outcome was not significant. However, it is relevant to note that the therapeutic effect was the secondary objective of this approach, whereas the primary one was to exploit it to induce changes in the TME, thereby making it immunologically active.

As previously described, the binding of Rituximab (and thus also antiCD20) to CD20 antigen on the B-cell surface results in the activation of the complement cascade through the classical pathway. To this end, we conducted an immunofluorescence analysis to examine the deposition of C1q in the tumor masses (Figure 4.30).

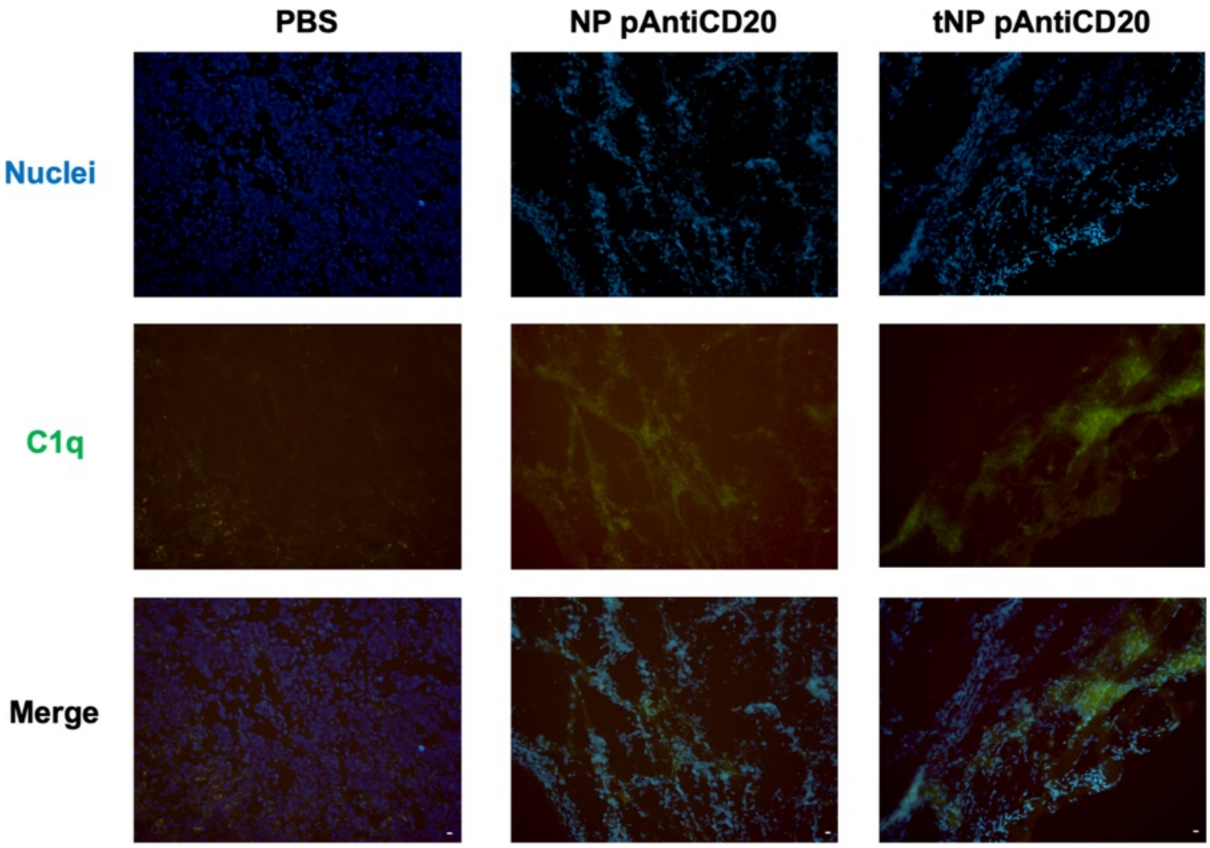

Figure 4.30. Representative images of *ex vivo* analysis of the C1q deposition in tumor mass. At the end of the study, tumor mass sections were analyzed by fluorescence microscopy. Nuclei were stained with DAPI. C1q deposition (green fluorescence) was stained with Rat anti-Mouse C1q and FITC-conjugated anti-Rat IgG antibody. Magnification 200X. Scale bar 10 μm

C1q deposition was more documented in tumor mass sections from mice treated with tNP pAntiCD20. In contrast, the evidence was less discernible in the tumor sections from mice treated with NP pAntiCD20 and was not observed in the samples obtained from mice treated with PBS. It is evident that the signal was not localized, but rather appeared diffused, suggesting the potential production of antiCD20 in these regions and, consequently, the C1q binding. The higher signal from samples treated with tNP pAntiCD20 in comparison to those treated with NP pAntiCD20 may be related to the better transfection efficiency of targeted NPs, previously observed both *in vivo* and *in vitro*. It can be reasonably assumed that the presence of the antiCD19 targeting mechanism on the tNP pAntiCD20 surface may have triggered the C1q deposition. However, the previous CH50 study, described in paragraph 4.1.3, allowed us to exclude this possibility, demonstrating that both targeted and untargeted NPs did not significantly impair complement system function through the classical pathway.

C1q is distinct from the majority of complement proteins, which are exclusively produced by hepatocytes. It can also be synthesized in a local environment by a diverse range of cell types, including macrophages and dendritic cells. Local synthesis thus provides an alternative means by which C1q can perform specific functions *in situ*, which are directly linked to its site of production, without triggering complement activation. C1q, when expressed in the vascular endothelium of several human malignant tumors, has been demonstrated to act as a tumor-promoting factor. This is evidenced by its ability to favor adhesion, migration, and proliferation of cancer cells, as well as angiogenesis and metastasis [209]. However, the lack of substantial C1q presence in PBS-treated mice tumor masses permitted the assumption that the C1q detected in those from NPs-treated mice was associated with antiCD20 production.

To ascertain whether complement system activation occurs, the presence of complement C3-activation fragments C3b, iC3b, and C3c was detected in tumor sections (Figure 4.31).

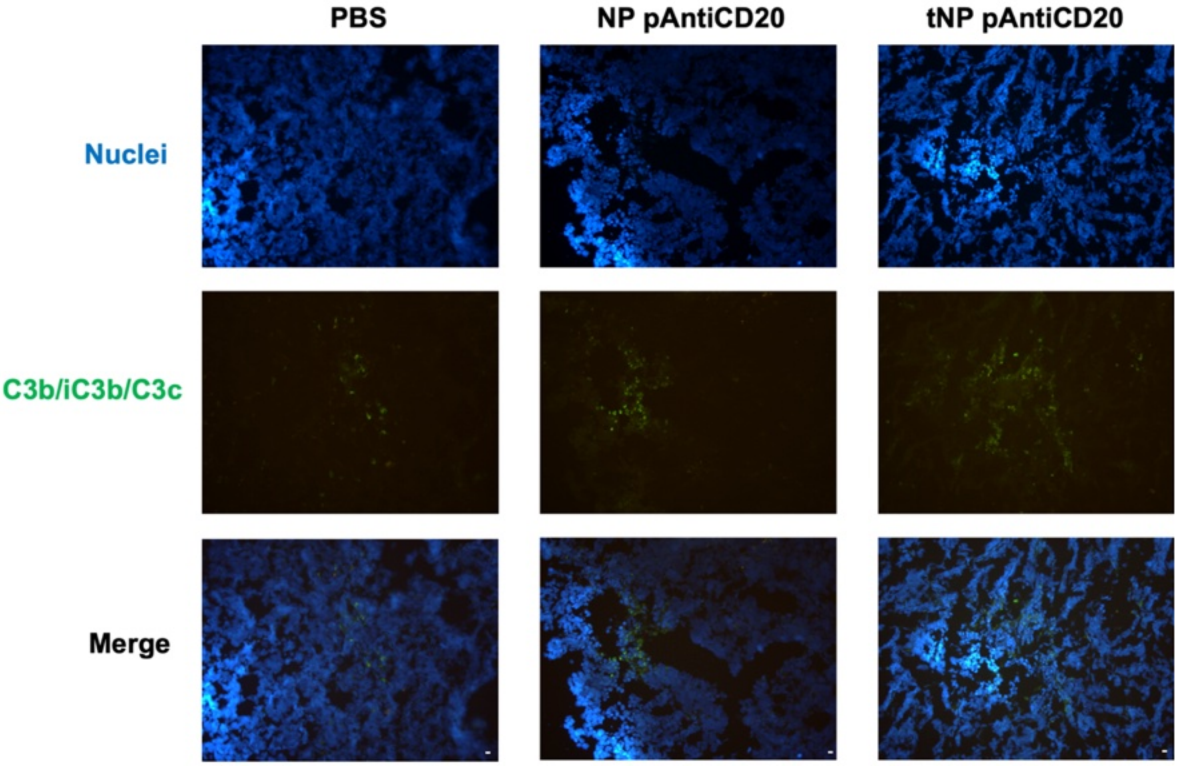

Figure 4.31. Representative images of *ex vivo* analysis of the C3b/iC3b/C3c deposition in tumor mass. At the end of the study, tumor mass sections were analyzed by fluorescence microscopy. Nuclei were stained with DAPI. C3b/iC3b/C3c deposition (green fluorescence) was stained with Rat anti-Mouse C3b/iC3b/C3c and FITC-conjugated anti-Rat IgG antibody. Magnification 200X. Scale bar 10 μm

The presence of C3-activation fragments in tumor mass sections from mice treated with NPs indicated a potential complement system activation resulting from the antiCD20 locally produced. In particular, the lower signal from NP pAntiCD20-treated mice indicated a partial complement system activation in comparison to the tNP pAntiCD20-treated ones. However, it is established that all three complement pathways (classical, alternative, and lectin) culminate in the generation of C3 convertases, which cleaves the C3 protein [210]. This may account for the signal observed in tumor masses from mice treated with PBS, indicating the possibility of alternative pathway activation. Consequently, a portion of the observed presence of activation fragments may be attributed to this contribution.

Subsequently, the activation of the complement system results in the formation of anaphylatoxins, such as C3a and C5a, and the recruitment of leukocytes as inflammatory cells from the bloodstream [211]. In fact, it is established that C5a is a chemoattractant molecule that can modulate the activity of numerous cell types, including macrophages and neutrophils, within the context of the immune system [212]. Accordingly, the recruitment of PMN leukocytes, which are involved in the body's rapid immune response, was analyzed in tumor mass sections by immunofluorescence. As illustrated in Figure 4.32, there was a notable accumulation, at varying amounts, of PMNs in both samples treated with PBS and NPs. Specifically, the slight accumulation in mice treated with PBS may be related to tumor-driven inflammation. In fact, the injection of human cancer cells into SCID mice has been shown to stimulate an innate immune response at the tumor site, which involves neutrophil recruitment [213]. In comparison, the recruitment of PMNs is more appreciable in mice treated with NPs, which suggests that these NPs play an effective role. Specifically, the signal from mice treated with tNP pAntiCD20 is higher than that from mice treated with NP pAntiCD20. This could be directly connected to the C1q deposition previously described. In fact, a slight antiCD20 production and deposition of C1q was observed in NP pAntiCD20-treated mice. Subsequently, antiCD20-mediated cell destruction can result in the triggering of an inflammatory response due to complement system activation and C5a formation. This, in turn, leads to the recruitment of PMNs to the tumor site as part of the immune response. This phenomenon is more pronounced in mice treated with tNP pAntiCD20, where the antiCD19 targeting mechanism likely facilitates the internalization of NPs at the tumor site, which may result in enhanced local antiCD20 production. It is reasonable to hypothesize that this could result in a higher concentration of antiCD20 bound to the tumor cells, which in turn led to a higher level of complement system activation, as evidenced by the increased C1q deposition. Accordingly, the supposed augmented complement activation, in conjunction with the destruction of tumor cells via antiCD20, attracts a greater number of PMNs to the site as part of the inflammatory and immune response.

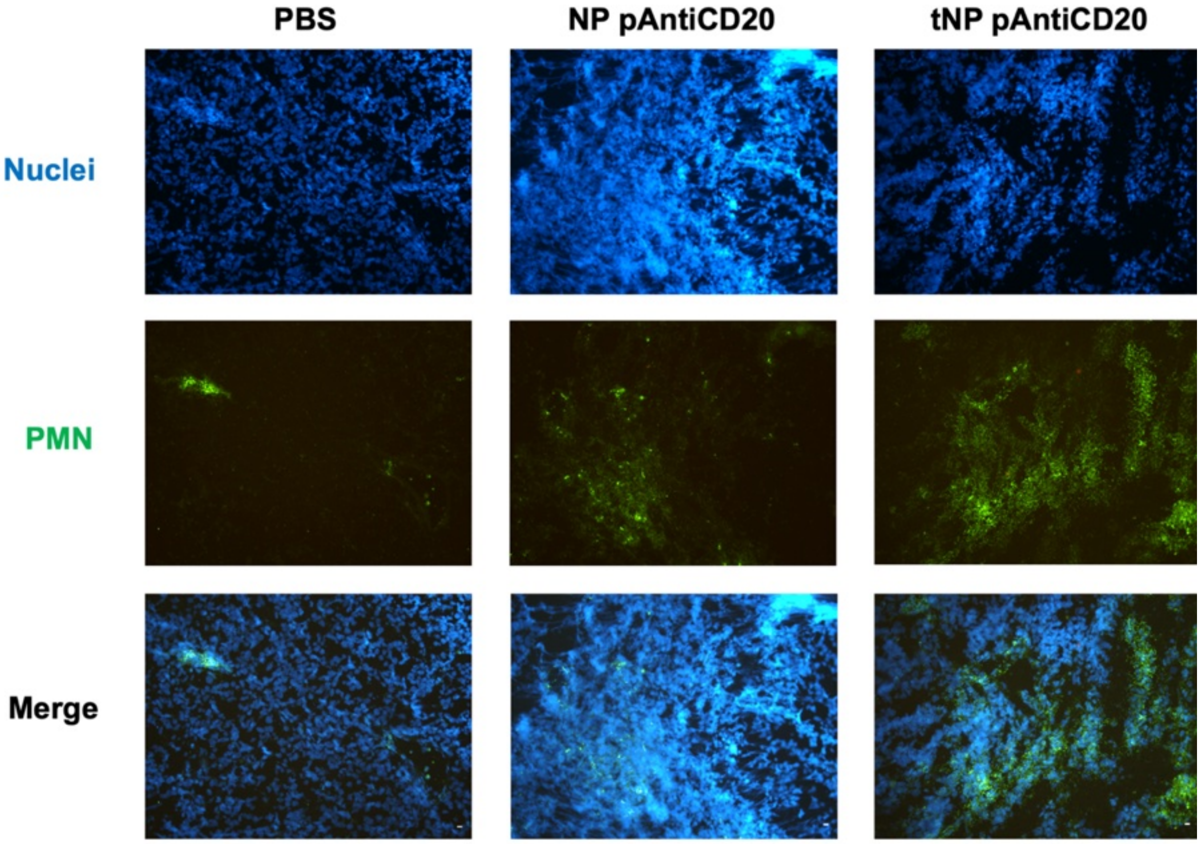

Figure 4.32. Representative images of *ex vivo* analysis of the PMN recruitment in tumor mass. At the end of the study, tumor mass sections were analyzed by fluorescence microscopy. Nuclei were stained with DAPI. PMNs (green fluorescence) were stained with FITC conjugated anti-Mouse PMN antibody. Magnification 200X. Scale bar 10 µm

Furthermore, the migration and infiltration of immune cells, such as $CD14^+$ macrophages and $CD56^+$ NK cells, were examined through immunofluorescence analysis on tumor mass sections. This is because both types of immune cells are instrumental in ADCC, which represents another mechanism through which Rituximab (and subsequently, antiCD20) exerts its anti-tumor effects.

In tumor sections of mice treated with PBS and NP pAntiCD20, signals corresponding to CD56 (Figure 4.33) and CD14 (Figure 4.34) expression were barely detectable. On the contrary, a slightly more noticeable presence of these cells was detected in tumor sections from mice treated with tNP pAntiCD20.

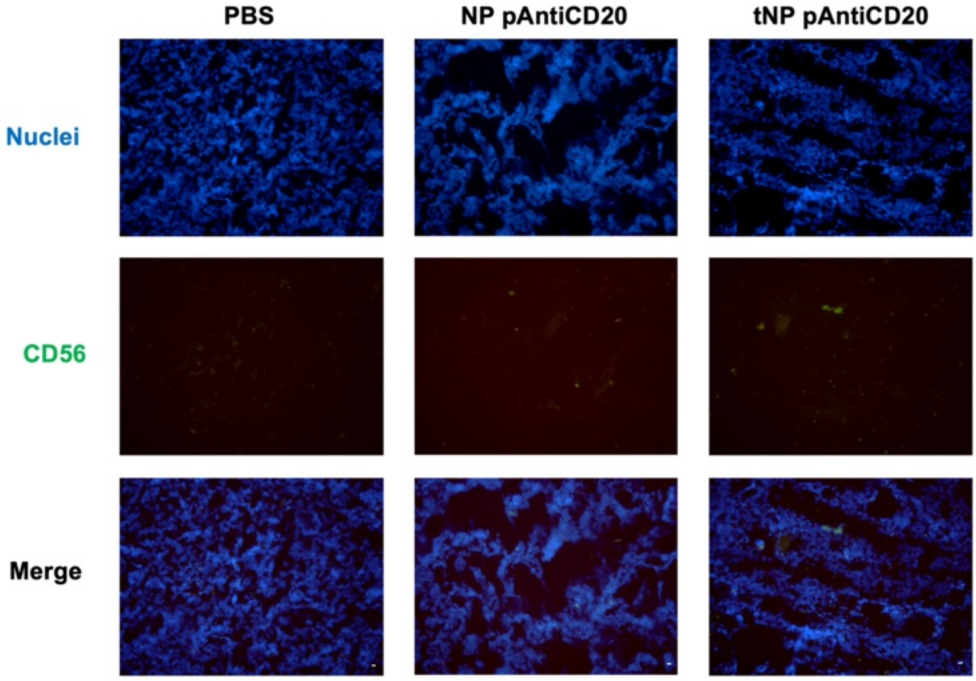

Figure 4.33. Representative images of *ex vivo* analysis of the CD56 protein of NK cells recruited in tumor mass. At the end of the study, tumor mass sections were analyzed by fluorescence microscopy. Nuclei were stained with DAPI. CD56 protein of NK cells (green fluorescence) were stained with Rat anti-Mouse CD56 and FITC conjugated anti-Rat IgG antibody. Magnification 200X. Scale bar 10 µm

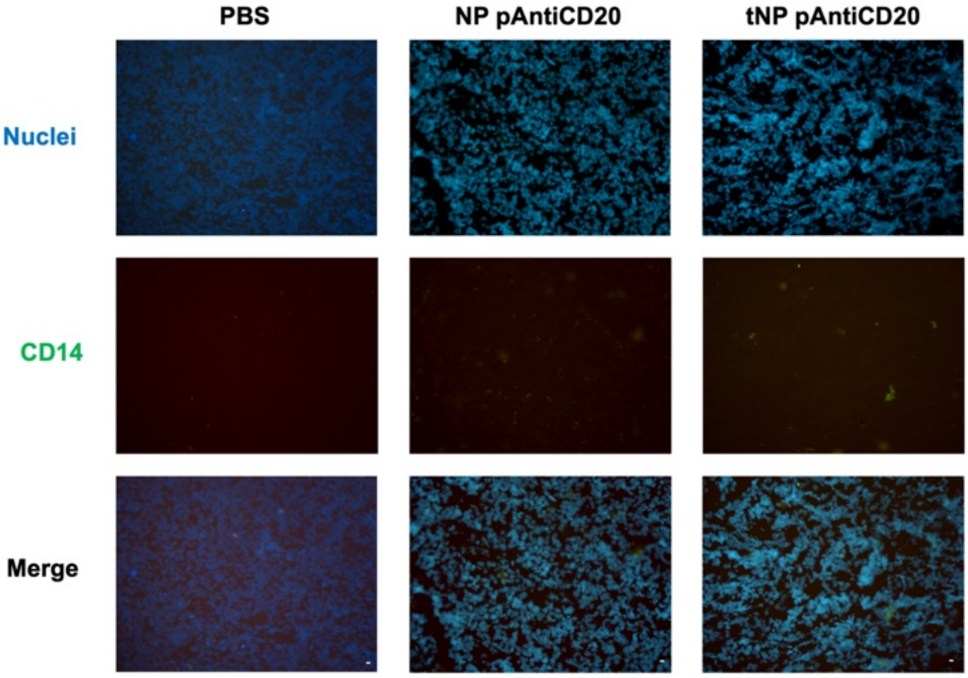

Figure 4.34 Representative images of *ex vivo* analysis of the CD14 protein of macrophages recruited in tumor mass. At the end of the study, tumor mass sections were analyzed by fluorescence microscopy. Nuclei were stained with DAPI. CD14 protein of macrophages (green fluorescence) were stained with Rabbit anti-Mouse CD14 and FITC conjugated anti-Rabbit IgG antibody. Magnification 200X. Scale bar 10 μm

In light of the preceding outcomes, it is feasible to elucidate that the mice that underwent PBS treatment, serving as a control group, did not undergo any therapeutic intervention. SCID mice are immunodeficient, exhibiting a deficiency in both T and B cells. However, they retain a partial innate immune response, including neutrophils, macrophages, and NK cells. The absence of C1q, a pivotal complement protein, indicates that in the absence of a therapeutic stimulus, the immune response is not significantly activated to recruit complement proteins or effector immune cells. Therefore, the expected result is minimal infiltration of PMNs, macrophages, and NK cells. With regard to untargeted NPs, the *in vitro* results indicated a relatively low transfection efficiency. It was therefore anticipated that NP pAntiCD20 would exhibit limited efficacy in delivering the antiCD20-coding pDNA to cells. The analysis demonstrated that some antiCD20 production occurred, which would result in the triggering of the classical complement pathway. This is evidenced by the slight levels of C1q and C3-activation fragments, as well as the supposed presence of C5a, which was not directly detected. However, it can be reasonably inferred from the recruitment of PMNs, which were detected, that this complement activation resulted. The restricted transfection rate by NP pAntiCD20 consequently led to a reduction in the number of macrophages and NK cells that were recruited. On the contrary, targeted NPs exhibited a higher *in vitro* transfection efficiency. This enhanced targeting significantly improved the delivery of the antiCD20-coding pDNA to tumor B cells, resulting in possible higher levels of antiCD20 production *in vivo* with consequent binding to its target. The C1q and C3-activation fragments led to suppose the possible activation of the classical complement pathway. This would lead to the recruitment of PMNs to the tumor site through complement-mediated inflammation, as well as macrophages and NK cells. All these cells contribute to the immune response via phagocytosis and ADCC, thereby complementing the effects of PMNs [214] in rendering the TME immunologically active.

The collective results demonstrated the potential of pAntiCD20-loaded PLGA-PVA NPs to induce production of the therapeutic protein in the TME, resulting in slightly noticeable complement system activation and recruitment of inflammatory cells, with a resulting modification of the TME. It is evident that further optimization is necessary, yet this approach has the potential to be a promising treatment for B-cell malignancies and other pathologies. In fact, PLGA-PVA NPs are biodegradable and, therefore safe, and the targeting mechanism ensures the delivery of the payload to the intended site, potentially reducing off-target effects. Moreover, these nanostructures can be conceptualized as a nano-platform on which the individual components, such as the payload or the targeting mechanism, can be substituted in order to achieve disparate objectives.

5. Conclusions

B-cell malignancies constitute a heterogeneous group of clinical conditions, encompassing indolent diseases such as CLL and highly aggressive lymphoproliferative disorders such as BL. Notwithstanding the availability of a range of therapeutic protocols, including dose-intensive chemotherapy and immunotherapy, a considerable proportion of patients experience relapse or are refractory to treatment. Moreover, these treatments often result in inadequate tumor targeting and can cause a multitude of adverse effects, primarily due to a lack of specificity. This in turn requires the use of considerable quantities of drugs in order to achieve the desired therapeutic effect. Given these considerations, our group has recently focused its efforts on developing DNA-loaded targeted NPs as a strategy that integrates targeting systems, gene therapy, and therapeutic antibodies. In this research project, biodegradable polymeric PLGA-PVA NPs were engineered to combine the specificity of the antiCD19 targeting mechanism with a gene therapy approach. Specifically, NPs encapsulate a pDNA encoding an antiCD20 therapeutic antibody, which induces the localized production of the protein within the B-cell TME. This could result in an enhanced concentration at the target site and improved therapeutic outcomes, but primarily in reducing off-target effects in other districts.

Firstly, the antiCD19 targeting mechanism was produced as a recombinant protein and its binding specificity was validated in both CD19$^+$ and CD19$^-$ cell lines.

PLGA-PVA NPs were produced with or without a covalently linked antiCD19 targeting mechanism and subsequently characterized to evaluate their shape (spherical), size (less than 300 nm), and charge (negative). The encapsulation efficiency is approximately 70%, with stability and payload retention (TE buffer, protein, or pDNA) observed for up to one year, regardless of the targeting mechanism presence. The NPs do not cause mechanical disruption of erythrocytes or significant interaction with complement system proteins or coagulation cascade.

In order to test the hypothesis of intravenous administration, an endothelial cells-human whole blood model was established to mimic a blood vessel. The results confirmed no activation of platelets but significant activation of the complement system, endothelial cells, monocytes, and granulocytes. However, no cytokine release by these cell types was observed, which lends support to the marginal activation of the aforementioned cells. This enables us to confirm the biocompatibility of NPs, thereby supporting their use in various applications, such as drug delivery and thrombus prevention, which are documented in published and under-review scientific publications from our laboratory. The targeting mechanism is employed to enhance the preferential activity of these nanosystems. The antiCD19 enables the targeted internalization of NPs in CD19$^+$ cells, both *in vitro* and *in vivo*, as demonstrated in a localized BL tumor-bearing zebrafish model, which represents an optimal model for preliminary studies.

The delivery of the EGFP-coding pDNA enables the demonstration of DNA delivery into cells through the formation of both mRNA and protein in cells. The highest transfection efficiency was observed in CD19$^+$ cells, and comparable outcomes were attained *in vivo* in a zebrafish xenograft lymphoma model.

Biodistribution studies in a BL xenograft mouse model demonstrated that NPs can reach the tumor mass independently of the presence of a targeting mechanism, thereby supporting the hypothesis that NPs reach the site through the EPR effect. It was observed that NPs were present in the lungs, which is likely attributable to the vascular structure of these organs, which facilitates NP deposition, and the liver as an elimination organ, while NPs were not localized in other organs such as the brain, heart, or spleen.

The main aim of the project was to demonstrate that targeted NPs can provide a novel therapeutic avenue through the targeted production of a therapeutic protein within the TME, with the objective of modifying it and rendering it immunologically active. To this end, an antiCD20 antibody, which exhibits characteristics similar to the well-known Rituximab, was selected as a model of therapeutic protein. Its specific binding and killing effect through the CDC mechanism was demonstrated. NPs loaded with a pDNA coding for the aforementioned therapeutic protein were produced and tested in the BL xenograft mouse model. The results demonstrate that the treatment with NPs does not lead to a reduction in tumor growth; however, it results in a slight improvement in survival. In tumor masses, antiCD20 production was detected and related to slight complement system activation and immune system cell recruitment, supporting the effective modification of the TME.

In view of the results obtained, further studies are required, including *in vivo* experiments aimed at enhancing the therapeutic efficacy. One potential avenue for further investigation would be the administration of a higher dose of NPs or variations to the treatment duration. Furthermore, additional strategies should be taken to minimize the accumulation of NPs in other organs, for example, by surface coating to limit possible macrophage interaction. Although the results, they nonetheless lay the foundation for exploiting these NPs as a TME-modifying versatile platform. This approach has the potential to enhance treatment outcomes by making tumors more responsive to standard immunotherapies and other treatments, facilitating the development of more targeted and therapeutically responsive environments. Moreover, these nanoplatform can be modified with different targeting systems or DNA encoding other therapeutic proteins, as well as RNA, representing an actual therapeutic approach, thus enabling potential applications in various pathological conditions.

6. References

1. Siegel, R.L., et al., *Cancer statistics, 2023.* CA Cancer J Clin, 2023. **73**(1): p. 17-48, doi: 10.3322/caac.21763.
2. Dyba, T., et al., *The European cancer burden in 2020: Incidence and mortality estimates for 40 countries and 25 major cancers.* European Journal of Cancer, 2021. **157**: p. 308-347, doi: 10.1016/j.ejca.2021.07.039.
3. Siegel, D.A., et al., *Counts, incidence rates, and trends of pediatric cancer in the United States, 2003-2019.* Journal of the National Cancer Institute, 2023. **115**(11): p. 1337–1354, doi: https://doi.org/10.1093/jnci/djad115.
4. Huang, J., et al., *Global incidence, mortality and temporal trends of cancer in children: A joinpoint regression analysis.* Cancer Medicine, 2022. **12**: p. 1903-1911, doi: 10.1002/cam4.5009.
5. Farrag, A., Ghazaly, M.H., Mohammed, K. et al., *Comparing presentations and outcomes of children with cancer: a study between a lower-middle-income country and a high-income country.* BMC Pediatrics, 2023. **23**, doi: https://doi.org/10.1186/s12887-023-04214-8.
6. Ricci, A.M., et al., *Causes of Childhood Cancer: A Review of the Recent Literature: Part I—Childhood Factors.* Cancers (Basel), 2024. **27**: p. 1297, doi: 10.3390/cancers16071297.
7. Steliarova, E., et al., *International incidence of childhood cancer, 2001-10: a population-based registry study.* Lancet Oncology, 2017. **18**: p. 719-731, doi: 10.1016/S1470-2045(17)30186-9.
8. Lamb, M., et al., *Lymphoid blood cancers, incidence and survival 2005-2023: A report from the UK's Haematological Malignancy Research Network.* Cancer Epidemiology, 2024. **88**, doi: https://doi.org/10.1016/j.canep.2023.102513.
9. Zhang, N., et al., *Global burden of hematologic malignancies and evolution patterns over the past 30 years.* Blood Cancer Journal, 2023. **17**(13): p. 82, doi: 10.1038/s41408-023-00853-3.
10. Olson, O., et al., *Normal Hematopoiesis Is a Balancing Act of Self-Renewal and Regeneration.* Cold Spring Harb Perspect Med., 2020. **10**, doi: 10.1101/cshperspect.a035519.
11. Simón Méndez-Ferrer, e.a., *Bone marrow niches in haematological malignancies.* Nat Rev Cancer., 2020. **5**: p. 285-298, doi: 10.1038/s41568-020-0245-2.
12. Schroeder, H.W., et al., *B-Cell Development and Differentiation.* Clinical Immunology, 2019: p. 107-118, doi: https://doi.org/10.1016/B978-0-7020-6896-6.00007-7.
13. Althwaiqeb, S. and B. Bordoni, *Histology, B Cell Lymphocyte.* 2023, doi: https://www.ncbi.nlm.nih.gov/books/NBK560905/.
14. Tangye, S.G., et al., *Inborn errors of human B cell development, differentiation, and function.* J Exp Med, 2023. **220**(7), doi: 10.1084/jem.20221105.
15. Janeway, C.A.J., Travers, P., Walport, M., et al. , *The structure of a typical antibody molecule.* Immunobiology: The Immune System in Health and Disease. 5th edition, 2001, doi: https://www.ncbi.nlm.nih.gov/books/NBK27144/.
16. Ma, H.a.R.O.K., *The Structure of Natural and Recombinant Antibodies.* Methods Mol Biol, 2015. **1348**: p. 7-11, doi: 10.1007/978-1-4939-2999-3_2.
17. Treanor, B., *B-cell receptor: from resting state to activate.* Immunology, 2012. **136**(1): p. 21-7, doi: 10.1111/j.1365-2567.2012.03564.x.
18. Kuppers, R., et al., *Mechanism of B-cell lymphoma pathogenesis.* Nat Rev Cancer, 2005. **5**(4): p. 251-62, doi: 10.1038/nrc1589.

19. Cooper, M.D., et al., *The evolution of adaptive immune systems.* Cell, 2006. **124**(4): p. 815-22, doi: 10.1016/j.cell.2006.02.001.
20. Pieper, K., et al., *B-cell biology and development.* The Journal of Allergy and Clinical Immunology, 2013. **131**(4): p. 959-971, doi: https://doi.org/10.1016/j.jaci.2013.01.046.
21. Pillai, S., et al., *Birth pangs: the stressful origins of lymphocytes.* The Journal of Clinical Investigation, 2005. **115**(2): p. 224-7, doi: 10.1172/JCI24238.
22. Palm, A.E., et al., *Marginal zone B cells: From housekeeping function to autoimmunity?* Journal of Autoimmunity, 2021. **119**, doi: https://doi.org/10.1016/j.jaut.2021.102627.
23. Klein, U., et al., *Germinal centres: role in B-cell physiology and malignancy.* Nat Rev Immunol, 2008. **8**(1): p. 22-33, doi: 10.1038/nri2217.
24. Le Bien, T., et al., *B lymphocytes: how they develop and function.* Blood, 2008. **112**(5): p. 1570-80, doi: 10.1182/blood-2008-02-078071.
25. Shaffer, A., et al,, *Pathogenesis of Human B Cell Lymphomas.* Annu Rev Immunol, 2012. **30**: p. 565-610, doi: 10.1146/annurev-immunol-020711-075027.
26. Harris, N.L., et al., *The World Health Organization Classification of Hematological Malignancies Report of the Clinical Advisory Committee Meeting, Airlie House, Virginia, November 1997.* Mod Pathol, 2000. **13**(2): p. 193 - 207, doi: https://doi.org/10.1038/modpathol.3880035.
27. Alnughmush, A., et al., *Pediatric-type follicular lymphoma: a short review.* Int J Hematol Oncol, 2022. **11**(4), doi: 10.2217/ijh-2022-0003.
28. De Leval, L., et al., *Lymphoma Classification.* Cancer Journal, 2020. **26**(3): p. 176-185, doi: 10.1097/PPO.0000000000000451.
29. Davies, K., et al., *Pediatric Aggressive Mature B-Cell Lymphomas, Version 2.2020, NCCN Clinical Practice Guidelines in Oncology.* J Natl Compr Canc Netw, 2020. **18**(8): p. 1105-1123, doi: 10.6004/jnccn.2020.0036.
30. McEachron, T.A., Helman, L. J., *Recent advances in pediatric cancer research.* Cancer Res., 2021. **81**(23): p. 5783-5799, doi: 10.1158/0008-5472.CAN-21-1191.
31. Zawitkowska, J., et al., *Diagnosis and therapy pediatric hematological malignancies: recent progress.* Frontiers in Pediatrics, 2023. **11**, doi: https://doi.org/10.3389/fped.2023.1303561.
32. Roschewski, M., *Burkitt's Lymphoma.* The England Journal of Medicine, 2022. **387**(12): p. 1111-1122, doi: 10.1056/NEJMra2025746.
33. Dalla-Favera, R., et al., *Human c-myc onc gene is located on the region of chromosome 8 that is translocated in Burkitt lymphoma cells.* Proc Natl Acad Sci U S A, 1982. **79**(24): p. 7824-7, doi: 10.1073/pnas.79.24.7824.
34. Kalisz, K., et al., *An update on Burkitt lymphoma: a review of pathogenesis and multimodality imaging assessment of disease presentation, treatment response, and recurrence.* Insights into Imaging, 2019. **10**(56), doi: https://doi.org/10.1186/s13244-019-0733-7.
35. Ferry, J.A., *Burkitt's Lymphoma: Clinicopathologic Features and Differential Diagnosis.* The Oncologist, 2006. **11**(4): p. 375-83, doi: 10.1634/theoncologist.11-4-375.
36. Graham, B.S., et al., *Burkitt Lymphoma.* 2023, doi: https://www.ncbi.nlm.nih.gov/books/NBK538148/.
37. Yin, Z., et al., *Advances in chimeric antigen receptor T- cell therapy for B-cell non-Hodgkin lymphoma.* Biomarker Research, 2021. **9**(58), doi: https://doi.org/10.1186/s40364-021-00309-5.

38. Avigdor, A., R. Shouval, and E. Jacoby, *CAR T cells induce a complete response in refractory Burkitt Lymphoma.* Bone Marrow Transplantation, 2018. **53**: p. 1583–1585, doi: https://doi.org/10.1038/s41409-018-0235-0.
39. Vale, A.M., et al., *Clinical consequences of defects in B-cell development.* J Allergy Clin Immunol, 2010. **125**(4): p. 778-87, doi: 10.1016/j.jaci.2010.02.018.
40. Herrera, A.F., et al., *Investigational Antibody-Drug Conjugates for Treatment of B-lineage Malignancies.* Clin Lymphoma Myeloma Leuk, 2018. **18**(7): p. 452-468, doi: 10.1016/j.clml.2018.05.006.
41. Inthagard, J., et al., *Immunotherapy: enhancing the efficacy of this promising therapeutic in multiple cancers.* Clin Sci (Lond), 2019. **133**(2): p. 181-193, doi: 10.1042/CS20181003.
42. Liu, C., et al., *Clinical cancer immunotherapy: Current progress and prospects.* Front. Immunol, 2022. **13**, doi: https://doi.org/10.3389/fimmu.2022.961805.
43. Mitra, A., et al., *From bench to bedside: the history and progress of CAR T cell therapy.* Front. Immunol, 2023. **14**, doi: https://doi.org/10.3389/fimmu.2023.1188049.
44. Shah, A., et al., *Targeting CD22 for the Treatment of B-Cell Malignancies.* Immunotargets Ther., 2021. **10**: p. 225-236, doi: 10.2147/ITT.S288546.
45. Wemlinger, S.M., et al., *Therapeutic tactics for targeting B lymphocytes in autoimmunity and cancer.* European Journal of Immunology, 2023. **54**(1), doi: https://doi.org/10.1002/eji.202249947.
46. Kristóf G. Kovács, e.a., *Revisiting the Coreceptor Function of Complement Receptor Type 2 (CR2, CD21); Coengagement With the B-Cell Receptor Inhibits the Activation, Proliferation, and Antibody Production of Human B Cells.* Front. Immunol., 2021. **12**, doi: https://doi.org/10.3389/fimmu.2021.620427.
47. Levy, S., *Function of the tetraspanin molecule CD81 in B and T cells.* Immunol Res, 2014. **58**: p. 179–185 doi: https://doi.org/10.1007/s12026-014-8490-7.
48. Viardot, A. and E. Sala, *Investigational immunotherapy targeting CD19 for the treatment of acute lymphoblastic leukemia.* Expert Opin Investig Drugs, 2021. **30**(7): p. 773-784, doi: 10.1080/13543784.2021.1928074.
49. Jakobczyk, H., et al., *Promises and limitations of nanoparticles in the era of cell therapy: Example with CD19-targeting chimeric antigen receptor (CAR)-modified T cells.* International Journal of Pharmaceutics, 2017. **53**(2): p. 813-824, doi: 10.1016/j.ijpharm.2017.07.075.
50. Crickx, E., et al., *Anti-CD20–mediated B-cell depletion in autoimmune diseases: successes, failures and future perspectives.* Kidney International, 2020. **97**(5): p. 885 - 893, doi: https://doi.org/10.1016/j.kint.2019.12.025.
51. Lee, A., *Loncastuximab Tesirine: First Approval.* Drugs, 2021. **81**: p. 1229–1233, doi: https://doi.org/10.1007/s40265-021-01550-w.
52. Yan, J., et al., *Targeting antigen to CD19 on B cells efficiently activates T cells.* International Immunology, 2005. **17**(7): p. 869–877, doi: https://doi.org/10.1093/intimm/dxh266.
53. Hong, E.E., et al., *Design of Coltuximab Ravtansine, a CD19-Targeting Antibody−Drug Conjugate (ADC) for the Treatment of B-Cell Malignancies: Structure−Activity Relationships and Preclinical Evaluation.* Molecular Pharmaceutics, 2015. **12**(6): p. 1703-16, doi: 10.1021/acs.molpharmaceut.5b00175.
54. Gerber, H.P., et al., *Potent antitumor activity of the anti-CD19 auristatin antibody drug conjugate hBU12-vcMMAE against rituximab-sensitive and -resistant lymphomas.* Blood, 2009. **113**(18): p. 4352–4361, doi: https://doi.org/10.1182/blood-2008-09-179143.

55. Petrie, R.J., et al., *Colocalization of the B Cell Receptor and CD20 Followed by Activation-Dependent Dissociation in Distinct Lipid Rafts.* Journal of Immunology, 2002. **169**(6): p. 2886–2891, doi: https://doi.org/10.4049/jimmunol.169.6.2886.
56. Pavlasova, G., et al., *The regulation and function of CD20: an "enigma" of B-cell biology and targeted therapy.* Haematologica, 2020. **105**(6): p. 1494–1506, doi: 10.3324/haematol.2019.243543.
57. Taylor, R. and M. Lindorfer, *Analyses of CD20 monoclonal antibody-mediated tumor cell killing mechanisms: rational design of dosing strategies.* Mol Pharmacol, 2014. **86**(5): p. 485-91, doi: 10.1124/mol.114.092684.
58. Dahal, L., et al., *Shaving Is an Epiphenomenon of Type I and II Anti-CD20-Mediated Phagocytosis, whereas Antigenic Modulation Limits Type I Monoclonal Antibody Efficacy.* J Immunol, 2018. **201**(4): p. 1211-1221, doi: 10.4049/jimmunol.1701122.
59. Beum, P., et al., *Loss of CD20 and Bound CD20 Antibody from Opsonized B Cells Occurs More Rapidly Because of Trogocytosis Mediated by Fc Receptor-Expressing Effector Cells Than Direct Internalization by the B Cells.* J Immunol, 2011. **187**(6): p. 3438–3447, doi: https://doi.org/10.4049/jimmunol.1101189.
60. Payandeh, Z., et al., *The applications of anti-CD20 antibodies to treat various B cells disorders.* Biomedicine & Pharmacotherapy, 2019. **109**: p. 2415-2426, doi: https://doi.org/10.1016/j.biopha.2018.11.121.
61. Klein, C., et al., *Epitope interactions of monoclonal antibodies targeting CD20 and their relationship to functional properties.* MAbs, 2013. **5**(1): p. 22-33, doi: 10.4161/mabs.22771.
62. Kumar, A., et al., *Binding mechanisms of therapeutic antibodies to human CD20.* Science, 2020. **369**(6505): p. 793-799, doi: 10.1126/science.abb8008.
63. Lara, S., et al., *Exploring complement-dependent cytotoxicity by rituximab isotypes in 2D and 3D-cultured B-cell lymphoma.* BMC Cancer, 2022. **22**(1): p. 678, doi: 10.1186/s12885-022-09772-1.
64. Pierpont, T.M., et al., *Past, Present, and Future of Rituximab—The World's First Oncology Monoclonal Antibody Therapy.* Front. Oncol., 2018. **8**: p. 163, doi: https://doi.org/10.3389/fonc.2018.00163.
65. Salles, G., et al., *Rituximab in B-Cell Hematologic Malignancies: A Review of 20 Years of Clinical Experience.* Adv Ther, 2017. **34**: p. 2232–2273, doi: https://doi.org/10.1007/s12325-017-0612-x.
66. Danese, M.D., et al., *Estimating the Population Benefits and Costs of Rituximab Therapy in the United States from 1998 to 2013 Using Real-World Data.* Med Care, 2016. **54**(4): p. 343-9, doi: 10.1097/MLR.0000000000000486.
67. Yi, J.H., *Novel combination immunochemotherapy beyond CD20 for B-cell lymphomas.* Blood Res, 2021, doi: 10.5045/br.2021.2020320.
68. Minard-Colin, V., et al., *Rituximab for High-Risk, Mature B-Cell Non-Hodgkin's Lymphoma in Children.* The New England Journal of Medicine, 2020. **382**(23): p. 2207-2219, doi: 10.1056/NEJMoa1915315.
69. Timothy M. Pierpont, e.a., *Past, Present, and Future of Rituximab—The world's First Oncology Monoclonal Antibody Therapy.* Frontiers in Oncology, 2018. **8**(163), doi: 10.3389/fonc.2018.00163.
70. Bergantini, L., d'Alessandro, M., Cameli, P. et al, *Effects of rituximab therapy on B cell differentiation and depletion.* Clin Rheumatol, 2020. **39**: p. 1415–1421, doi: https://doi.org/10.1007/s10067-020-04996-7.
71. Abdelbaky, S., et al., *Cancer immunotherapy from biology to nanomedicine.* J Control Release, 2021. **336**: p. 410-432, doi: 10.1016/j.jconrel.2021.06.025.

72. Gonzalez-Valdivieso, J., et al., *Advanced nanomedicine and cancer: Challenges and opportunities in clinical translation.* Int J Pharm, 2021. **559**: p. 120438, doi: 10.1016/j.ijpharm.2021.120438.
73. Patel, H., et al., *Nanotechnology-based delivery systems to overcome drug resistance in cancer.* Med Rev, 2024. **4**(1): p. 5-30, doi: 10.1515/mr-2023-0058.
74. Yusuf, A., et al., *Nanoparticles as Drug Delivery Systems: A Review of the Implication of Nanoparticles' Physicochemical Properties on Responses in Biological Systems.* Polymers, 2023. **15**(7): p. 1596, doi: https://doi.org/10.3390/polym15071596.
75. Valerian E Kagan, e.a., *Nanomedicine and nanotoxicology: two sides of the same coin.* Nanomedicine, 2005. **1**(4): p. 313-6, doi: 10.1016/j.nano.2005.10.003. PMID: 17292104.
76. Thapa, R.K., Kim, J.O., *Nanomedicine-based commercial formulations: current developments and future prospects.* J. Pharm. Investig., 2023. **53**: p. 19–33, doi: https://doi.org/10.1007/s40005-022-00607-6.
77. Altammar, K., *A review on nanoparticles: characteristics, synthesis, applications, and challenges.* Front. Microbiol, 2023. **14**, doi: https://doi.org/10.3389/fmicb.2023.1155622.
78. Joudeh, N., Linke, D., *Nanoparticle classification, physicochemical properties, characterization, and applications: a comprehensive review for biologists.* J Nanobiotechnol 2022. **20**(262), doi: https://doi.org/10.1186/s12951-022-01477-8.
79. Bozzer, S., et al., *Nanocarriers as a Delivery Platform for Anticancer Treatment: Biological Limits and Perspectives in B-Cell Malignancies.* Pharmaceutics, 2022. **14**(9), doi: 10.3390/pharmaceutics14091965.
80. Hani, U., Gowda, B.H.J., Haider, N., et al., *Nanoparticle-Based Approaches for Treatment of Hematological Malignancies: a Comprehensive Review.* AAPS PharmSciTech, 2023. **24**(233), doi: https://doi.org/10.1208/s12249-023-02670-0.
81. Sijia Yi, e.a., *Dendritic peptide-conjugated polymeric nanovectors for non-toxic delivery of plasmid DNA and enhanced non-viral transfection of immune cells.* iScience, 2022. **25**(7), doi: https://doi.org/10.1016/ j.isci.2022.104555.
82. Colombo, F., et al., *Targeting CD34+ cells of the inflamed synovial endothelium by guided nanoparticles for the treatment of rheumatoid arthritis.* J Autoimmun, 2019. **103**: p. 102288, doi: 10.1016/j.jaut.2019.05.016.
83. Capolla, S., et al., *Targeted chitosan nanobubbles as a strategy to down-regulate microRNA-17 into B-cell lymphoma models.* Front. Immunol, 2023. **21**(376), doi: 10.3389/fimmu.2023.1200310.
84. Khan, I., *Nanoparticles: Properties, applications and toxicities.* Arabian Journal of Chemistry, 2019. **12**(7): p. 908-931, doi: https://doi.org/10.1016/j.arabjc.2017.05.011.
85. Mia, B., et al., *Uptake of Poly-dispersed Carbon Nanotubes Induce Cytotoxic and Cytostatic Effect on Human B Cell Leukemia Cells.* J Clin Toxicol., 2022. **12**(1).
86. Gao, S., et al., *Nanotechnological advances in cancer: therapy a comprehensive review of carbon nanotube applications.* Sec. Nanobiotechnology, 2024. **12**, doi: https://doi.org/10.3389/fbioe.2024.1351787.
87. El-Readi, M.Z., Althubiti, M.A., *Cancer Nanomedicine: A New Era of Successful Targeted Therapy.* Journal of Nanomaterials, 2019, doi: https://doi.org/10.1155/2019/4927312.

88. Chittasupho C, A.S., Sarisuta N., *CXCR4 targeted dendrimer for anti-cancer drug delivery and breast cancer cell migration inhibition.* Eur J Pharm Biopharm, 2017. **119**: p. 310-321, doi: 10.1016/j.ejpb.2017.07.003.
89. Sherje, A.P., Jadhav, M., Dravyakar, B. R., & Kadam, D, *Dendrimers: A versatile nanocarrier for drug delivery and targeting.* International Journal of Pharmaceutics, 2018. **548**(1): p. 707-720, doi: https://doi.org/10.1016/j.ijpharm.2018.07.030.
90. Li, L., et al., *The application advances of dendrimers in biomedical field.* View, 2023, doi: https://doi.org/10.1002/VIW.20230023.
91. Mora-Huertas, C., H. Fessi, and A. Elaissari, *Polymer-based nanocapsules for drug delivery.* Pharmaceutical Nanotechnology, 2010. **385**(1-2): p. 113-142, doi: 10.1016/j.ijpharm.2009.10.018.
92. Xiao, X., et al., *Polymeric nanoparticles—Promising carriers for cancer therapy.* Front. Bioeng. Biotechnol, 2022. **10**, doi: https://doi.org/10.3389/fbioe.2022.1024143.
93. Banik, B., P. Fattahi, and J. Brown, *Polymeric nanoparticles: the future of nanomedicine:.* WIREs Nanomed Nanobiotechnol, 2016. **8**(2): p. 271-299, doi: https://doi.org/10.1002/wnan.1364.
94. Soares, S., Sousa, J., Pais, A., Vitorino, C., *Nanomedicine: Principles, Properties, and Regulatory Issues.* Frontiers in Chemistry, 2018. **6**, doi: https://doi.org/10.3389/fchem.2018.00360.
95. Kamaly, N., *Degradable Controlled-Release Polymers and Polymeric Nanoparticles: Mechanisms of Controlling Drug Release.* Chem Rev, 2016. **116**(4): p. 2602-63, doi: 10.1021/acs.chemrev.5b00346.
96. Mirakabad, F.S.T., et al., *PLGA-based nanoparticles as cancer drug delivery systems.* Asian Pac J Cancer Prev, 2014. **15**(2): p. 517-35, doi: 10.7314/apjcp.2014.15.2.517.
97. M Alvi, A.Y., K Rehman, et al. , *PLGA-based nanoparticles for the treatment of cancer: current strategies and perspectives.* AAPS Open, 2022. **8**(12), doi: https://doi.org/10.1186/s41120-022-00060-7.
98. Bozzer, S., et al., *Zebrafish: A Useful Animal Model for the Characterization of Drug-Loaded Polymeric NPs.* Biomedicines, 2022. **10**(9): p. 2252, doi: 10.3390/biomedicines10092252.
99. Hashem O. Alsaab, e.a., *PLGA-Based Nanomedicine: History of Advancement and Development in Clinical Applications of Multiple Diseases.* Pharmaceutics, 2022. **14**(12), doi: 10.3390/pharmaceutics14122728.
100. Sahoo, S., et al., *Residual polyvinyl alcohol associated with poly (d,l-lactide-co-glycolide) nanoparticles affects their physical properties and cellular uptake.* Journal of Controlled Release, 2002. **82**(1): p. 105-14, doi: 10.1016/s0168-3659(02)00127-x.
101. Salvioni, L., et al., *Thirty Years of Cancer Nanomedicine: Success, Frustration, and Hope.* Cancers, 2019. **11**(12): p. 1855, doi: https://doi.org/10.3390/cancers11121855.
102. Cruz, G.D., et al., *Interaction of Nanoparticles with Blood Components and Associated Pathophysiological Effects.* InTech, 2018, doi: 10.5772/intechopen.69386.
103. Du, B., et al., *Transport and interactions of nanoparticles in the kidneys.* Nat Rev Mater, 2018. **3**: p. 358–374, doi: https://doi.org/10.1038/s41578-018-0038-3.
104. Behzadi, S., et al., *Cellular uptake of nanoparticles: journey inside the cell.* Chem. Soc, 2017. **46**: p. 4218-4244, doi: https://doi.org/10.1039/C6CS00636A.

105. Capolla, S., et al., *Surface antibody changes protein corona both in human and mouse serum but not final opsonization and elimination of targeted polymeric nanoparticles.* Journal of Nanobiotechnology, 2023. **21**(1): p. 376, doi: 10.1186/s12951-023-02134-4.
106. Baboci, L., et al., *The Dual Role of the Liver in Nanomedicine as an Actor in the Elimination of Nanostructures or a Therapeutic Target.* Journal of Oncology, 2020. **24**: p. 4638192, doi: 10.1155/2020/4638192.
107. Fam, S.Y., et al., *Stealth Coating of Nanoparticles in Drug-Delivery Systems.* Nanomaterials, 2020. **10**(4): p. 787, doi: https://doi.org/10.3390/nano10040787.
108. Panico, S., et al., *Biological Features of Nanoparticles: Protein Corona Formation and Interaction with the Immune System.* Pharmaceutics, 2022. **14**(12): p. 2605, doi: 10.3390/pharmaceutics14122605.
109. Zeng, L., et al., *Role of protein corona in the biological effect of nanomaterials: Investigating methods.* TrAC Trends in Analytical Chemistry, 2019. **118**: p. 303-314, doi: https://doi.org/10.1016/j.trac.2019.05.039.
110. Berrecoso, G., Crecente-Campo, J. & Alonso, MJ, *Unveiling the pitfalls of the protein corona of polymeric drug nanocarriers.* Drug Deliv. and Transl., 2020. **10**: p. 730–750 doi: https://doi.org/10.1007/s13346-020-00745-0.
111. Bozzer, S., et al., *Stealth-Engineered Albumin-Coated Nanoparticles for Targeted Therapy: Effective Drug Delivery and Tumor Suppression in Xenograft-Zebrafish Model.* International Journal of Nanomedicine, 2024, doi: 10.2147/IJN.S476241.
112. Katrin Partikel, e.a., *Effect of nanoparticle size and PEGylation on the protein corona of PLGA nanoparticles.* European Journal of Pharmaceutics and Biopharmaceutics, 2019. **141**: p. 70-80, doi: https://doi.org/10.1016/j.ejpb.2019.05.006.
113. Lang Rao, e.a., *Synthetic nanoparticles camouflaged with biomimetic erythrocyte membranes for reduced reticuloendothelial system uptake.* Nanotechnology, 2016. **27**(8): p. 085106, doi: 10.1088/0957-4484/27/8/085106.
114. Qiuyan Guo, e.a., *Cancer cell membrane-coated nanoparticles: a promising anti-tumor bionic platform.* RSC Adv, 2024. **14**: p. 10608-10637, doi: 10.1039/D4RA01026D.
115. Yao, Y., et al, *Nanoparticle-Based Drug Delivery in Cancer Therapy and Its Role in Overcoming Drug Resistance.* Front. Mol. Biosci., 2020. **7**, doi: https://doi.org/10.3389/fmolb.2020.00193.
116. Wicki, A., et al., *Nanomedicine in cancer therapy: challenges, opportunities, and clinical applications.* J Control Release, 2015. **200**: p. 138-57, doi: 10.1016/j.jconrel.2014.12.030.
117. Li, J., et al., *Selective organ targeting nanoparticles: from design to clinical translation.* Nanoscale Horiz, 2023. **8**(9): p. 1155-1173, doi: 10.1039/d3nh00145h.
118. Maeda, H., H. Nakamura, and J. Fang, *The EPR effect for macromolecular drug delivery to solid tumors: Improvement of tumor uptake, lowering of systemic toxicity, and distinct tumor imaging in vivo.* Adv Drug Deliv Rev, 2013. **65**(1): p. 71-9, doi: 10.1016/j.addr.2012.10.002.
119. Gavas, S., et al., *Nanoparticles for Cancer Therapy: Current Progress and Challenges.* Nanoscale Res Lett., 2021. **16**(1): p. 173, doi: 10.1186/s11671-021-03628-6.
120. Elumalai, K., et al., *Review of the efficacy of nanoparticle-based drug delivery systems for cancer treatment.* Biomedical Technology, 2024. **5**: p. 109-122, doi: https://doi.org/10.1016/j.bmt.2023.09.001.

121. Steichen, S.D., et al., *A review of current nanoparticle and targeting moieties for the delivery of cancer therapeutics.* Eur J Pharm Sci, 2013. **48**(3): p. 416-27, doi: 10.1016/j.ejps.2012.12.006.
122. Wilhelm Stefan, e.a., *Analysis of nanoparticle delivery to tumours.* Nature Reviews Materials, 2016. **1**: p. 16014, doi: 10.1038/NATREVMATS.2016.14.
123. Dai, W., et al., *Combination antitumor therapy with targeted dual-nanomedicines.* Adv Drug Deliv Rev, 2017. **336**: p. 410-432, doi: 10.1016/j.addr.2017.03.001.
124. Sanna, V., N. Pala, and M. Sechi, *Targeted therapy using nanotechnology: focus on cancer.* Int J Nanomedicine, 2014. **9**: p. 467-83, doi: 10.2147/IJN.S36654.
125. Bertrand, N., et al., *Cancer nanotechnology: the impact of passive and active targeting in the era of modern cancer biology.* Adv Drug Deliv Rev, 2014. **66**: p. 2-25, doi: 10.1016/j.addr.2013.11.009.
126. Danhier, F., et al., *To exploit the tumor microenvironment: Since the EPR effect fails in the clinic, what is the future of nanomedicine? .* J Control Release, 2016. **244**: p. 108-121, doi: 10.1016/j.jconrel.2016.11.015.
127. Dursun, A., et al., *Enhancement of Paclitaxel Therapeutic Effect by Aptamer Targeted Delivery in PLGA Nanoparticles.* EJMI, 2021. **5**(4): p. 422–426, doi: 10.14744/ejmi.2021.12120.
128. Fleischmann, D., et al., *Steric Shielding of cRGD-Functionalized Nanoparticles from Premature Exposition to Off-Target Endothelial Cells under a Physiological Flow.* ACS Appl. Bio Mater., 2021. **4**(1), doi: 10.1021/acsabm.0c01193.
129. Sosa, Y., et al., *CD19-targeting liposomes containing imatinib efficiently kill Philadelphia chromosome-positive acute lymphoblastic leukemia cells.* Blood, 2004. **104**(5): p. 1442-9, doi: 10.1182/blood-2004-02-0588
130. Mezzaroba N., e.a., *New potential therapeutic approach for the treatment of B-Cell malignancies using chlorambucil/hydroxychloroquine-loaded anti-CD20 nanoparticles.* PLoS One, 2013. **8**(9): p. e74216, doi: 10.1371/journal.pone.0074216.
131. TSOURKAS, A., *Developing Targeted Theranostic Nanoparticles: Challenges and Potential Solutions.* National Academy of Engineering. Frontiers of Engineering: Reports on Leading-Edge Engineering from the 2018 Symposium, 2019, doi: https://www.ncbi.nlm.nih.gov/books/NBK538695/.
132. Cheng Yu, e.a., *Recent Advances in Stimulus-Responsive Nanocarriers for Gene Therapy.* Advanced Science, 2021. **8**(14), doi: https://doi.org/10.1002/advs.202100540.
133. Bulaklak, K. and C. Gersbach, *The once and future gene therapy.* Nat Commun 2020. **11**: p. 5820 doi: https://doi.org/10.1038/s41467-020-19505-2.
134. Krebsbach, E.L.S.a.P.H., *Gene Therapy.* J Dent Res, 2009. **88**(7): p. 585-96, doi: 10.1177/0022034509337480.
135. X.M. Anguela, K.A.H., *Entering the modern era of gene therapy.* Annu. Rev. Med., 2019. **70**: p. 273-288, doi: 10.1146/annurev-med-012017-043332.
136. Levine, B., et al., *Global manufacturing of CAR T cell therapy.* Mol. Ther. Methods Clin, 2017. **4**: p. 92-101, doi: 10.1016/j.omtm.2016.12.006.
137. P. Zarogoulidis, e.a., *Suicide gene therapy for cancer - current strategies.* J. Genet. Syndr. Gene Ther., 2013. **4**, doi: 10.4172/2157-7412.1000139.
138. Nakagami, H., *Development of COVID-19 vaccines utilizing gene therapy technology.* Int. Immunol., 2021. **33**(10): p. 521-527, doi: 10.1093/intimm/dxab013.

139. Fatemeh Arabi, e.a., *Gene therapy clinical trials, where do we go? An overview.* Biomedicine & Pharmacotherapy, 2022. **153**, doi: https://doi.org/10.1016/j.biopha.2022.113324.
140. Lundstrom, K., *Viral Vectors in Gene Therapy: Where Do We Stand in 2023?* Viruses, 2023. **15**(3), doi: 10.3390/v15030698.
141. Murali Ramamoorth, A.N., *Non Viral Vectors in Gene Therapy- An Overview.* J Clin Diagn Res, 2015. **9**(1): p. Ge01-6, doi: 10.7860/JCDR/2015/10443.5394.
142. Colina, A., S., et al., *Current advances in experimental and computational approaches to enhance CAR T cell manufacturing protocols and improve clinical efficacy.* Front. Mol. Med, 2024. **4**, doi: https://doi.org/10.3389/fmmed.2024.1310002.
143. Volodina, O., Smirnikhina, S., *The Future of Gene Therapy: A Review of In Vivo and Ex Vivo Delivery Methods for Genome Editing-Based Therapies.* Mol Biotechnol 2024, doi: https://doi.org/10.1007/s12033-024-01070-4.
144. Lara M. Mollé, e.a., *Nanoparticles for vaccine and gene therapy: Overcoming the barriers to nucleic acid delivery.* ADVANCED REVIEW, 2022. **14**(6), doi: 10.1002/wnan.1809.
145. Peixuan Guo, e.a., *Uniqueness, Advantages, Challenges, Solutions, and Perspectives in Therapeutics Applying RNA Nanotechnology.* Nucleic acid therapeutic, 2012. **22**(4), doi: https://doi.org/10.1089/nat.2012.0350.
146. Rennick, J.J., Johnston, A. P. R., & Parton, R. G., *Key principles and methods for studying the endocytosis of biological and nanopar- ticle therapeutics.* Nature Nanotechnology, 2021. **16**: p. 266–276, doi: https://doi.org/10.1038/s41565-021-00858-8.
147. Kiss, A.L., & Botos, E., *Endocytosis via caveolae: Alternative pathway with distinct cellular compartments to avoid lysosomal degradation?* Journal of Cellular and Molecular Medicine, 2009. **13**(7): p. 1228-1237, doi: https://doi.org/10.1111/j.1582-4934.2009.00754.x.
148. Yuyang Qin, e.a., *Delivery of nucleic acids using nanomaterials.* Mol Biomed, 2023. **4**(1): p. 48, doi: 10.1186/s43556-023-00160-0.
149. Selby, L.I., Cortez-Jugo, C. M., Such, G. K., & Johnston, *Nanoescapology: Progress toward understanding the endosomal escape of polymeric nanoparticles.* Nanomedicine and Nanobiotechnology, 2017. **9**(5): p. e1452, doi: https://doi.org/10.1002/wnan.1452.
150. Dean, D.A., Strong, D. D., & Zimmer, W. E., *Nuclear entry of nonviral vectors.* Gene Therapy, 2005. **12**(881–890), doi: https://doi.org/10.1038/sj.gt.3302534.
151. Knockenhauer, K.E., & Schwartz, T. U., *The nuclear pore complex as a flexible and dynamic gate.* Cell, 2016. **164**(6): p. 1162-1171, doi: https://doi.org/10.1016/j.cell.2016.01.034.
152. Lechardeur, D., et al., *Metabolic instability of plasmid DNA in the cytosol: A potential barrier to gene transfer.* Gene Therapy, 1999. **6**: p. 482–497, doi: https://doi.org/10.1038/sj.gt.3300867.
153. Qin, S., et al., *mRNA-based therapeutics: powerful and versatile tools to combat diseases.* Signal Transduction and Targeted Therapy volume, 2022. **7**(166), doi: https://doi.org/10.1038/s41392-022-01007-w.
154. Kulkarni, J., et al., *The current landscape of nucleic acid therapeutics.* Nature Nanotechnology, 2021. **16**: p. 630–643, doi: https://doi.org/10.1038/s41565-021-00898-0.
155. M. Jafarlou, e.a., *An overview of the history, applications, advantages, disadvantages and prospects of gene therapy.* J. Biol. Regul. Homeost., 2016. **30**(2): p. 315-21.

156. J.T. Bulcha, e.a., *Viral vector platforms within the gene therapy landscape.* Signal Transduct. Target. Ther., 2021. **6**(1): p. 53, doi: 10.1038/s41392-021-00487-6.
157. S. Razi Soofiyani, e.a., *Gene therapy, early promises, subsequent problems, and recent breakthroughs.* Adv. Pharm. Bull., 2013. **3**(2): p. 249-55, doi: 10.5681/apb.2013.041.
158. Chen, J., et al., *Production and clinical development of nanoparticles for gene delivery.* Molecular Therapies Methods & Clinical Development, 2016. **3**, doi: https://doi.org/10.1038/mtm.2016.23.
159. Erin W. Kavanagh, J.J.G., *Toward Gene Transfer Nanoparticles as Therapeutics.* Advanced Healthcare Materials, 2022. **11**(7): p. e2102145, doi: https://doi.org/10.1002/adhm.202102145.
160. Joel G. Rurik, e.a., *CAR T cells produced in vivo to treat cardiac injury.* Science 2022. **375**(6576): p. 91-96, doi: 10.1126/science.abm0594.
161. Labhasetwar, J.K.V.a.V., *Preparation of Biodegradable Nanoparticles and Their Use in Transfection.* Cold Spring Harbor Laboratory Press, 2008, doi: 10.1101/pdb.prot4888.
162. Gerogianni, A., et al., *In vitro evaluation of iron oxide nanoparticle-induced thromboinflammatory response using a combined human whole blood and endothelial cell model.* Front Immunol, 2023. **14**: p. 1101387, doi: 10.3389/fimmu.2023.1101387.
163. Garred, P., et al., *Characterization of a monoclonal antibody MoAb bH6 reacting with a neoepitope of human C3 expressed on C3b, iC3b, and C3c.* Scand J Immunol. , 1988. **27**(3): p. 319-27, doi: 10.1111/j.1365-3083.1988.tb02353.x.
164. T. E. MOLLNES, T.L., S. S. FRØLAND, M. HARBOE, *Quantification of the Terminal Complement Complex in Human Plasma by an Enzyme-Linked Immunosorbent Assay Based on Monoclonal Antibodies against a Neoantigen of the Complex.* Scand J Immunol, 1985, doi: https://doi.org/10.1111/j.1365-3083.1985.tb01871.x.
165. Bergseth, G., et al., *An international serum standard for application in assays to detect human complement activation products.* Mol Immunol, 2013. **56**(3): p. 232-9, doi: 10.1016/j.molimm.2013.05.221.
166. Hoy, S., *Tafasitamab: First Approval.* Drugs, 2020. **80**(16): p. 1731-1737, doi: 10.1007/s40265-020-01405-w.
167. Shao, X., et al., *Independent effect of polymeric nanoparticle zeta potential/surface charge, on their cytotoxicity and affinity to cells.* Cell Prolif, 2015. **48**(4): p. 465-74, doi: 10.1111/cpr.12192.
168. Kurtz-Chalot, A., et al., *Adsorption at cell surface and cellular uptake of silica nanoparticles with different surface chemical functionalizations: impact on cytotoxicity.* J Nanopart Res, 2014. **16**, doi: https://doi.org/10.1007/s11051-014-2738-y.
169. Minh Quan Le, e.a., *Residence time and uptake of porous and cationic maltodextrin-based nanoparticles in the nasal mucosa: Comparison with anionic and cationic nanoparticles.* International Journal of Pharmaceutics, 2018. **1**, doi: https://doi.org/10.1016/j.ijpharm.2018.08.054.
170. Tatiana Petithory, e.a., *Size-Dependent Internalization Efficiency of Macrophages from Adsorbed Nanoparticle-Based Monolayers.* Nanomaterials, 2021. **11**(8): p. 1963, doi: https://doi.org/10.3390/nano11081963.
171. Ma, L., et al., *Quantitative evaluation of cellular internalization of polymeric nanoparticles within laryngeal cancer cells and immune cells for enhanced drug*

delivery. Nanoscale Res Lett., 2021. **16**(40), doi: https://doi.org/10.1186/s11671-021-03498-y.

172. Amin Swed, e.a., *Protein Encapsulation into PLGA Nanoparticles by a Novel Phase Separation Method Using Non-Toxic Solvents.* Journal of Nanomedicine & Nanotechnology, 2014, doi: 10.4172/2157-7439.1000241.
173. Marwah, M., et al., *Novel controlled-release polylactic-co-glycolic acid (PLGA) nanoparticles for sodium thiosulphate, a hydrogen sulphide donor, retains pro-angiogenic potential of hydrogen sulphide.* Journal of Experimental Nanoscience 2022. **17**(1): p. 197–213, doi: https://doi.org/10.1080/17458080.2022.2060963.
174. Johswich, L.S.a.K.O., *Anticoagulants impact on innate immune responses and bacterial survival in whole blood models of Neisseria meningitidis infection.* Sci Rep., 2018. **8**(1): p. 10225, doi: 10.1038/s41598-018-28583-8.
175. P Garred, e.a., *Characterization of a monoclonal antibody MoAb bH6 reacting with a neoepitope of human C3 expressed on C3b, iC3b, and C3c.* Scand J Immunol, 1988, doi: 10.1111/j.1365-3083.1988.tb02353.x.
176. Garred, P., et al., *Quantification in enzyme-linked immunosorbent assay of a C3 neoepitope expressed on activated human complement factor C3.* Scand J Immunol, 1988. **27**(3): p. 329-35, doi: 10.1111/j.1365-3083.1988.tb02354.x.
177. Zhou, H., X. Jiang, and Y. Ventikos, *Role of blood flow in endothelial functionality: a review.* Front Cell Dev Biol, 2023. **11**: p. 1259280, doi: 10.3389/fcell.2023.1259280.
178. Kilgore, K., et al., *Enhancement by the complement membrane attack complex of tumor necrosis factor-alpha-induced endothelial cell expression of E-selectin and ICAM-1.* Journal of Immunology, 1995. **155**(3): p. 1434–1441, doi: https://doi.org/10.4049/jimmunol.155.3.1434.
179. Monsinjon, T., et al., *Regulation by complement C3a and C5a anaphylatoxins of cytokine production in human umbilical vein endothelial cells.* The Faseb Journal, 2003. **17**(9): p. 1003-14, doi: 10.1096/fj.02-0737com.
180. Schraufstatter, I., et al., *Complement c3a and c5a induce different signal transduction cascades in endothelial cells.* Journal of Immunology, 2002. **169**(4): p. 2102-10, doi: 10.4049/jimmunol.169.4.2102.
181. Laudes, I., et al., *Expression and function of C5a receptor in mouse microvascular endothelial cells.* Journal of Immunology, 2002. **169**(10): p. 5962-70, doi: 10.4049/jimmunol.169.10.5962.
182. Yih Yang Chen, e.a., *Flow Rate Affects Nanoparticle Uptake into Endothelial Cells.* Advanced Materials, 2020. **32**(24), doi: https://doi.org/10.1002/adma.201906274.
183. Stig Nymo, e.a., *Human Endothelial Cell Activation by Escherichia coli and Staphylococcus aureus Is Mediated by TNF and IL-1β Secondarily to Activation of C5 and CD14 in Whole Blood.* Journal of Immunology, 2016. **196**(5): p. 2293–2299, doi: https://doi.org/10.4049/jimmunol.1502220.
184. Steven D. Marlin, R.R., *Intercellular Adhesion Molecules: ICAM-1, ICAM-2 And ICAM-3.* Encyclopedia of Immunology, 1998: p. 1409-1412, doi: https://doi.org/10.1006/rwei.1999.0358.
185. Garth L. J. Dixon, e.a., *Endothelial Adhesion Molecule Expression and Its Inhibition by Recombinant Bactericidal/Permeability-Increasing Protein Are Influenced by the Capsulation and Lipooligosaccharide Structure ofNeisseria meningitidis.* Infections and Immunity, 1999. **67**(11), doi: https://doi.org/10.1128/iai.67.11.5626-5633.1999.

186. Liu, J., et al., *The interaction between nanoparticles and immune system: application in the treatment of inflammatory diseases.* J Nanobiotechnol, 2022. **20**(127), doi: https://doi.org/10.1186/s12951-022-01343-7.
187. Michael A Gimbrone Jr, G.G.-C., *Endothelial Cell Dysfunction and the Pathobiology of Atherosclerosis.* Circ Res, 2016. **118**(4): p. 620-36, doi: 10.1161/CIRCRESAHA.115.306301.
188. Cao, Y., *The Toxicity of Nanoparticles to Human Endothelial Cells.* Cellular and Molecular Toxicology of Nanoparticles, 2018: p. 59-69, doi: https://doi.org/10.1007/978-3-319-72041-8_4.
189. Hugh M Davis, e.a., *Human granulocyte CD11b expression as a pharmacodynamic biomarker of inflammation.* Journal of Immunological Methods, 2000. **240**(1-2): p. 125-132, doi: https://doi.org/10.1016/S0022-1759(00)00183-6.
190. Valérie Schaeffer, e.a., *The priming effect of C5a on monocytes is predominantly mediated by the p38 MAPK pathway.* Shock, 2007. **27**(6): p. 623-30, doi: 10.1097/SHK.0b013e31802fa0bd.
191. Katerina Oikonomopoulou, e.a., *Interactions between coagulation and complement--their role in inflammation.* Semin Immunopathol, 2012. **34**(1): p. 151-65, doi: 10.1007/s00281-011-0280-x.
192. Roointan, A., et al., *Poly(lactic-co-glycolic acid): The most ardent and flexible candidate in biomedicine!* International Journal of Polymeric Materials and Polymeric Biomaterials 2017. **67**(17): p. 1028-1049, doi: https://doi.org/10.1080/00914037.2017.1405350.
193. Xu, Z., *Strategy for Cytoplasmic Delivery Using Inorganic Particles.* Pharm Res, 2022. **39**(6): p. 1035–1045, doi: 10.1007/s11095-022-03178-1.
194. Marianna Galliani, e.a., *Nanocarriers for Protein Delivery to the Cytosol: Assessing the Endosomal Escape of Poly(Lactide-co-Glycolide)-Poly(Ethylene Imine) Nanoparticles.* Nanomaterials, 2019. **9**(4): p. 652, doi: https://doi.org/10.3390/nano9040652.
195. Malgorzata S Cartiera, e.a., *The uptake and intracellular fate of PLGA nanoparticles in epithelial cells.* Biomaterials, 2009. **30**(14): p. 2790-8, doi: 10.1016/j.biomaterials.2009.01.057.
196. Ohgaki, R., et al., *Ratiometric fluorescence imaging of cell surface pH by poly(ethylene glycol)-phospholipid conjugated with fluorescein isothiocyanate.* Sci Rep., 2017. **7**(1): p. 17484, doi: 10.1038/s41598-017-17459-y.
197. Harata, M., et al., *CD19-targeting liposomes containing imatinib efficiently kill Philadelphia chromosome-positive acute lymphoblastic leukemia cells.* Blood, 2004. **104**(5): p. 1442-9, doi: 10.1182/blood-2004-02-0588.
198. Lee, L., et al., *The fate of human malignant melanoma cells transplanted into zebrafish embryos: assessment of migration and cell division in the absence of tumor formation.* Dev Dyn, 2005. **233**(4): p. 1560-70, doi: 10.1002/dvdy.20471.
199. Hill, D., et al., *Embryonic zebrafish xenograft assay of human cancer metastasis.* F1000Res, 2018. **7**: p. 1682, doi: 10.12688/f1000research.
200. Bozzer, S., et al., *Nanoparticles-Based Oligonucleotides Delivery in Cancer: Role of Zebrafish as Animal Model.* Pharmaceutics, 2021. **13**(8): p. 1106, doi: 10.3390/pharmaceutics13081106.
201. Karlsson, J., J. von-Hofsten, and P. Olsson, *Generating transparent zebrafish: a refined method to improve detection of gene expression during embryonic development.* Mar Biotechnol (NY), 2001. **3**(6): p. 522-7, doi: 10.1007/s1012601-0053-4.

202. Cabezas-Sáinz, P., et al., *Modeling Cancer Using Zebrafish Xenografts: Drawbacks for Mimicking the Human Microenvironment.* 2020, Cells. **9**: p. 1978, doi: https://doi.org/10.3390/cells9091978.
203. Sofía Mirón-Barroso, e.a., *Nanotechnology-Based Strategies to Overcome Current Barriers in Gene Delivery.* Int. J. Mol. Sci., 2021. **22**(16): p. 8537, doi: https://doi.org/10.3390/ijms22168537.
204. Haiqing Bai, e.a., *Cytoplasmic transport and nuclear import of plasmid DNA.* Biosci Rep, 2017. **37**(6), doi: https://doi.org/10.1042/BSR20160616.
205. Means, N., et al., *Revealing macropinocytosis using nanoparticles.* Mol Aspects Med, 2022. **83**: p. 100993, doi: 10.1016/j.mam.2021.100993.
206. Bosma, M. and A. Carroll, *The SCID mouse mutant: definition, characterization, and potential uses.* Annu Rev Immunol, 1991. **9**: p. 323-50, doi: 10.1146/annurev.iy.09.040191.001543.
207. MS, I., et al., *A Review of Respiratory Anatomical Development, Air Flow Characterization and Particle Deposition.* Int J Environ Res Public Health, 2020. **17**(2), doi: 10.3390/ijerph17020380.
208. Aegerter, H., B.N. Lambrecht, and C.V. Jakubzick, *Biology of lung macrophages in health and disease.* Immunity, 2022. **55**(9): p. 1564-1580, doi: 10.1016/j.immuni.2022.08.010.
209. Mangogna, A., et al., *Is the Complement Protein C1q a Pro- or Anti-tumorigenic Factor? Bioinformatics Analysis Involving Human Carcinomas.* Frontiers in Immunology, 2019. **10**, doi: 10.3389/fimmu.2019.00865.
210. Nesargikar, P., B. Spiller, and R. Chavez, *The complement system: history, pathways, cascade and inhibitors.* Eur J Microbiol Immunol (Bp), 2012. **2**(2): p. 103-11, doi: 10.1556/EuJMI.2.2012.2.2.
211. Macor, P., S. Capolla, and F. Tedesco, *Complement as a biological tool to control tumor growth.* Front Immunol, 2018. **9**: p. 2203, doi: 10.3389/fimmu.2018.02203.
212. Monk, P., et al., *Function, structure and therapeutic potential of complement C5a receptors.* Br J Pharmacol, 2007. **152**(4): p. 429-48, doi: 10.1038/sj.bjp.0707332.
213. SenGupta, S., L. Hein, and C. Parent, *The Recruitment of Neutrophils to the Tumor Microenvironment Is Regulated by Multiple Mediators.* Front Immunol, 2021. **12**: p. 73418, doi: 10.3389/fimmu.2021.734188.
214. Lookeren, C.V., C. Wiesmann, and E. Brown, *Macrophage complement receptors and pathogen clearance.* Cell Microbiol, 2007. **9**: p. 2095–102, doi: https://doi.org/10.1111/j.1462-5822.2007.00981.x.